nature energy

Article

https://doi.org/10.1038/s41560-023-01361-1

Direct in situ measurements of electrical properties of solid–electrolyte interphase on lithium metal anodes

Received: 13 March 2023

Accepted: 22 August 2023

Published online: 28 September 2023

Check for updates

Yaobin Xu[1,9], Hao Jia[2,9], Peiyuan Gao[3], Diego E. Galvez-Aranda[4,5], Saul Perez Beltran[4], Xia Cao[2], Phung M. L. Le[2], Jianfang Liu[6], Mark H. Engelhard[1], Shuang Li[1], Gang Ren[6], Jorge M. Seminario[4,5,7] ✉, Perla B. Balbuena[4,7,8] ✉, Ji-Guang Zhang[2], Wu Xu[2] ✉ & Chongmin Wang[1] ✉

The solid–electrolyte interphase (SEI) critically governs the performance of rechargeable batteries. An ideal SEI is expected to be electrically insulative to prevent persistently parasitic reactions between the electrode and the electrolyte and ionically conductive to facilitate Faradaic reactions of the electrode. However, the true nature of the electrical properties of the SEI remains hitherto unclear due to the lack of a direct characterization method. Here we use in situ bias transmission electron microscopy to directly measure the electrical properties of SEIs formed on copper and lithium substrates. We reveal that SEIs show a voltage-dependent differential conductance. A higher rate of differential conductance induces a thicker SEI with an intricate topographic feature, leading to an inferior Coulombic efficiency and cycling stability in Li||Cu and Li||$LiNi_{0.8}Mn_{0.1}Co_{0.1}O_2$ cells. Our work provides insight into the targeted design of the SEI with desired characteristics towards better battery performance.

Functioning of a rechargeable battery depends on the synergy of three major components in the cell: anode, electrolyte and cathode. The electrolyte, in either solid state or liquid state, is sandwiched between the cathode and the anode to facilitate ion transport[1–3]. The interface between electrolyte and electrode is not atomically sharp; instead, electron transfer across the interface leads to the formation of an interphasial layer, which is termed a solid–electrolyte interphase (SEI) layer[1,4–7]. The characteristics of the SEI layer, including chemical, structural, morphological and mechanical properties[4,8–10], determine a series of key properties of rechargeable batteries, such as active ion inventory, cycle life, rate capability and temperature-dependent performance of a rechargeable battery[2,3,5,11,12]. For better battery performances, the SEI is expected to possess three ideal characteristics: electrically insulative, ionically conductive and constant thickness[5,6]. These three characteristics are interactively correlated. Typically, the SEI thickness is controlled by the electrical properties of the SEI. The thickness of the SEI continuously increases during charge–discharge cycling and shelf storage, indicating that the SEI does not behave as an electrical insulator[1,5,12]. Electronic structure calculations indicate that certain SEI components and their grain boundaries, in contrast with their crystalline counterparts, are prone to electron leakage through the SEI layer[13–18], leading to continued SEI thickening. A thick SEI increases the ion conduction

[1]Environmental Molecular Sciences Laboratory, Pacific Northwest National Laboratory, Richland, WA, USA. [2]Energy and Environment Directorate, Pacific Northwest National Laboratory, Richland, WA, USA. [3]Physical and Computational Sciences Directorate, Pacific Northwest National Laboratory, Richland, WA, USA. [4]Department of Chemical Engineering, Texas A&M University, College Station, TX, USA. [5]Department of Electrical and Computer Engineering, Texas A&M University, College Station, TX, USA. [6]The Molecular Foundry, Lawrence Berkeley National Laboratory, Berkeley, CA, USA. [7]Department of Materials Science and Engineering, Texas A&M University, College Station, TX, USA. [8]Department of Chemistry, Texas A&M University, College Station, TX, USA. [9]These authors contributed equally: Yaobin Xu, Hao Jia. ✉e-mail: seminario@tamu.edu; balbuena@tamu.edu; wu.xu@pnnl.gov; chongmin.wang@pnnl.gov

https://doi.org/10.1038/s41560-023-01361-1

length and consequently the ionic resistance, deteriorating the kinetic properties of batteries[11,12,14]. In addition, the SEI growth also consumes active ions and electrolytes in the batteries, leading to capacity decay, short cycle life and calendar life of the batteries. Although different mechanisms based on mathematical and theoretical models have been proposed to account for the electron leakage behaviour of the SEI and consequently to explain the continuous growth of the SEI[6,14,19–25], such as solvent diffusion[20,21], electron conduction[20,21,23,26], electron tunnelling[27] and Li-interstitial diffusion[22], the transport mechanism behind these phenomena is still under debate and not identified directly by experiment.

Despite the critical importance of the electrical properties of the SEI, quantitative measurement of this parameter remains unsolved due to the lack of a proper and reliable method. The four-point Hebb–Wagner polarization and electrochemical impedance spectroscopy methods for mixed ionic–electronic conductors cannot be readily applied to quantify the electrical conductivity of the SEI[28–30], because the SEI is not only highly air sensitive but also very thin, which is beyond the high spatial resolution of the method. Scanning probe microscopy inside a glovebox or scanning electron microscopy could solve the air-sensitive issue[31,32]. However, the scanning probe method is based on the principle of touching the top surface of the sample, without any information from the top surface to the counter electrode. Adhering to the nature of this limitation, the thickness of the SEI layer at the measuring site cannot be in situ measured. Consequently, it is hard to directly correlate the microstructure and chemical information of the SEI with the measured resistivity. In spite of the lack of concrete experimental evidence, it is widely assumed that an SEI layer behaves as an insulator, as such an assumption helps to interpret, to some degree, the electrochemical performances of rechargeable batteries[4]. In essence, for all types of cell chemistry that are enabled by the SEI, the electrical and ionic properties of the SEI remain the most challenging mystery, leading to a range of behaviours of rechargeable batteries being uninterpreted.

In this Article, we describe an in situ bias transmission electron microscopy (TEM) approach to directly measure the electrical properties of SEI layers grown on copper (Cu) and lithium (Li) substrates, revealing the electrical characteristics of the SEI in terms of current (I)–voltage (V) relationship, differential conductance, critical field strength and bandgap. We unveil that the I–V characteristics of SEIs resemble certain electrical conductance, rather than electrical insulators as assumed in most studies. The SEI with a higher rate differential conductance tends to exhibit a greater thickness and more complex topographic features, consequently leading to an inferior electrochemical performance. The work highlights the governing role of electrical properties of the SEI layer and their tuning towards the enhanced performance of an electrochemical cell.

Electrical properties of SEI layer and battery performance

We integrated in situ TEM with scanning tunnelling microscopy (STM) technique to measure the electrical properties of SEIs on Cu and Li, as illustrated in Fig. 1 and detailed in Supplementary Methods and Supplementary Figs. 1–7. A STM tungsten (W) nanoprobe with atomically clean surface was used as the counter electrode (Supplementary Fig. 3), which was manipulated by the piezo system with three-axis nanometre-scale control. As ion-blocking Cu and W electrodes are used, the measured I–V data directly reflect the electron transport behaviour of the SEI. It should be noted that this measurement with two blocking electrodes does not exactly resemble a real Wagner–Hebb polarization measurement but rather provides an upper limit value of the electrical conductivity[28,33,34]. As the SEI is very sensitive to electron beam[35–38], we performed the I–V measurements at very low magnification of electron dose rate of 1 e^{-} Å^{-2} s^{-1} to avoid electron-beam-induced damage to the SEI and did I–V curve measurement calibration to make sure

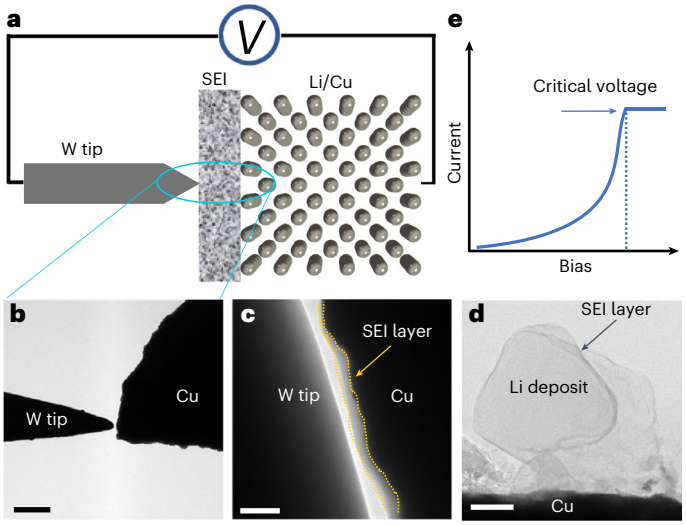

Fig. 1 | In situ bias TEM measurement of electrical properties of the SEI. **a**, Schematic of experiment set-up. **b**. Low-magnification TEM image showing in situ bias set-up of W tip and Cu wire inside TEM. **c**, High-magnification TEM image showing contact between W tip and Cu wire with the SEI on the Cu. **d**, TEM image showing Li deposit with the surface SEI layer using Cu wire as electrode. **e**, Typical I–V curves showing the critical voltage. Scale bars, 50 μm in (**c**) and 100 nm in (**b**,**d**).

the experimental results are repeatable and credible (Supplementary Figs. 8–14 and Supplementary Notes 1–3). Besides, we built Li–electrolyte interface models (Fig. 2a) to investigate the SEI structure using hybrid ab initio molecular dynamics (AIMD) simulation (Fig. 2b) and subsequently calculate the electron transport in the SEI in terms of I–V curve (Fig. 2c). To systematically study different SEIs, Li bis(fluorosulfonyl) imide (LiFSI) and 1,2-dimethoxyethane (DME) were chosen to make four electrolytes with designed microscopic solvation structures[39,40]: (1) a low-concentration electrolyte (LCE) comprised of 1 M LiFSI in DME with a molar ratio of 1:9; (2) a high-concentration electrolyte (HCE) of LiFSI and DME with a molar ratio of 1:1.2; (3) a localized high-concentration electrolyte (LHCE) formed by adding bis(2,2,2-trifluoroethyl) ether (BTFE) diluent into the HCE to yield LiFSI-DME-BTFE = 1:1.2:3 by mole (LHCE-BTFE); and (4) an LHCE with bis(2,2,2-trifluoroethyl) ether carbonate (BTFEC):LiFSI-DME-BTFEC = 1.0:1.2:3.0 by mole (PLHCE, as free DME molecules are not closely coordinated with Li^{+} and making it a pseudo-LHCE[40]) (Supplementary Tables 1 and 2).

The I–V curves of SEIs formed on Cu and Li with the four different electrolytes are shown in Fig. 3. Due to the very thin nature of the SEI (nanoscale), before deciphering the physical meaning of the measured I–V curves of the SEIs, we calibrated the measurement of the I–V curves with known materials at nanoscale as a standard. Therefore, we measured the I–V curves of SiO_2 as a typical insulator and TiO_2 as a semiconductor. As shown in Fig. 3a, even at nanoscale, the I–V curve of SiO_2 shows typical features of an insulator, while that of TiO_2 is a semiconductor. It is rather apparent that the I–V curves of SEIs on both Cu and Li are similar to that of TiO_2 but distinctively different from that of SiO_2, revealing that the electrical properties of SEIs resemble that of a semiconductor. As detailed in Methods and Supplementary Figs. 29–38, based on the results of AIMD simulation of SEI formation and the calculated electronic structure of these four electrolytes, we calculated I–V curve of the SEI on Li metal using the Generalized Electron Nano-Interface Program (GENIP)[13,41]. The calculated I–V curves (Fig. 3d) exhibit similar characteristics and trends to those of experimentally captured ones.

Two characteristic parameters can be extracted from the I–V curves to quantitatively interpret the I–V curves. One is the differential

https://doi.org/10.1038/s41560-023-01361-1

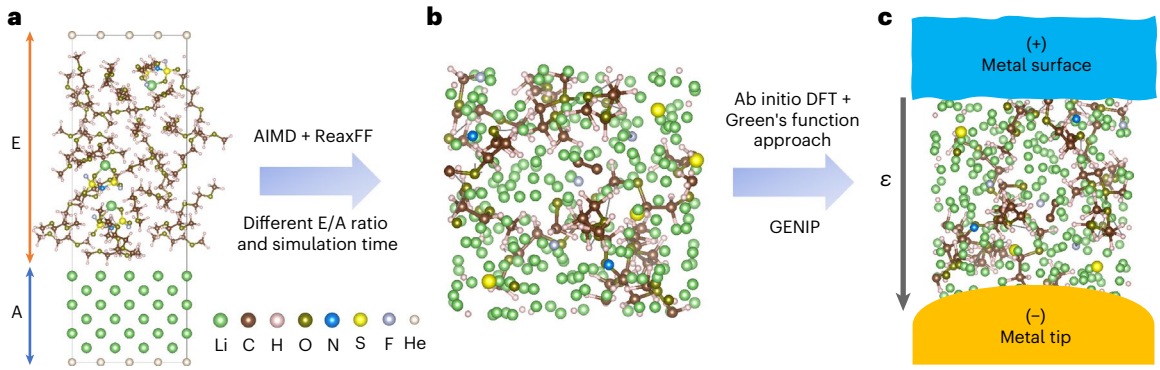

Fig. 2 | Simulation of the SEI structure and subsequent calculation of *I*–*V* curve. a, Simulation cell with different E/A ratio. **b**, Final states of the SEI formed by reaction between electrolyte and Li metal with different E/A ratio and simulation time via AIMD and ReaxFF method. **c**, Schematic of *I*–*V* curve calculation set-up of simulated SEI via ab initio DFT with a Green's function approach. *ε*, voltage.

conductance, d*I*/d*V*, which is plotted as a function of applied voltage, *V* (Fig. 3e–h). Another one is the critical field strength for the breakdown of the SEI. The differential conductance of all samples unanimously shows a linear relationship with the applied voltage. However, the slopes of the linear relationship, which can be termed as the rate of differential conductance, are notably different for different samples. It would be expected that for an insulator, such as SiO_2, the d*I*/d*V* − *V* should have a slope of close to zero, which is consistently supported by what we have measured (SiO_2: 6.06×10^{-27} S V^{-1}). For a semiconductor such as TiO_2, the d*I*/d*V* − *V* plot exhibits a positive slope (2.19×10^{-8} S V^{-1}). The differential conductance (d*I*/d*V*) of all SEIs on both Cu and Li shows linear positive correlations to the applied voltage, while the values of slopes follow a decreasing order from LCE (3.86×10^{-7} S V^{-1} and 2.72×10^{-7} S V^{-1}) to PLHCE (1.22×10^{-7} S V^{-1} and 2.26×10^{-7} S V^{-1}), HCE (8.93×10^{-8} S V^{-1} and 2.53×10^{-8} S V^{-1}) and LHCE (7.67×10^{-8} S V^{-1} and 1.48×10^{-8} S V^{-1}), where the values in the parentheses correspond to the slopes of d*I*/d*V* − *V* on Cu and Li, respectively. Because the differential conductance represents the electron density of state at the local position of the SEI, the positive linear relationship between d*I*/d*V* and voltage indicates that the electrical conductance increases with increasing voltage, implying that the formation of the SEI during battery cycling shows dependence on the voltage difference between the electrode/SEI interface and the SEI/electrolyte interface. The larger the rate of the differential conductance against voltage is, the stronger the SEI responds to the voltage increase. As illustrated in Fig. 3f,g, regardless of the type of substrate (Cu or Li), the SEIs formed by LHCE and HCE electrolytes show a much lower rate of differential conductance than those by PLHCE and LCE electrolytes. The d*I*/d*V* − *V* plot derived from the calculated *I*–*V* curve (Fig. 3h) corroborates our experimental results. It should be noted that to account for the SEI thickness effect, we draw the differential conductance, d*I*/d*V*, as a function of the electrical field strength (voltage divided by the thickness of the SEI) by which the SEI thickness effect is normalized as detailed in the Supplementary Note 4. As shown in Supplementary Fig. 15c, the electrical differential conductance against the electrical field strength shows a similar trend of variation for the case of d*I*/d*V* as a function of *V* (Supplementary Fig. 15b).

With increasing the voltage, the current increases parabolically; and to a critical voltage, the current reaches a critical value that exceeds the maximum value of the instrument (Fig. 3). When applying constant voltage above the critical voltage, the current keeps saturated, indicating the transition from semiconductor to conductor is irreversible (Supplementary Fig. 7). Critical field strength is defined as the critical voltage divided by the sample thickness. The critical field strengths of the SEIs for the four electrolytes are different, which correlate positively with the slopes of the d*I*/d*V* − *V* plots as depicted in Fig. 3f,g. The critical field strength of the SEI formed in LHCE is larger than those of SEIs formed in LCE and PLHCE, indicating the SEI formed in LHCE is much stable against increasing voltage as compared with those formed in other three electrolytes.

To demonstrate the direct correlation between the SEI electrical property and battery performance, the electrochemical performances in terms of Coulombic efficiency (CE) and cycle life of those four electrolytes were evaluated in Li||Cu cells and Li||$LiNi_{0.8}Mn_{0.1}Co_{0.1}O_2$ (NMC811) batteries. As shown in Fig. 3i,j, the first cycle CEs of Li||Cu cells and the stable cycle numbers of Li||NMC811 cells have the following orders: LHCE > HCE > PLHCE > LCE (Supplementary Table 3). Overall, an increased differential conductance of the SEI correlates to a decreased Li CE and battery cycling stability (Fig. 3i,j), indicating the governing role of the SEI electrical property on the battery performance.

Correlation of Li morphology with SEI characteristics

Consistent with the above electrochemical property differences among these four electrolytes is the noticeable difference of morphological features of both the SEI and the deposited Li. The deposited Li in these four electrolytes exhibits crystalline structure and granular morphology (Supplementary Figs. 16 and 17). However, the particle size distributions and topographic features vary obviously. Figure 4a shows the morphologies of the deposited Li particles using high angle annular dark field imaging (HAADF) in scanning transmission electron microscope (STEM) by which the image intensity is proportional to the square of atomic number of the sample. The elemental compositions of the SEI, such as O, C, F, S and N, each have a larger atomic number than Li, leading to a large contrast between the SEI and Li, therefore lending the convenience of delineating the spatial distribution of the SEI. On the basis of the SEI configuration maps (Fig. 4b) derived from the STEM-HAADF images (Fig. 4a), it can be seen that the SEI with a high rate of differential conductance corresponds with a high SEI:Li metal ratio.

Three-dimensional (3D) visualization of Li deposits (Supplementary Video 1) yields details of Li topography. It is evident that for the SEI with a high rate of differential conductance and a low critical field strength, as representatively shown for the case of LCE (Fig. 4c), the deposited Li particles exhibit a wide size distribution, a large fraction of isolated small particles (possible 'dead' Li) and a high topographical tortuosity, leading to the high specific surface area of the SEI. In contrast, for the SEI with a low rate of differential conductance and a high critical field strength, as represented by the case of LHCE (Fig. 4c), the deposited Li particles are large, uniformly distributed and topographically smooth, leading to a low specific surface area of the SEI and less 'dead' Li.

https://doi.org/10.1038/s41560-023-01361-1

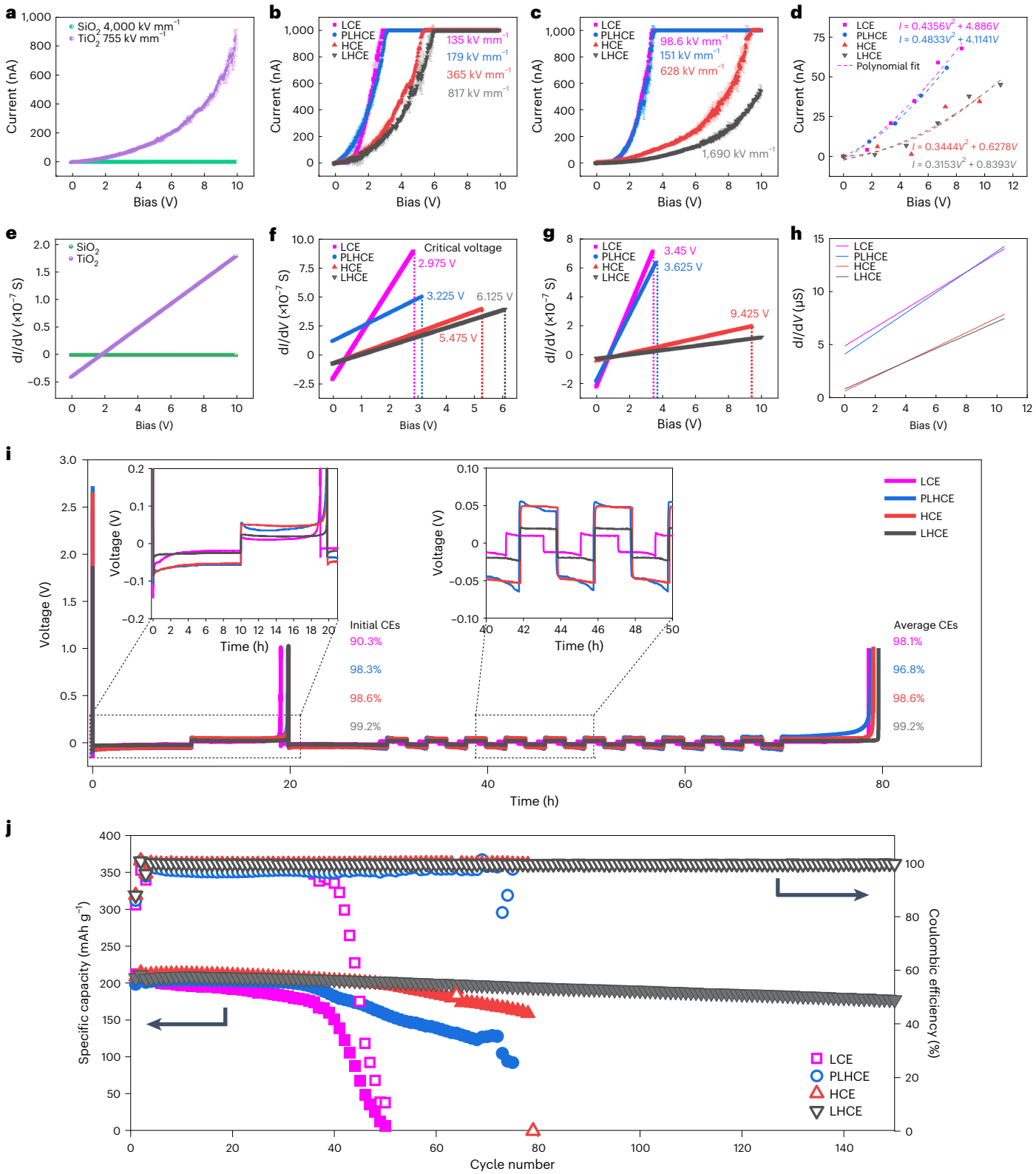

Fig. 3 | Electrical properties of SEI and electrochemical cell performances. **a**, *I*–*V* curves of SiO_2 insulator and TiO_2 semiconductor. Error bars are s.d.; $n = 10$. **b**, *I*–*V* curves of the SEI formed on Cu. **c**, *I*–*V* curves of the SEI formed on Li deposits. Error bars are s.d.; $n = 10$. **d**, Calculated *I*–*V* curve based on sample cell (E/A ratio is 2.79, simulation time is 253 ps). **e**–**h**, Differential conductance, d*I*/d*V* as function of *V*, derived from the *I*–*V* curves, with the critical voltage indicated, for SiO_2 and TiO_2 (**e**), for SEI on Cu (**f**), for SEI on Li (**g**) and for calculated SEI on Li (**h**). The slope of the d*I*/d*V* against *V* in **d**–**f** is termed as rate of differential conductance. **i**, CE of Li||Cu cells. Left inset: CE curve at higher magnification of the initial 20 h. Right inset: CE curve at higher magnification from 40 h to 50 h. Average CEs are from ten cycles. **j**, Long-term cycling stability of Li||NMC811 cells in LCE, PLHCE, HCE and LHCE electrolytes. Error bars in (**a**–**c**) show the reproducibility of measured *I*–*V* curves.

https://doi.org/10.1038/s41560-023-01361-1

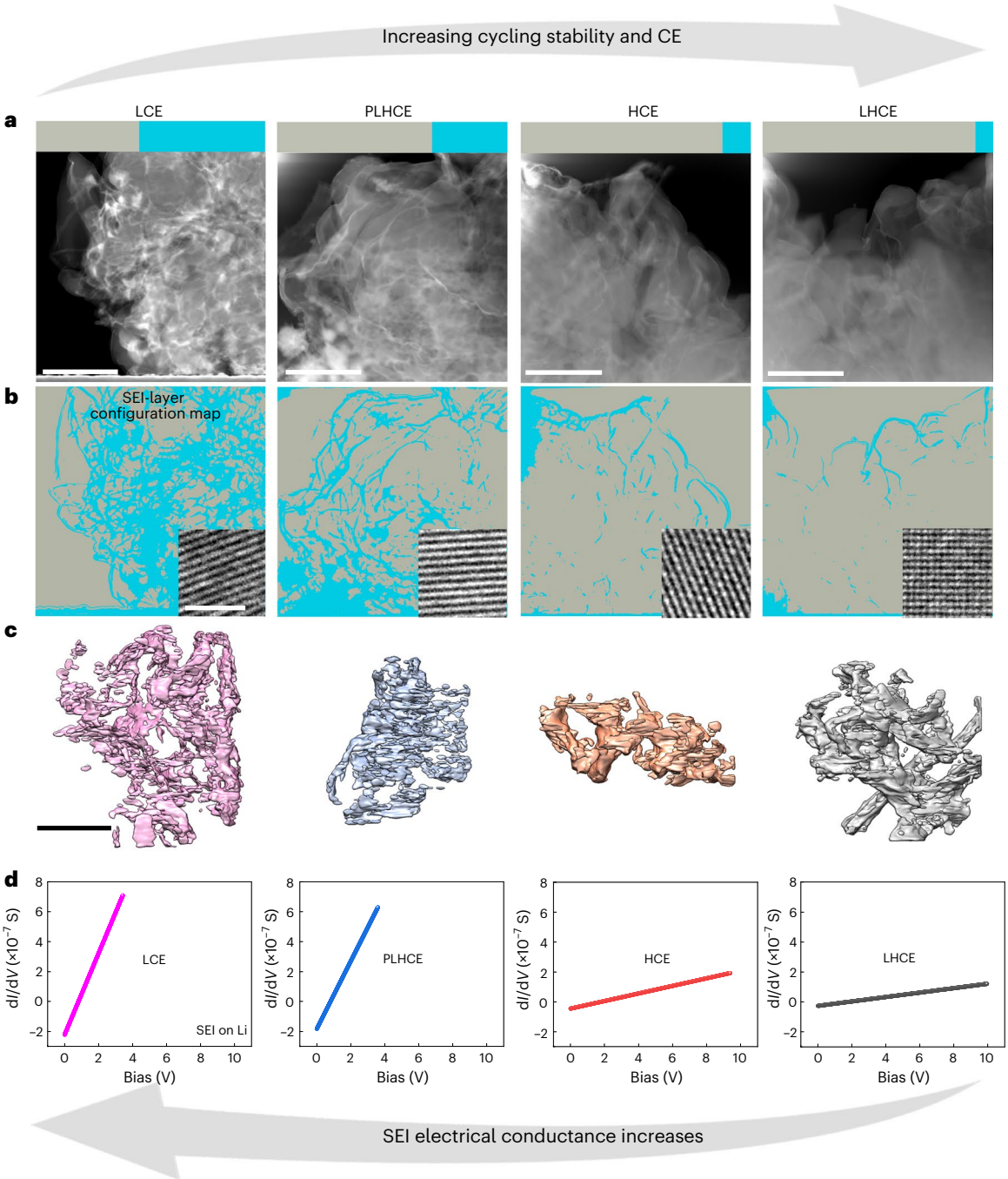

Fig. 4 | Dependence of microstructure of Li deposits on rate of differential conductance. a, Low-magnification cryo-STEM-HAADF images of Li deposits formed in LCE, PLHCE, HCE and LHCE; grey and blue bars indicate the area fraction of Li and SEI, respectively. **b**, SEI-layer configuration maps derived from the STEM-HAADF images. Insets: high-resolution TEM images of Li deposits. **c**, Three-dimensional reconstruction of Li deposits. **d**, d*I*/d*V* – *V* curves of the SEI on Li formed in those four electrolytes, where the slope of d*I*/d*V* as a function of *V* is termed as rate of differential conductance. Scale bars, 5 µm in (**a**,**c**) and 5 nm (inset in **b**).

Thickening of the SEI is a self-limiting process, which is governed by the electron leakage behaviour of the on-growing SEI. Our observations clearly indicate the SEIs formed on Cu (Supplementary Fig. 18) and Li (Fig. 5a) exhibit a similar trend of increasing thickness with a high rate of differential conductance and low critical field strength of the SEI (Fig. 5b). The SEI formed in LCE has the highest rate of differential conductance and the lowest critical field strength, which is corresponded with an SEI thickness of ~35 nm. The SEI formed in LHCE has the lowest rate of differential conductance and the highest critical field strength, corresponding to an SEI thickness of merely 7.5 nm.

Aiming to gain further insight into the origin of different electrical properties of different SEIs, the compositions of SEIs formed on Cu and Li were analysed by cryo-TEM, energy-dispersive X-ray spectroscopy, electron energy-loss spectroscopy (EELS) and X-ray photoelectron spectroscopy (XPS), as shown in Supplementary Figs. 19–28. Chemically, the SEI is composed of Li as the sole cation, which is balanced by the anions comprised of oxygen (O), sulfur (S), carbon (C), fluorine (F) and nitrogen (N). The SEI with a high O:S ratio tends to exhibit a high rate of differential conductance and a low critical field strength, whereas the SEI with a low O:S ratio leads to a low rate of differential

https://doi.org/10.1038/s41560-023-01361-1

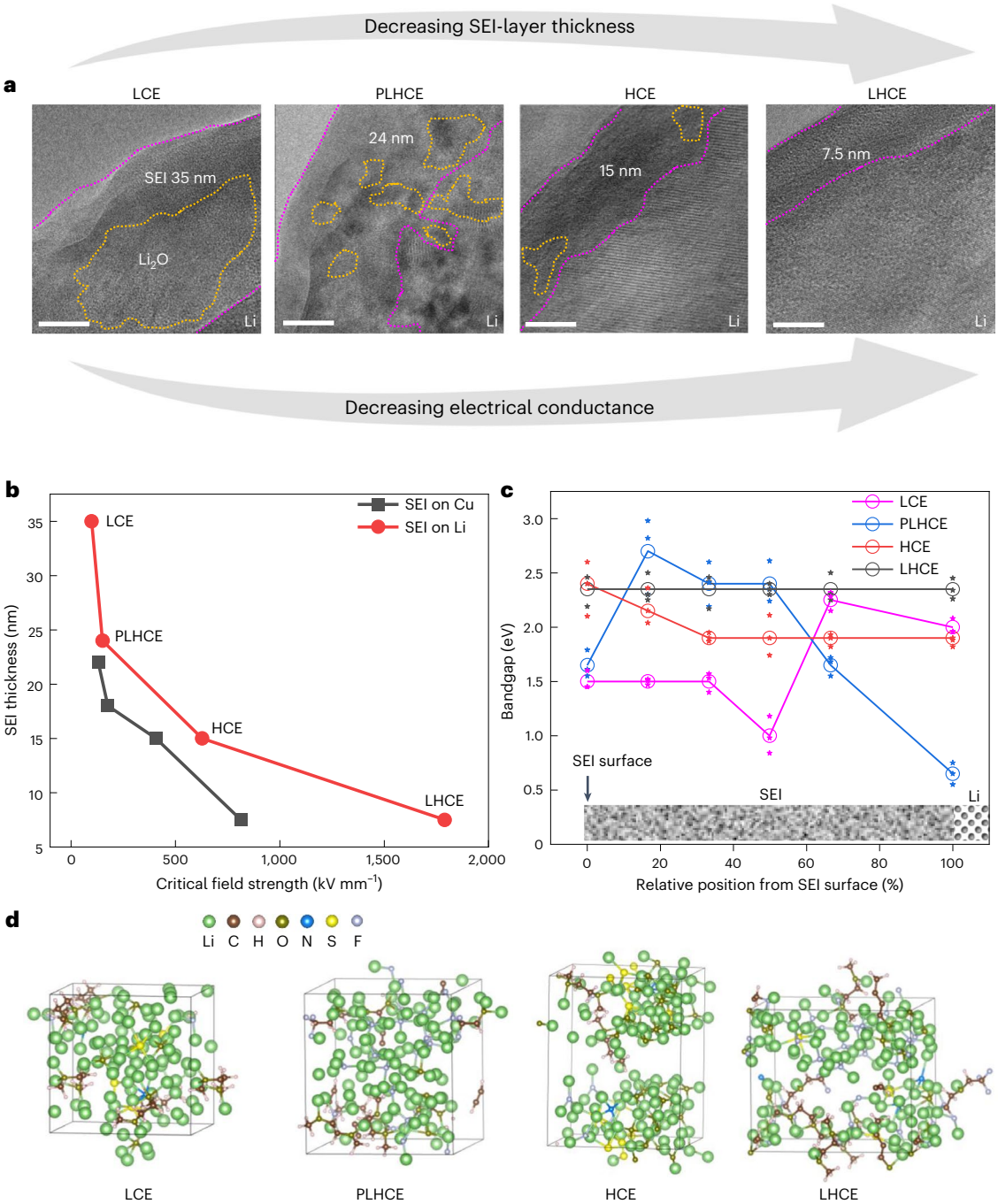

Fig. 5 | Correlation between SEI structure and its electrical property. **a**, Atomic structure of SEI layers on the Li deposits formed in LCE, PLHCE, HCE and LHCE. Scale bars, 5 nm. **b**, SEI thickness as a function of the critical field strength of the SEI on Cu and Li, indicating the SEI layer thickness decreases with increasing critical field strength. **c**, Measured bandgap of the SEI layer on Li for different electrolytes, demonstrating bandgap decrease from the SEI surface towards Li interface. The stars represent individual data points, and the circle signifies the mean. **d**, Snapshots of samples for four electrolytes reacting with Li metal in *I*–*V* curve calculations (E/A ratio is 2.79; simulation time is 253 ps).

conductance and a high critical field strength. The O:S ratios of the SEIs on Cu and Li follow the order from high to low as LCE (4.91 and 19.81) > PLHCE (2.90 and 7.71) > HCE (0.92 and 1.58) > LHCE (0.78 and 0.69), where the values in the parentheses correspond to the O:S ratios of SEIs on Cu and Li, respectively. These values exactly follow the tendencies of gradually decreased rate of differential conductance and increased critical field strength (Supplementary Fig. 23). The variation of O:S ratio represents the relative contribution of the solvent and salt anion derived components of the SEI in these electrolytes as discussed in detail in the Supplementary Note 5. This observation clearly demonstrates that salt derived component in the SEI leads to low electrical conductance, while the SEI component derived from solvent yields high electrical conductance.

Molecular insight into electrical properties of SEI

To delineate the critical factors, in particular molecular-level information that controls the electrical properties of the SEI, we built Li–electrolyte interface models to investigate the SEI structure using hybrid AIMD-based simulation (Supplementary Figs. 29–39, Supplementary Tables 4–8 and Supplementary Notes 6–7) and subsequently calculated

the electron transport in terms of *I*–*V* curve as representatively shown in Fig. 5d for the sampling SEI used for the *I*–*V* curve calculation. The concentrations of the various species in the SEI derived based on hybrid AIMD generally agree with the XPS data (Supplementary Table 9). We found that SEIs formed in LCE and PLHCE, which exhibit high electrical conductance (Fig. 3), show greater proportion of organic to inorganic phase as signified by a higher C content (Supplementary Fig. 39), indicating the dominance of solvent-derived SEI components as what we have experimentally observed. The high proportion of organic components in the SEI will lead to large porosity of the SEI, presence of charged molecular fragments or organic radical species due to incomplete molecular reduction and existence of large amount of dissolved Li ions, which may lead to formation of 'dead' Li as observed experimentally (Fig. 4c). All these collectively contribute to the electron leakage. It should be noticed that the lower concentration of sulfate products in the calculated SEI, as contrasted with that captured from XPS, energy-dispersive X-ray spectroscopy and EELS, is attributed to the fast reaction rate between FSI^- and Li metal and the difference between the electrolyte to anode (E/A) ratio, which may be lower in the simulations than in the experiment[42]. Indeed, we carried out additional simulation with high E/A ratio (Supplementary Figs. 34–36), which demonstrates increased sulfate products, and the calculated *I*–*V* shows similar trend (Supplementary Fig. 37b).

Bandgap is a parameter to reflect electron transition from valance to conduction band, which correlates with the electron tunnelling barrier of the SEI[14,15]. To better understand the electrical properties of the SEI, we measured the bandgaps of the SEI using EELS (Supplementary Fig. 40)[43,44]. The bandgap of the SEI on Li deposit shows two obvious features (Fig. 5c). First, the average bandgap of SEIs follows the increasing order as LCE (1.63 ± 0.12 eV) < PLHCE (1.86 ± 0.13 eV) < HCE (2.03 ± 0.19 eV) < LHCE (2.35 ± 0.14 eV), which corresponds well to the orders of increasing critical field strength and decreasing rate of differential conductance. Second, the bandgaps of SEIs in these four electrolytes show spatial variance from outer to inner SEI with exception of LHCE showing nearly a constant bandgap value across the SEI. It is apparent that the spatial change of bandgap across the SEI thickness direction correlates with the chemical composition variations of the SEI. As shown in Supplementary Fig. 24, the SEI formed in HCE shows a distinctive bilayer structure, where the outer layer has high F intensity, while O distributes near the Li deposit and very few C distributes on the surface of the SEI. The composition difference across the SEI indicates the difference of the electronic environment between the outer layer and the inner layer, hence the difference in the bandgap. The O-rich nature in SEIs consistently accounts for the formation of Li_2O particles in the SEIs in LCE, PLHCE and HCE, while SEIs formed in HCE and LHCE contain S-based components. On the basis of bandgap calculation of SEI components as shown in Supplementary Fig. 41 and previous studies[17,18,45,46], it has been indicated that the electron leakage resistance of amorphous Li_2S (3.07 eV) is higher than that of Li_2O (2.2 eV) (ref. 46). Furthermore, grain boundaries of inorganic compounds have been predicted to enhance electron tunnelling in the SEI[17,18]. It should be noted that the classic model of the SEI is composed of an inner layer of inorganic and an outer layer of organic[5], which, in terms of electrical properties, correspond to a tandem structure. Apparently, it would be expected that the inner layer of inorganic will be the determining layer on the electrical properties. However, given the fact that the inner layer of the SEI is a composite structure with crystalline particles dispersed in the amorphous matrix (including organic and inorganic species) (Fig. 5a and Supplementary Fig. 19), the electron leakage characteristic will be determined by the continuous amorphous matrix, rather than the dispersed crystalline particles.

Discussion

An ideal SEI is highly ionically conductive but electrically insulative. Our direct measurement of the electrical properties of the SEI reveals the electrical behaviours of SEIs formed in four typical electrolytes. Contrary to what has been conventionally assumed, SEIs do not act as perfect electrical insulators. Instead, they show non-negligible electrical conductance, which governs the SEI formation and Li deposition and consequently affects battery performance. A higher electrical conductance of the SEI could facilitate electron transport inside the SEI, especially at the initial stage of SEI formation, leading to the reduction of Li^+ in the SEI and the formation of metallic Li inside the SEI (Supplementary Fig. 42). This reduced Li is isolated by the SEI, leading to the formation of 'dead' Li and moss Li[47,48]. The 'dead' Li and repeated formation of the SEI give rise to low CE, accounting for why Li CE is much lower in LCE and PLHCE (Fig. 3i). The SEI with high electrical conductance and low critical field strength is more susceptible to local electric field variation, such as that induced by protuberances of Cu surface. If the local electric field strength is higher than the critical field strength of the SEI, localized high electrical conduction will lead to localized Li^+ reduction with or on the surface of the SEI and/or localized thickening of the SEI. The electrical behaviours of the SEI, including electrical conductance and critical field strength, account for their surface uniformity and topographical features.

Nucleation and growth of the SEI are mainly based on the electron tunnelling model, consisting of reduction products of electrolytes formed through the reactions between the electrode and the electrolyte[4–6,12,14,49,50]. Associated with the critical thickness for electron tunnelling, the growth of the SEI would be expected to be self-limiting to a thickness of 2–3 nm (refs. 14,45), which is apparently far deviated from experimentally determined values of ranging from 6 nm to 50 nm (refs. 35,36,38,51,52). The mechanism for further growth beyond the critical tunnelling thickness of 2–3 nm remains elusive. Several mechanisms were proposed to account for SEI growth, that is, electron diffusion through point defects such as Li interstitials[22], solvent diffusion[20,21], electron conduction through the SEI[20,21,26] and transition metal-enabled electron transfer[24]. The voltage-dependent electron leakage mechanism has been included in many battery life models and appears to be the only one to explain some experimental observations[6,14,20–22]. The electrical properties of the SEI are determined by the microstructure and chemistry of SEI components formed by the reduction and reaction of electrolyte solvent and Li salt; the SEI with high content of inorganic spices shows good electrical insulation. Tailoring of electrolyte through compositional optimization towards desired properties for different battery systems offers plenty of room for further research, especially those from machine learning approaches, which could be integrated to delineate the critical component and proper electrolyte chemistry to realize ideal SEI properties, that is, high ionic conductivity and electronic insulation, thus solving major challenges of battery research[53].

Conclusions

We developed an in situ bias TEM method to measure the electrical properties of beam-sensitive SEIs formed on the Cu and Li substrates. Our results reveal that the SEI deviates from an insulator, showing voltage-dependent differential conductance. A slight variation in the rate of differential conductance can result in dramatic differences in the SEI thickness and Li morphology and, consequently, the electrochemical performance of the batteries. This work provides a direct method to quantify the electrical properties of the SEI and their effects on the electrochemical performances of rechargeable Li-based batteries. The method established here can be generally used for other types of electrochemical cell as well.

Methods

Fabrication and assembly of coin cells

CR2032 Li||Cu coin cells (MTI) were assembled inside an argon (Ar)-filled glovebox. A Cu wire or Cu TEM half grid placed on a Cu foil current collector was used as the working electrode; a Li metal foil was utilized as both the reference electrode and counter electrode.

A polyethylene separator (Asahi Kasei) was employed to physically separate the working electrode and the reference/counter electrode. Four electrolytes with the same Li salt LiFSI and solvating solvent DME were prepared in the glovebox: LCE of 1 M LiFSI in DME (with a molar ratio of 1:9), HCE of LiFSI-1.2DME (by molar ratio), LHCEs by diluting the HCE with BTFE diluent to form LHCE and BTFEC to form PLHCE with a molar ratio of 1:1.2:3. The physical properties of those solvents and corresponding electrolytes are summarized in Supplementary Tables 1 and 2. SEI formation on Cu electrode was conducted by applying a current density of 0.1 mA cm^{-2} until the cell reached 0 V. Li metal (that is, the SEI on Li) was electrochemically deposited on Cu with a current density of 0.1 mA cm^{-2} for 100 min to reach a fixed Li deposition amount of an areal capacity of 0.167 mAh cm^{-2} as shown in Supplementary Fig. 1 (by using Arbin BT-2000). Therefore, the SEIs we studied are the ones after the first discharge process.

In situ bias TEM measurement of the electrical property of the SEI

In situ measuring the electrical transport properties of the SEI was conducted inside TEM using a nanofactory holder. The TEM holder features a dual-probe design, comprising two distinct components. One probe utilizes a W probe as the electrode, while the other probe consists of a Cu wire coated with the SEI. The Cu wire probe is movable within the TEM column and is driven by a piezo motor with a 1-nm-step size. Inside an Ar-filled glovebox, the Cu wire with SEI/Li particles formed on it was taken out from the coin cell and affixed on the TEM holder. The TEM holder with airtight cover and sealed within the Ar-filled bag was transferred and inserted into the TEM column. This process ensured limited exposure to air, safeguarding the integrity of the samples and maintaining the desired experimental conditions.

Simulations of SEI formation in each electrolyte

Our simulations follow the recently introduced hybrid ab initio and reactive force field (HAIR) method[54]. This approach uses the AIMD and the reactive force field (ReaxFF) method to extend the time simulation window to the order of hundreds of picoseconds[42]; the AIMD method runs for about 0.5 ps each time to provide an accurate description of the localized electrochemical reactions while the ReaxFF runs for 5 ps, allowing access to chemical reactions of greater scope and duration, as well as broader mass transfer processes[42].

The Vienna Ab Initio Simulation Package (VASP, version 5.4.4) is used for the AIMD simulation[55]. The Perdew–Burke–Ernzerhof makes the exchange-correlation energy approximation. The projector augmented wave method addresses electron interactions with a plane-wave basis expansion to 400 eV. The Monkhorst–Pack scheme samples the 1 × 1 × 1 Brillouin zone, and the occupation method is Gaussian smearing (0.05 eV)[42,56]. The electronic self-consistent convergence criterion is 10^{-4} eV, the ensemble of choice is the NVT and the integration of Newton's equations is with the Verlet algorithm. The hydrogen mass is changed to its tritium isotope to enable a time step of 1.2 fs (ref. 57).

The ReaxFF runs with the large-scale atomic/molecular massively parallel simulation software (LAMMPS, version 3Mar20)[42,56]. The ReaxFF parameterization of choice correctly describes the interfacial interactions between the different organic solvents, the FSI^- anions and the Li surface. The time step is 0.25 fs, the NVT ensemble applies and the Nose–Hoover thermostat has a damping parameter of 0.01 fs^{-1}.

We performed simulations with different length and timescale. The first-round simulations complete 46 HAIR cycles for a total of 253 ps with electrolyte to anode (E/A) ratio of 0.75. The second-round simulations complete 46 HAIR cycles but with larger E/A ratio (2.79). All simulation cells were run with about 450 atoms. To confirm our simulation window is long and large enough to allow the system equilibration, we performed additional simulation with 572 atoms, keeping constant the E/A ratio (0.75) and found no notable structural changes (Supplementary Fig. 36e). We also ran another two simulations up to 1 ns (181 HAIR cycles) and found no notable structural changes (Supplementary Fig. 36d,f). The SEI simulation parameters are summarized in Supplementary Table 4. The details of simulation systems are in Supplementary Note 7 (methodology on SEI layer simulation and subsequently *I*–*V* curve calculation).

Current–voltage characteristics of SEI

A fully ab initio DFT with a Green's function approach is used to determine the *I*–*V* characteristics of the SEI produced by the four electrolytes in a Li metal anode. The electronic structure of eight SEIs (two per electrolyte taken from hybrid AIMD runs) was obtained using DFT with the hybrid functional B3PW91[58] encoded in the Gaussian-16 programme[59]. The density and superposition matrices of these calculations were entered into the GENIP[13,41] to obtain the *I*–*V* characteristics of the 11 samples reported in this work.

3D image reconstruction

Serial tilt HAADF/BF-STEM images were acquired from −60° to 60° by every 2° for 3D reconstruction. The tilt series of whole micrographs were initially aligned using the image processing, modelling and display programme[60], and then reconstructed by the individual particle electron tomography (IPET) method[61]. Final 3D maps were reduced missing-wedge artefact by low-tilt tomographic 3D reconstruction method[62]. All IPET 3D reconstructions were Gaussian filtered at the same level and rendered in University of California San Francisco Chimera software[63].

Data availability

All data that support the findings of this study have been included in this article and its Supplementary Information. Source data are provided with this paper.

References

1. Xu, K. Electrolytes and interphases in Li-ion batteries and beyond. *Chem. Rev.* **114**, 11503–11618 (2014).
2. Cheng, X. B., Zhang, R., Zhao, C. Z. & Zhang, Q. Toward safe lithium metal anode in rechargeable batteries: a review. *Chem. Rev.* **117**, 10403–10473 (2017).
3. Lin, D. C., Liu, Y. Y. & Cui, Y. Reviving the lithium metal anode for high-energy batteries. *Nat. Nanotechnol.* **12**, 194–206 (2017).
4. Peled, E. The electrochemical behavior of alkali and alkaline-earth metals in non-aqueous battery systems—the solid–electrolyte-interphase model. *J. Electrochem. Soc.* **126**, 2047–2051 (1979).
5. Peled, E. & Menkin, S. Review—SEI: past, present and future. *J. Electrochem. Soc.* **164**, A1703–A1719 (2017).
6. Wang, A., Kadam, S., Li, H., Shi, S. & Qi, Y. Review on modeling of the anode solid–electrolyte interphase (SEI) for lithium-ion batteries. *npj Comput. Mater.* **4**, 15 (2018).
7. Xu, K. Interfaces and interphases in batteries. *J. Power Sources* **559**, 232652 (2023).
8. Ma, Y. G. et al. Structure and reactivity of alucone-coated films on Si and Li_xSi_y surfaces. *ACS Appl. Mater. Inter.* **7**, 11948–11955 (2015).
9. Wang, L. N. et al. Identifying the components of the solid–electrolyte interphase in Li-ion batteries. *Nat. Chem.* **11**, 789–796 (2019).
10. Shen, X. et al. The failure of solid–electrolyte interphase on Li metal anode: structural uniformity or mechanical strength? *Adv. Energy Mater.* **10**, 1903645 (2020).
11. Winter, M. The solid–electrolyte interphase—the most important and the least understood solid electrolyte in rechargeable Li batteries. *Z. Phys. Chem.* **223**, 1395–1406 (2009).

12. He, X. et al. The passivity of lithium electrodes in liquid electrolytes for secondary batteries. *Nat. Rev. Mater.* **6**, 1036–1052 (2021).
13. Benitez, L. & Seminario, J. M. Electron transport and electrolyte reduction in the solid–electrolyte interphase of rechargeable lithium-ion batteries with silicon anodes. *J. Phys. Chem. C* **120**, 17978–17988 (2016).
14. Lin, Y. X. et al. Connecting the irreversible capacity loss in Li-ion batteries with the electronic insulating properties of solid–electrolyte-interphase (SEI) components. *J. Power Sources* **309**, 221–230 (2016).
15. Liu, Z. et al. Interfacial study on solid–electrolyte interphase at Li metal anode: implication for Li dendrite growth. *J. Electrochem. Soc.* **163**, A592–A598 (2016).
16. Zhang, Q. L. et al. Synergetic effects of inorganic components in solid–electrolyte interphase on high cycle efficiency of lithium-ion batteries. *Nano Lett.* **16**, 2011–2016 (2016).
17. Feng, M., Pan, J. & Qi, Y. Impact of electronic properties of grain boundaries on the solid-electrolyte interphases (SEIs) in Li-ion batteries. *J. Phys. Chem. C* **125**, 15821–15829 (2021).
18. Smeu, M. & Leung, K. Electron leakage through heterogeneous LiF on lithium metal battery anodes. *Phys. Chem. Chem. Phys.* **23**, 3214–3218 (2021).
19. Christensen, J. & Newman, J. A mathematical model for the lithium-ion negative electrode solid–electrolyte interphase. *J. Electrochem. Soc.* **151**, A1977–A1988 (2004).
20. Single, F., Horstmann, B. & Latz, A. Dynamics and morphology of solid-electrolyte interphase (SEI). *Phys. Chem. Chem. Phys.* **18**, 17810–17814 (2016).
21. Single, F., Horstmann, B. & Latz, A. Revealing SEI morphology: in-depth analysis of a modeling approach. *J. Electrochem. Soc.* **164**, E3132–E3145 (2017).
22. Single, F., Latz, A. & Horstmann, B. Identifying the mechanism of continued growth of the solid–electrolyte interphase. *ChemSusChem* **11**, 1950–1955 (2018).
23. Kobbing, L., Latz, A. & Horstmann, B. Growth of the solid–electrolyte interphase: electron diffusion versus solvent diffusion. *J. Power Sources* **561**, 232651 (2023).
24. Harris, O. C., Lin, Y. X., Qi, Y., Leung, K. & Tang, M. H. How transition metals enable electron transfer through the SEI: part I. Experiments and Butler–Volmer modeling. *J. Electrochem. Soc.* **167**, 013502 (2019).
25. Ploehn, H. J., Ramadass, P. & White, R. E. Solvent diffusion model for aging of lithium-ion battery cells. *J. Electrochem. Soc.* **151**, A456–A462 (2004).
26. Attia, P. M., Das, S., Harris, S. J., Bazant, M. Z. & Chueh, W. C. Electrochemical kinetics of SEI growth on carbon black: part I. Experiments. *J. Electrochem. Soc.* **166**, E97–E106 (2019).
27. Tang, M., Lu, S. D. & Newman, J. Experimental and theoretical investigation of solid–electrolyte-interphase formation mechanisms on glassy carbon. *J. Electrochem. Soc.* **159**, A1775–A1785 (2012).
28. Riess, I. Four point Hebb–Wagner polarization method for determining the electronic conductivity in mixed ionic–electronic conductors. *Solid State Ionics* **51**, 219–229 (1992).
29. Liu, Y. et al. Impacts of the properties of anode solid–electrolyte interface on the storage life of Li-ion batteries. *J. Phys. Chem. C* **122**, 9411–9416 (2018).
30. Lorger, S., Usiskin, R. & Maier, J. Transport and charge carrier chemistry in lithium oxide. *J. Electrochem. Soc.* **166**, A2215–A2220 (2019).
31. Stetson, C. et al. Three-dimensional electronic resistivity mapping of solid–electrolyte interphase on Si anode materials. *Nano Energy* **55**, 477–485 (2019).
32. Santos, C. S., Botz, A., Bandarenka, A. S., Ventosa, E. & Schuhmann, W. Correlative electrochemical microscopy for the elucidation of the local ionic and electronic properties of the solid–electrolyte interphase in Li-ion batteries. *Angew. Chem. Int. Ed.* **61**, e202202744 (2022).
33. Su, Y. et al. LiPON thin films with high nitrogen content for application in lithium batteries and electrochromic devices prepared by RF magnetron sputtering. *Solid State Ion.* **282**, 63–69 (2015).
34. Han, F. et al. High electronic conductivity as the origin of lithium dendrite formation within solid electrolytes. *Nat. Energy* **4**, 187–196 (2019).
35. Li, Y. Z. et al. Atomic structure of sensitive battery materials and interfaces revealed by cryo-electron microscopy. *Science* **358**, 506–510 (2017).
36. Wang, X. F. et al. New insights on the structure of electrochemically deposited lithium metal and its solid–electrolyte interphases via cryogenic TEM. *Nano Lett.* **17**, 7606–7612 (2017).
37. Zachman, M. J., Tu, Z., Choudhury, S., Archer, L. A. & Kourkoutis, L. F. Cryo-STEM mapping of solid–liquid interfaces and dendrites in lithium metal batteries. *Nature* **560**, 345–349 (2018).
38. Xu, Y. et al. Atomic to nanoscale origin of vinylene carbonate enhanced cycling stability of lithium metal anode revealed by cryo-transmission electron microscopy. *Nano Lett.* **20**, 418–425 (2020).
39. Ren, X. et al. Role of inner solvation sheath within salt–solvent complexes in tailoring electrode/electrolyte interphases for lithium metal batteries. *Proc. Natl Acad. Sci. USA* **117**, 28603–28613 (2020).
40. Cao, X. et al. Effects of fluorinated solvents on electrolyte solvation structures and electrode/electrolyte interphases for lithium metal batteries. *Proc. Natl Acad. Sci. USA* **118**, e2020357118 (2021).
41. Derosa, P. A. & Seminario, J. M. Electron transport through single molecules: scattering treatment using density functional and green function theories. *J. Phys. Chem. B* **105**, 471–481 (2001).
42. Beltran, S. P. & Balbuena, P. B. SEI formation mechanisms and Li^+ dissolution in lithium metal anodes: impact of the electrolyte composition and the electrolyte-to-anode ratio. *J. Power Sources* **551**, 232203 (2022).
43. Rafferty, B. & Brown, L. M. Direct and indirect transitions in the region of the bandgap using electron-energy-loss spectroscopy. *Phys. Rev. B* **58**, 10326–10337 (1998).
44. Liu, X. et al. Local electronic structure variation resulting in Li 'filament' formation within solid electrolytes. *Nat. Mater.* **20**, 1485–1490 (2021).
45. Li, Y. S. & Qi, Y. Transferable self-consistent charge density functional tight-binding parameters for Li-metal and Li-ions in inorganic compounds and organic solvents. *J. Phys. Chem. C* **122**, 10755–10764 (2018).
46. Xu, J. G. et al. Mechanical and electronic stabilization of solid–electrolyte interphase with sulfite additive for lithium metal batteries. *J. Electrochem. Soc.* **166**, A3201–A3206 (2019).
47. Lu, D. P. et al. Failure mechanism for fast-charged lithium metal batteries with liquid electrolytes. *Adv. Energy Mater.* **5**, 1400993 (2015).
48. Fang, C. et al. Quantifying inactive lithium in lithium metal batteries. *Nature* **572**, 511–515 (2019).
49. Peled, E., Golodnitsky, D. & Ardel, G. Advanced model for solid–electrolyte-interphase electrodes in liquid and polymer electrolytes. *J. Electrochem. Soc.* **144**, L208–L210 (1997).
50. Aurbach, D. et al. New insights into the interactions between electrode materials and electrolyte solutions for advanced non-aqueous batteries. *J. Power Sources* **81**, 95–111 (1999).

51. Zhang, Z. et al. Capturing the swelling of solid-electrolyte interphase in lithium metal batteries. *Science* **375**, 66–70 (2022).
52. Yu, Z. et al. Molecular design for electrolyte solvents enabling energy-dense and long-cycling lithium metal batteries. *Nat. Energy* **5**, 526–533 (2020).
53. Li, J. et al. Dynamics of particle network in composite battery cathodes. *Science* **376**, 517–521 (2022).
54. Liu, Y. et al. The DFT-ReaxFF hybrid reactive dynamics method with application to the reductive decomposition reaction of the TFSI and DOL electrolyte at a lithium metal anode surface. *J. Phys. Chem. Lett.* **12**, 1300–1306 (2021).
55. Kresse, G. & Hafner, J. Ab initio molecular dynamics for liquid metals. *Phys. Rev. B* **47**, 558–561 (1993).
56. Plimpton, S. Fast parallel algorithms for short-range molecular dynamics. *J. Comput. Phys.* **117**, 1–19 (1995).
57. Kamphaus, E. P. & Balbuena, P. B. First-principles investigation of lithium polysulfide structure and behavior in solution. *J. Phys. Chem. C* **121**, 21105–21117 (2017).
58. Perdew, J. P. & Wang, Y. Accurate and simple analytic representation of the electron-gas correlation energy. *Phys. Rev. B* **45**, 13244–13249 (1992).
59. Frisch, M. J. et al. Gaussian 16 Rev. C.01 (Gaussian, 2016).
60. Kremer, J. R., Mastronarde, D. N. & McIntosh, J. R. Computer visualization of three-dimensional image data using IMOD. *J. Struct. Biol.* **116**, 71–76 (1996).
61. Zhang, L. & Ren, G. IPET and FETR: experimental approach for studying molecular structure dynamics by cryo-electron tomography of a single-molecule structure. *PLoS ONE* **7**, e30249 (2012).
62. Zhai, X. B. et al. LoTToR: an algorithm for missing-wedge correction of the low-tilt tomographic 3D reconstruction of a single-molecule structure. *Sci. Rep.* **10**, 10489 (2020).
63. Pettersen, E. F. et al. UCSF chimera—a visualization system for exploratory research and analysis. *J. Comput. Chem.* **25**, 1605–1612 (2004).

Acknowledgements

We thank Y. Wu at Pacific Northwest National Laboratory (PNNL) for providing the TiO_2 sample and C. Yan at University of Chicago for helpful discussions about electrical measurement. This work was supported by the Energy Efficiency and Renewable Energy, Office of Vehicle Technologies of the US Department of Energy (DOE) under the Advanced Battery Materials Research (BMR) Program and the US–Germany Cooperation on Energy Storage under Contract DE-LC-000L072 (C.W. and W.X.). P.B.B. and J.M.S. acknowledge the US–Germany Cooperation on Energy Storage under Contract DE-AC02-05CH11357 and the Assistant Secretary for Energy Efficiency and Renewable Energy, Office of Vehicle Technologies of the US DOE through the BMR Program (Battery500 Consortium phase 2) under DOE contract DE-AC05-76RL01830 from PNNL. Computational resources from the Texas A&M University High Performance Research Computing are gratefully acknowledged. The characterization work was conducted in the William R. Wiley Environmental Molecular Sciences Laboratory, a national scientific user facility sponsored by DOE's Office of Biological and Environmental Research and located at PNNL. PNNL is operated by Battelle for the US DOE under contract DE-AC05-76RL01830. The work at the molecular foundry, Lawrence Berkeley National Laboratory was supported by the Office of Science, Office of Basic Energy Sciences of the US DOE under contract DE-AC02-05CH11231. G.R. and J.L. acknowledge US National Institutes of Health grants R01HL115153, R01GM104427, R01MH077303 and R01DK042667.

Author contributions

C.W. and Y.X. conceived the project and designed the experiments with suggestions from W.X. and H.J. Y.X. collected and analysed experimental data for in situ TEM and cryo-TEM studies and drafted the paper under the direction of C.W. and W.X. H.J. performed the electrochemical measurements. P.G. performed the AIMD calculation of bulk electrolytes. D.E.G.-A. and J.M.S. performed the SEI composition analyses, the molecular orbital electronic structure calculations and the current–voltage characteristics of the SEI samples. S.P.B. and P.B.B. performed hybrid AIMD combined with reactive force field simulations. J.L. and G.R. carried out three-dimensional reconstruction. X.C. conducted battery cycling tests. P.M.L.L. and J.-G.Z. helped with interpretation of the electrochemical data. M.H.E. collected XPS data. S.L. prepared the W STM tip. Y.X., H.J., W.X. and C.W. co-wrote the original paper. All authors discussed the results and edited the paper.

Competing interests

The authors declare no competing interests.

Additional information

Supplementary information The online version contains supplementary material available at https://doi.org/10.1038/s41560-023-01361-1.

Correspondence and requests for materials should be addressed to Jorge M. Seminario, Perla B. Balbuena, Wu Xu or Chongmin Wang.

Peer review information *Nature Energy* thanks the anonymous reviewers for their contribution to the peer review of this work.

nature energy

Article

https://doi.org/10.1038/s41560-023-01361-1

Direct in situ measurements of electrical properties of solid–electrolyte interphase on lithium metal anodes

In the format provided by the authors and unedited

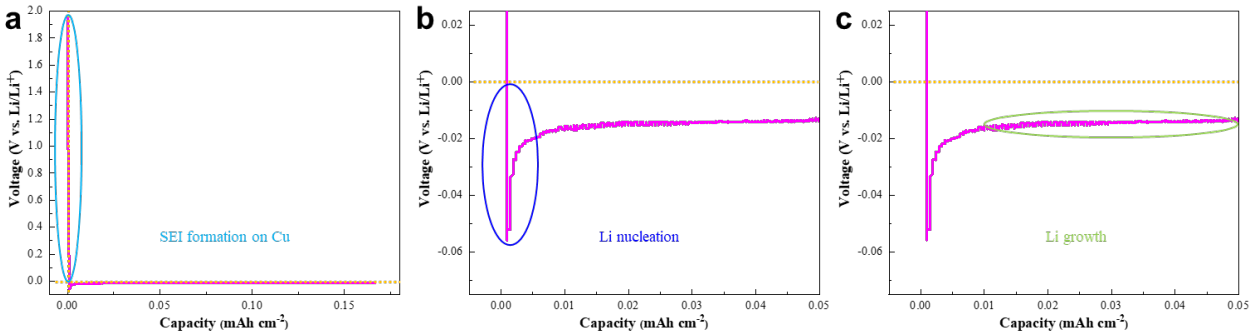

Supplementary Fig. 1 | Deposition curve of coin cell with Cu wire. a, Experimental voltage profiles of Li deposition on Cu foil with Cu wire in LCE for a total capacity of 0.167 mA h cm^{-2}. The light blue ellipse indicates voltage above 0 V, which is related SEI formation on Cu. **b**, Amplified region of voltage below 0 V. A clear overpotential was observed, as highlighted by the dark blue ellipse which corresponding Li nucleation. **c**, The green ellipse indicates Li growth region.

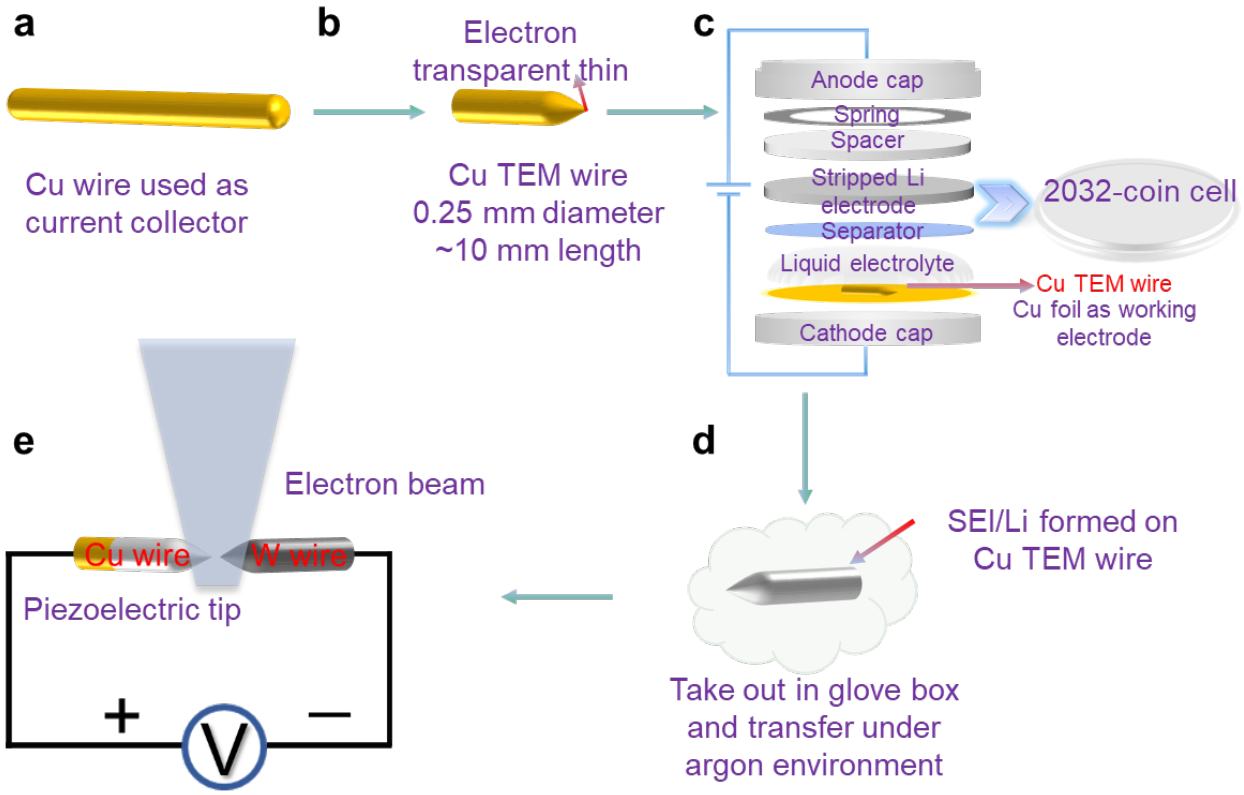

Supplementary Fig. 2 | Schematic of preserving and electrical measurement of SEI formed on Cu current collector by in situ TEM. a, Cu wire as current collector. **b**, Cu TEM wire with electron transparent thin area prepared from Cu wire. **cb** Assembling Cu TEM wire into a coin cell. **d**, Disassembling of coin cell in glove box. **e**, The Cu TEM wire with SEI/Li deposition is loaded on in situ bias TEM holder in glove box and is subsequently transferred to TEM in Ar environment.

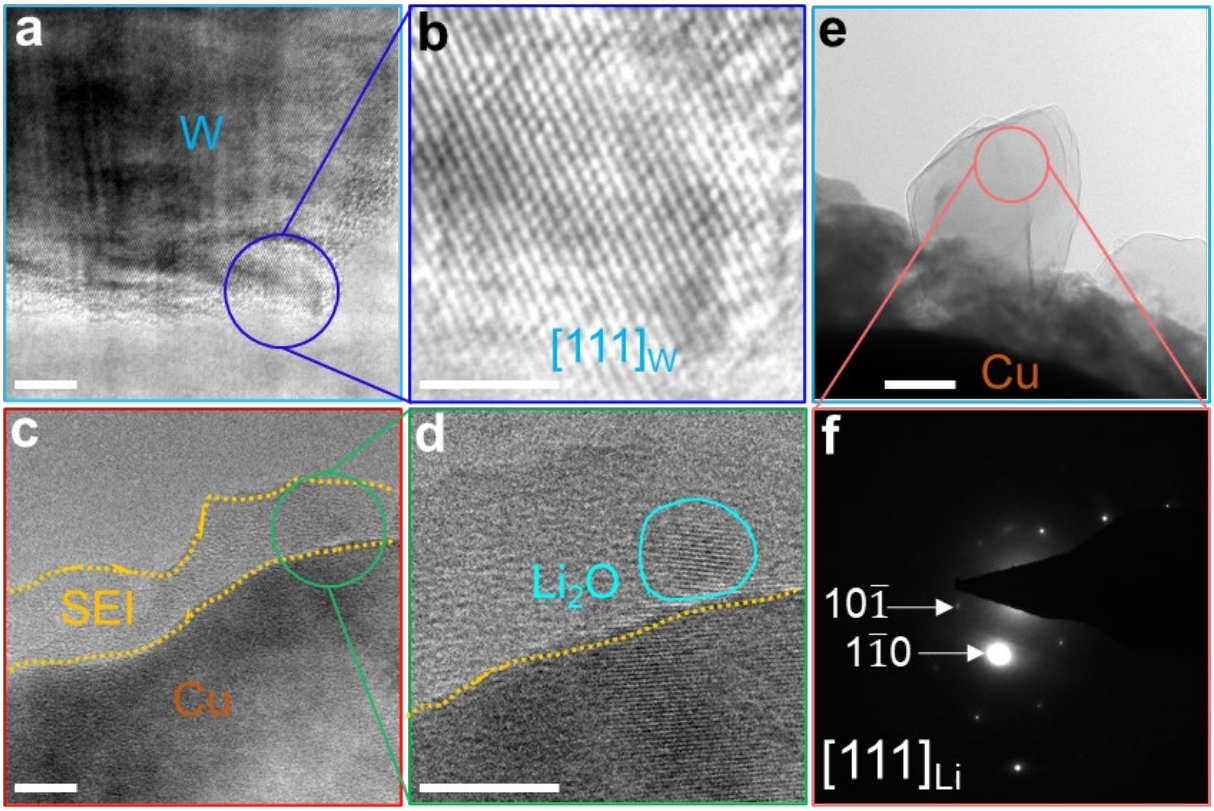

Supplementary Fig. 3 | Structures of the Cu and W tip. a-b, TEM images showing W wire with clean surface. **c-d**, TEM images showing Cu TEM wire with SEI formed on the surface. **e-f**, TEM image showing Li deposit formed on the Cu TEM wire and corresponding SAED patter. Scale bars, 5 nm in **a** and **c**, 2 nm in **b** and **d**, and 200 nm in **e**.

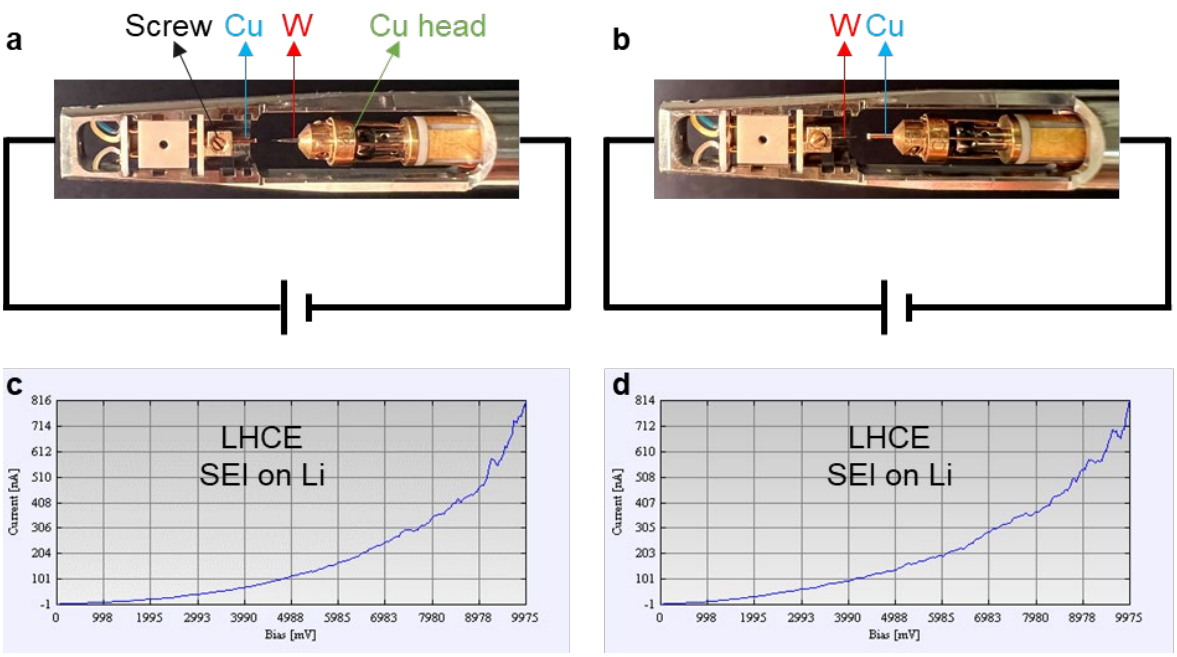

Supplementary Fig. 4 | Experimental setup for in situ I-V curve measurement. a, Initial setup with Cu as negative electrode and W as positive electrode. **b**, Final setup with Cu as positive electrode and W as negative electrode. **c**, I-V curve measured based on initial setup. **d**, I-V curve measured based on final setup.

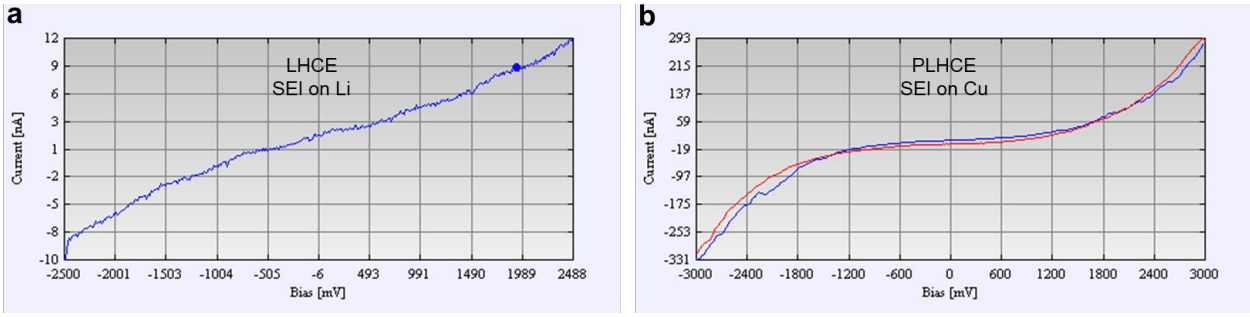

Supplementary Fig. 5 | The reversibility of I-V curve upon forward and reverse biasing. **a**, I-V curve of SEI on Li formed in LHCE (the electrolyte with BTFE diluent). **b**, I-V curve of SEI on Cu formed in PLHCE (the electrolyte with BTFEC diluent) with 2 cycles.

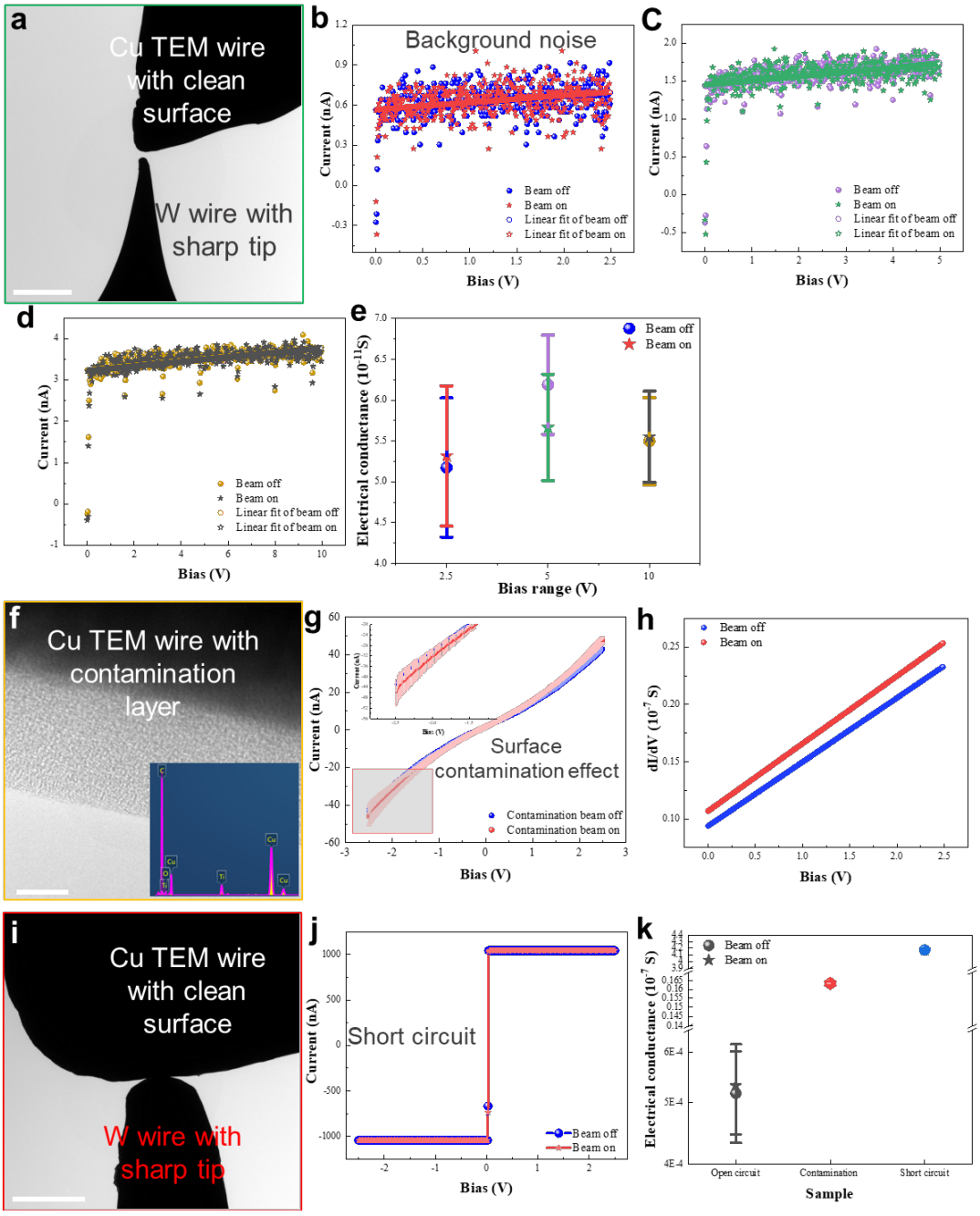

Supplementary Fig. 6 | The feasibility study of in situ probing electrical response measurements in the TEM. a-e, Detection of background noise when W wire does not contact with Cu wire. Error bars, s.d. n=10. **f-h**, Short circuit phenomenon happens when W wire directly contacts with Cu wire without SEI formed on its surface. Error bars, s.d. n=10. Error bars in g show the reproducibility of measured I-V curves. **i-j**, Surface contamination effect revealed when the Cu wire was prepared in the air with contamination layer on the surface. **k**, Summary of electrical conductance measurement in those three sample configurations. Error bars, s.d. n=10. Scale bars, 100 μm in **a**, 10 nm in **f**, and 10 μm in **i**.

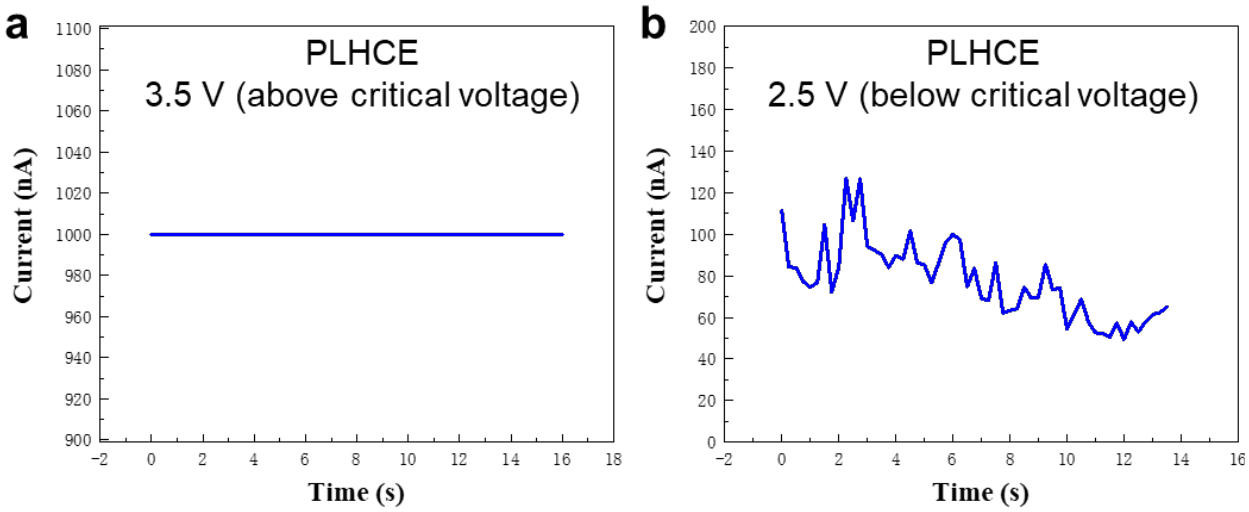

Supplementary Fig. 7 | Electrical transport measurements of SEI formed on the Cu in PLHCE. **a**, I-V curve of the SEI formed on Cu with constant voltage above critical voltage. **b**, I-V curve of the SEI formed on Cu with constant voltage below critical voltage.

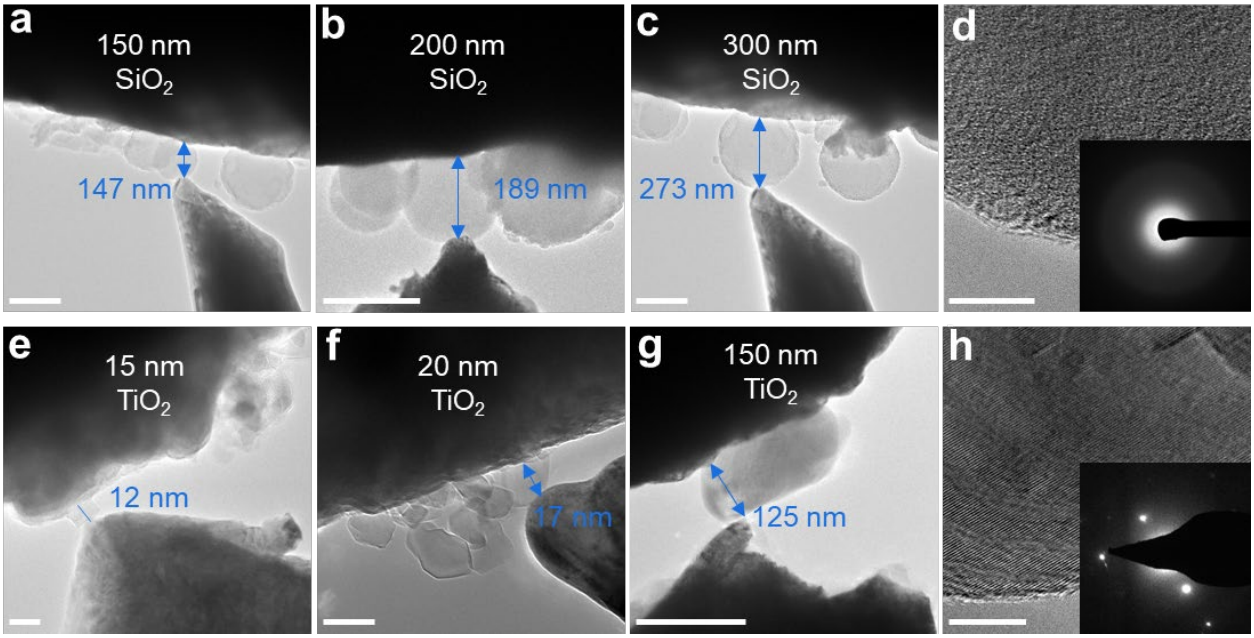

Supplementary Fig. 8 | TEM images showing the in situ probing electrical response measurements of (**a-d**) SiO_2 insulator and (**e-h**) TiO_2 semiconductor in the TEM. Scale bars, 200 nm in **a-c** and **g**, 10 nm in **d** and **h**, 20 nm in **e** and **f**.

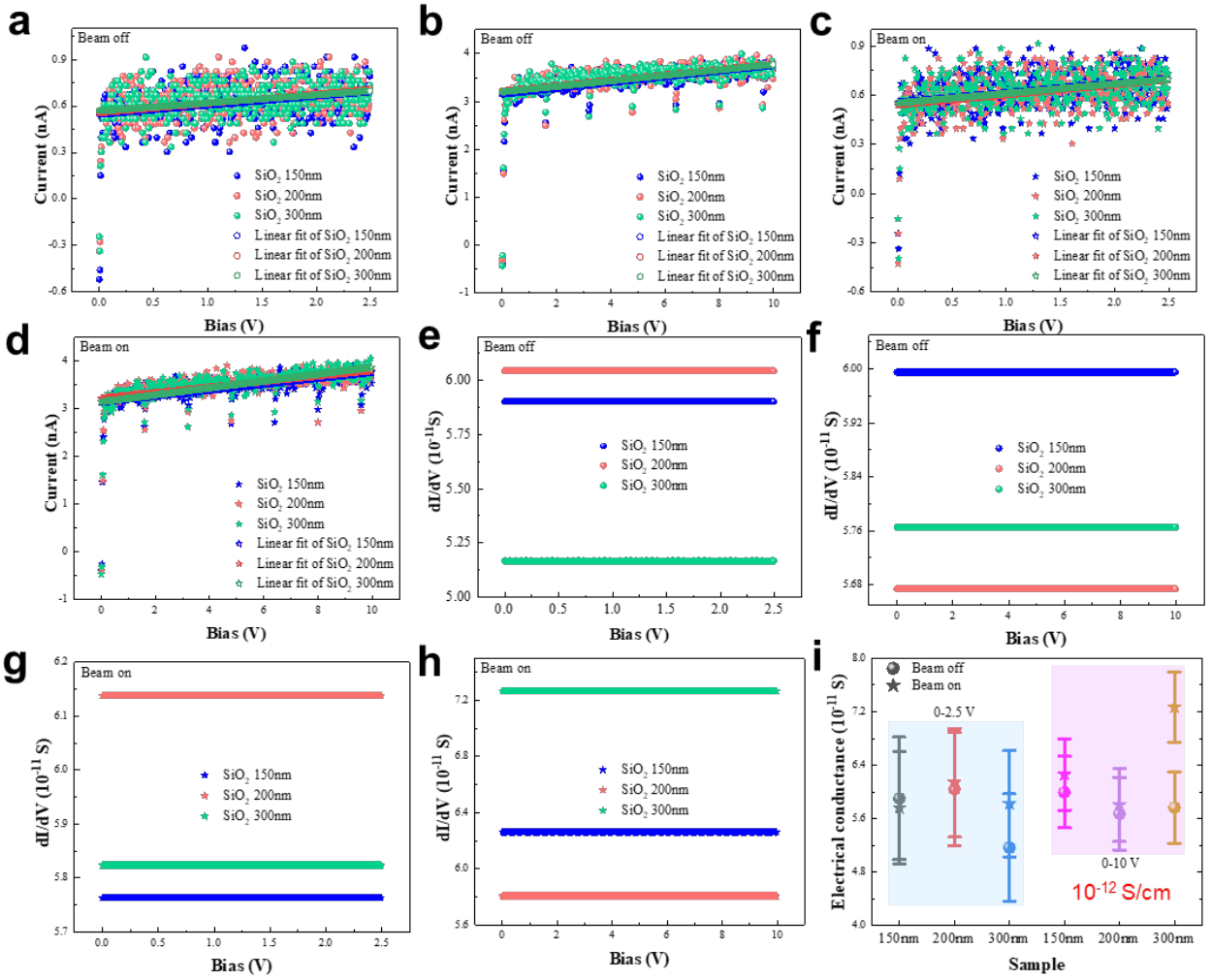

Supplementary Fig. 9 | Effect of bias range, electron beam, sample size on I-V curves and dI/dV-V curves taken from SiO_2 insulator. a,**b**, I-V curves measured from different size of SiO_2 nano particles under electron beam off condition with bias range from (**a**) 0-2.5 V and (**b**) 0-10 V. **c**,**d**, I-V curves measured from different size of SiO_2 nano particles under electron beam on condition with bias range from (**c**) 0-2.5 V and (**d**) 0-10 V. **e-h**, Differential conductance, dI/dV as function of V, derived from the above I-V curves (**a-d**). **i**, Summary of electrical conductance based on above dI/dV curves (**e-h**). Error bars, s.d. n=10. Inset: the normal electrical conductance of SiO_2.

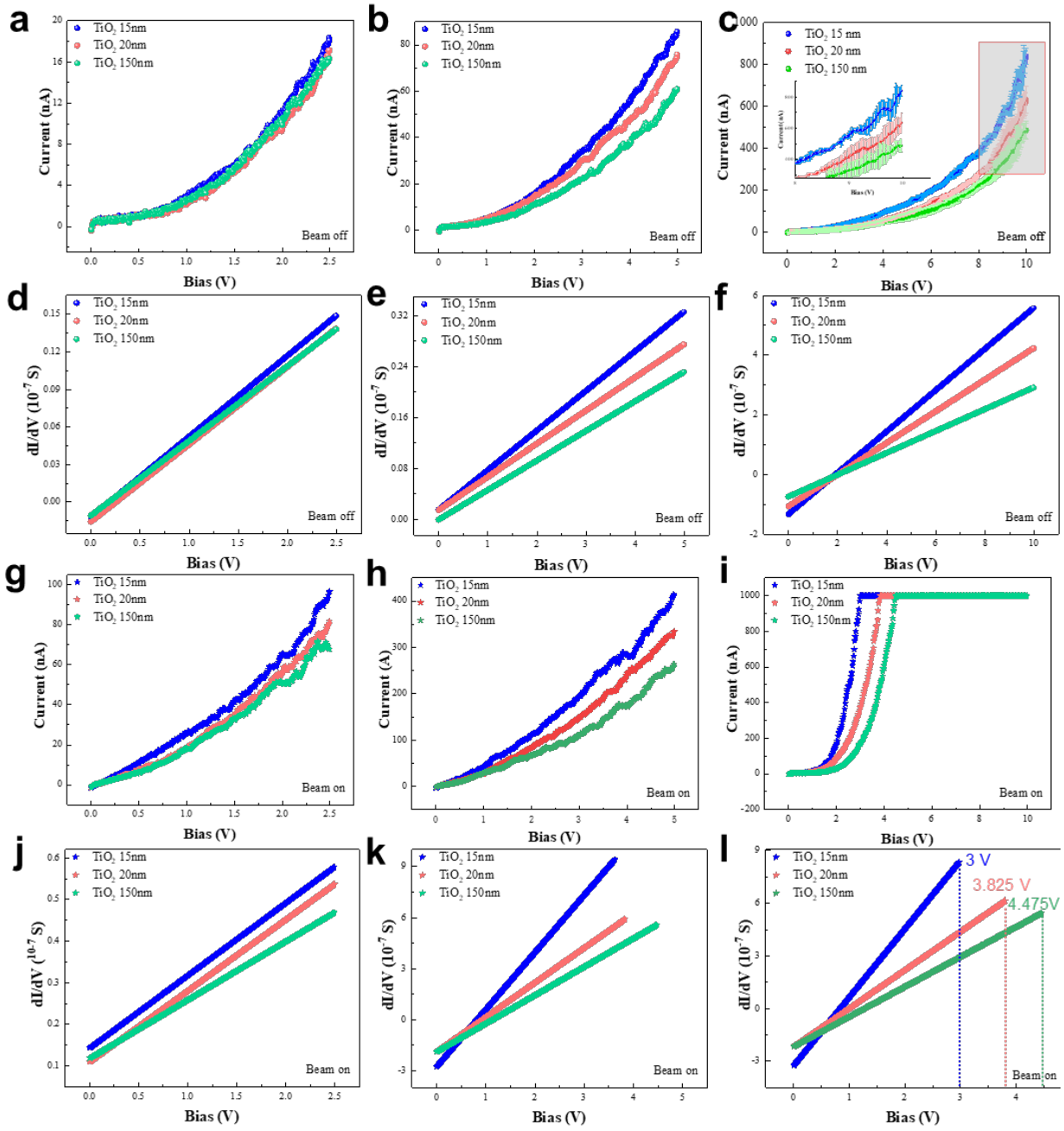

Supplementary Fig. 10 | Effect of bias range, electron beam, sample size on I-V curves and dI/dV-V curves taken from TiO_2 semiconductor. a-c, I-V curves measured from different size of TiO_2 nano particles under electron beam off condition with bias range from (**a**) 0-2.5 V, (**b**) 0-5 V and (**c**) 0-10 V. Error bars, s.d. n=10. Error bars in c show the reproducibility of measured I-V curves. **d-f**, Corresponding differential conductance derived from the above I-V curves (**a-c**). **g-i**, I-V curves measured from different size of TiO_2 nano particles under electron beam on condition with bias range from (**g**) 0-2.5 V, (**h**) 0-5 V and (**i**) 0-10 V. **j-l**, Corresponding differential conductance derived from the above I-V curves (**g-i**). Inset of **l**: critical voltage.

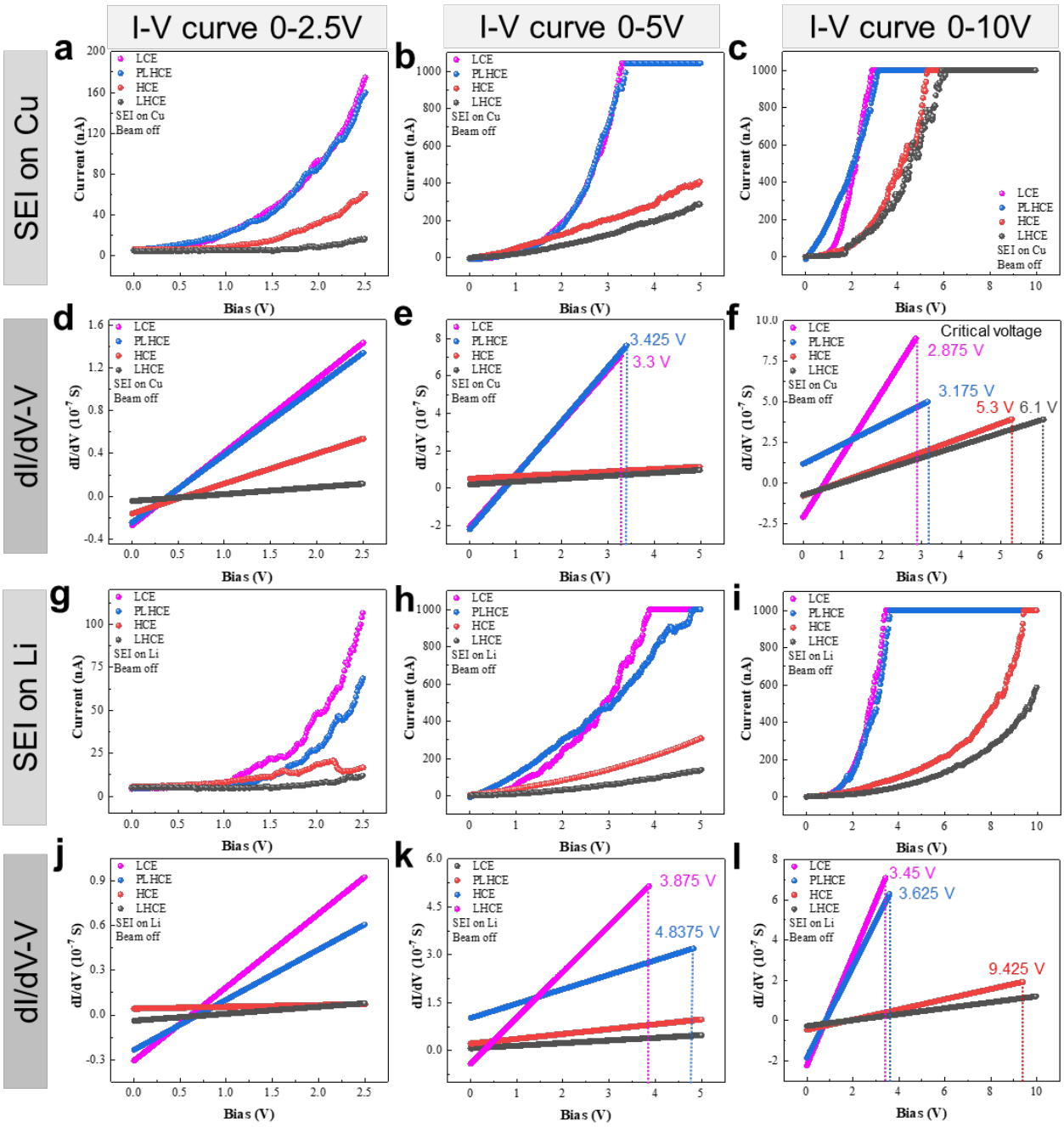

Supplementary Fig. 11 | Effect of bias range on I-V curves and dI/dV-V curves taken from SEI layers formed on Cu and Li. a-c, I-V curves measured from SEI on Cu formed in the different electrolytes under electron beam off condition with bias range from (**a**) 0-2.5 V, (**b**) 0-5 V and (**c**) 0-10 V. **d-f**, Corresponding differential conductance derived from the above I-V curves (**a-c**). **g-i**, I-V curves measured from SEI on Li formed in the different electrolytes under electron beam off condition with bias range from (**g**) 0-2.5 V, (**h**) 0-5 V and (**i**) 0-10 V. **j-l**, Corresponding differential conductance derived from the above I-V curves (**g-i**). Insets of **e-f** and **k-l**: critical voltage.

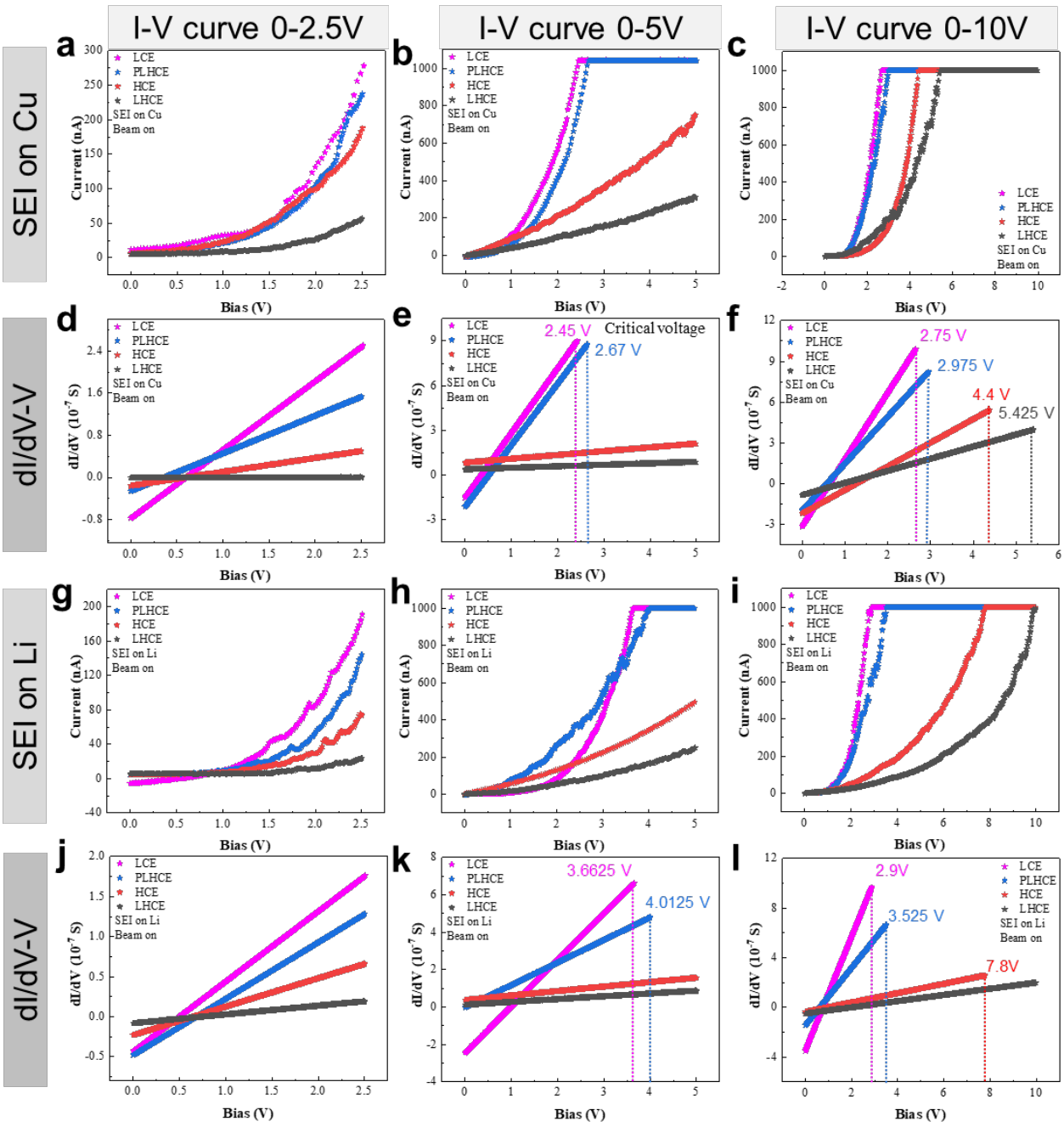

Supplementary Fig. 12 | Effect of electron beam on I-V curves and dI/dV-V curves taken from SEI layers formed on Cu and Li. a-c, I-V curves measured from SEI on Cu formed in the different electrolytes under electron beam on condition with bias range from (**a**) 0-2.5 V, (**b**) 0-5 V and (**c**) 0-10 V. **d-f**, Corresponding differential conductance derived from the above I-V curves (**a-c**). **g-i**, I-V curves measured from SEI on Li formed in the different electrolytes under electron beam on condition with bias range from (**g**) 0-2.5 V, (**h**) 0-5 V and (**i**) 0-10 V. **j-l**, Corresponding differential conductance derived from the above I-V curves (**g-i**). Insets of **e-f** and **k-l**: critical voltage.

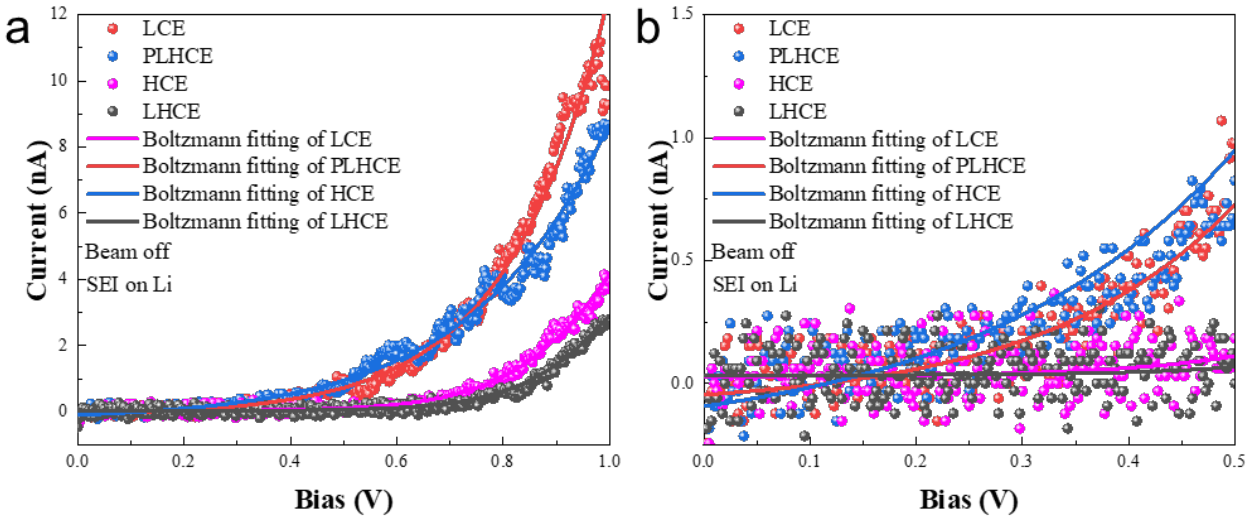

Supplementary Fig. 13 | Electrical transport measurements of SEI formed on the Li at low bias range (0-1 V). a, I-V curve of the SEI formed on Li at lower voltage range. **b**, Amplified low bias range (0-0.5 V).

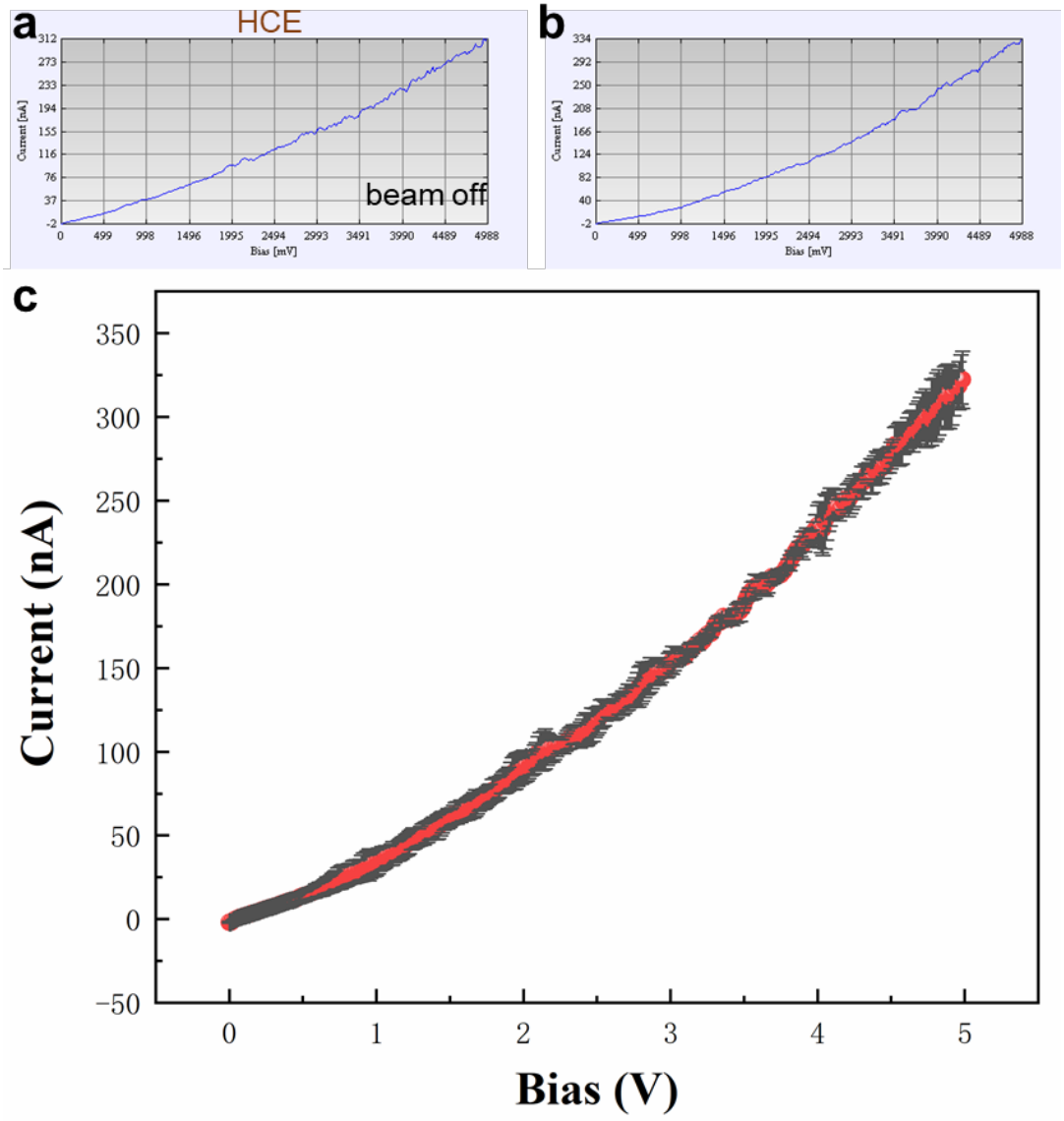

Supplementary Fig. 14 | Statistics analysis of measured I-V curve. a,**b**, I-V curves measured from same sample at different region. **c**, Averaged I-V curve with error bar. Error bars, s.d. n=10.

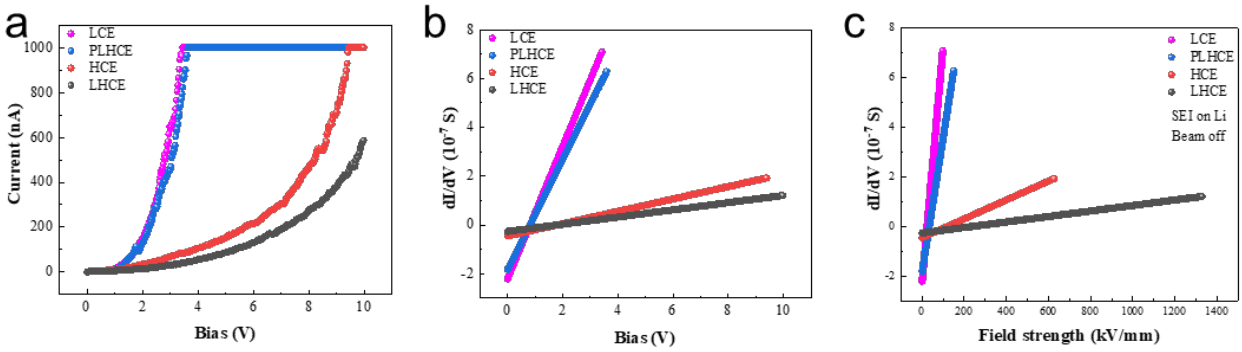

Supplementary Fig. 15 | Relationship between electrical differential conductance and electrical field strength based on the measured I-V curve. a, I-V curve acquired with bias range from 0-10 V. **b**, Calculated dI/dV-V curve based on I-V curve. **c**, The electrical differential conductance as a function of electrical field strength.

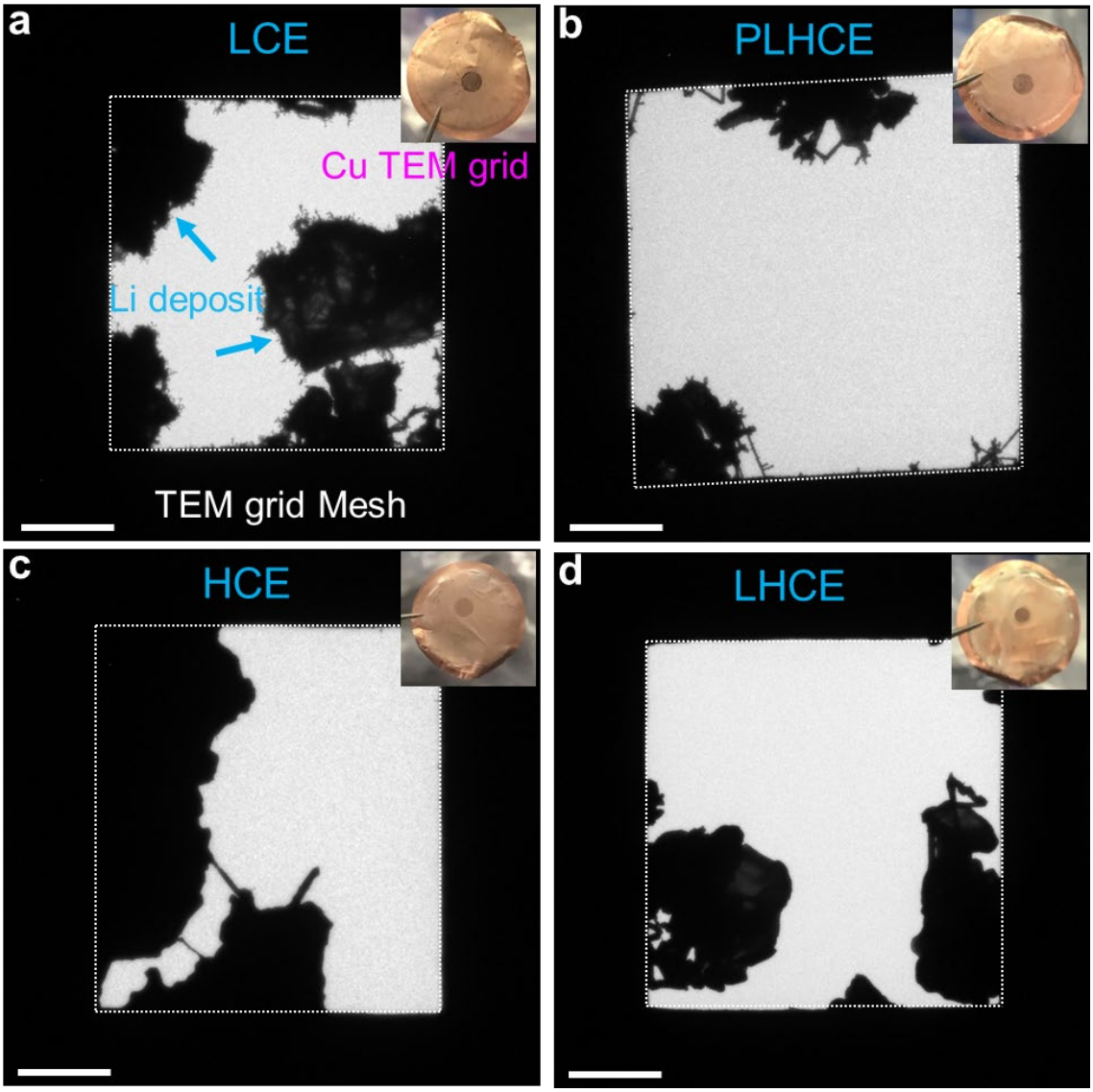

Supplementary Fig. 16 | Low magnification TEM images of Li deposits. **a**, LCE, **b**, PLHCE, **c**, HCE, and **d**, LHCE. Insets: Digital photos of deposited Li. Scale bar, 1 μm.

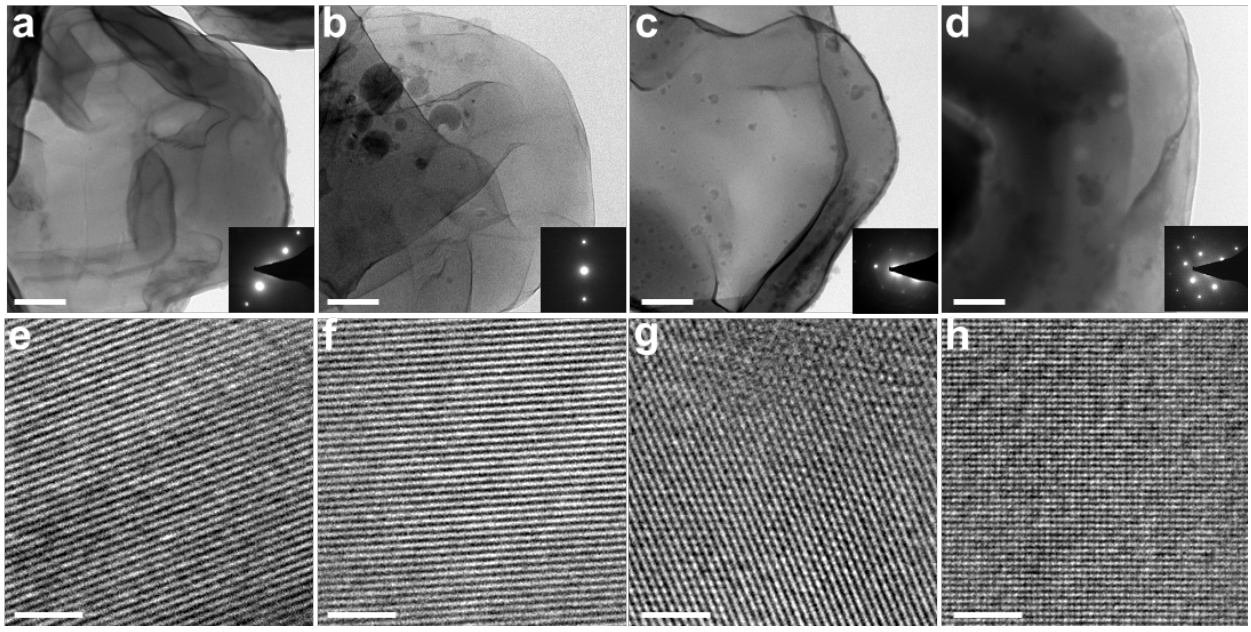

Supplementary Fig. 17 | Microstructures of Li deposits formed in the different electrolytes. **a-d**, Bright-field TEM images of Li deposits formed in (**a)** LCE, (**b)** PLHCE, (**c)** HCE, (**d**) LHCE; **e-h**, corresponding high-resolution TEM images of Li deposits formed in these different electrolytes. Insets are corresponding SAED patterns. Scale bars, 1 μm in **a-d**, 5 nm in (**e-h)**.

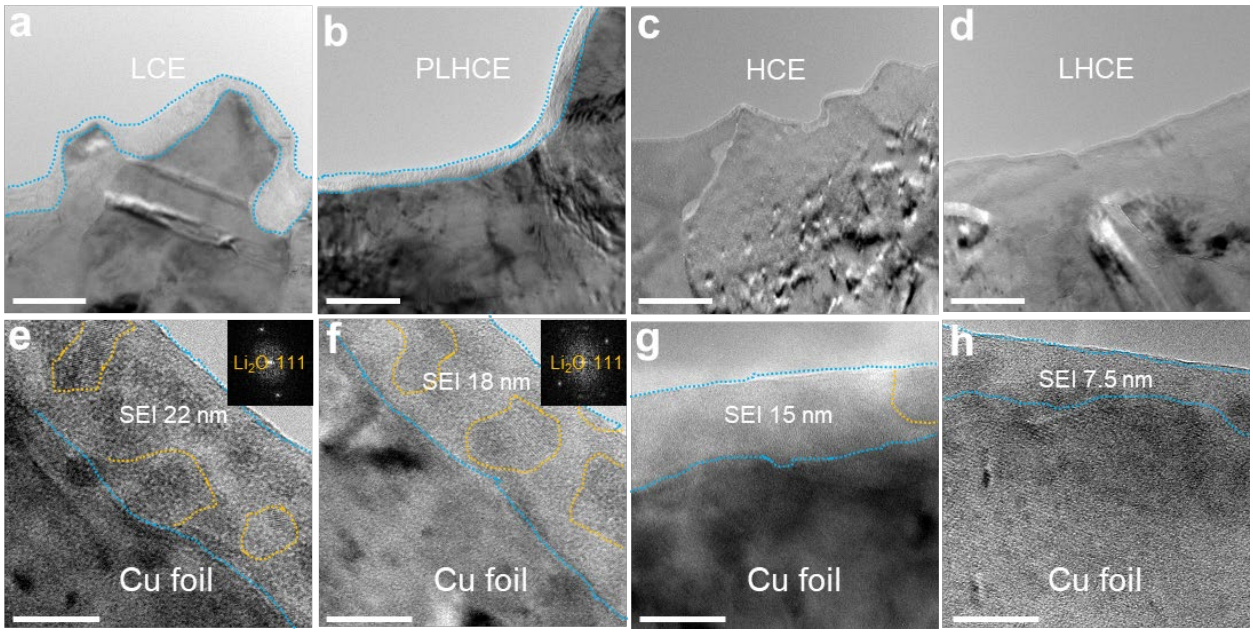

Supplementary Fig. 18 | Cryo-TEM characterization of SEI layer on Cu. a-d, Morphology and (**e-h**) atomic structure of SEI layers on the Cu foil. Scale bars, 50 nm in **a-d**, 10 nm in **e-h**.

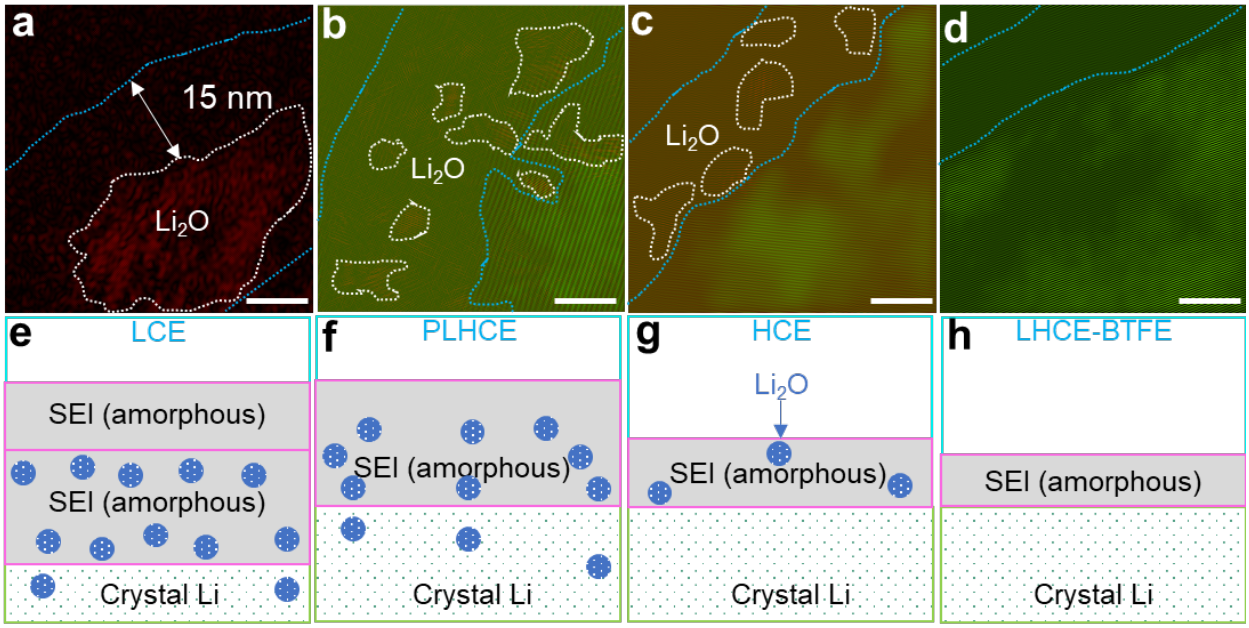

Supplementary Fig. 19 | Cryo-TEM characterization of SEI layer on Li using different electrolyte. a-d, Corresponding invert FFT images of Fig. 4a. **e-h**, Schematic of the observed SEIs on the Li deposits formed in LCE, HCE, PLHCE, and LHCE, separately. Scale bar: 5 nm in **a-d**.

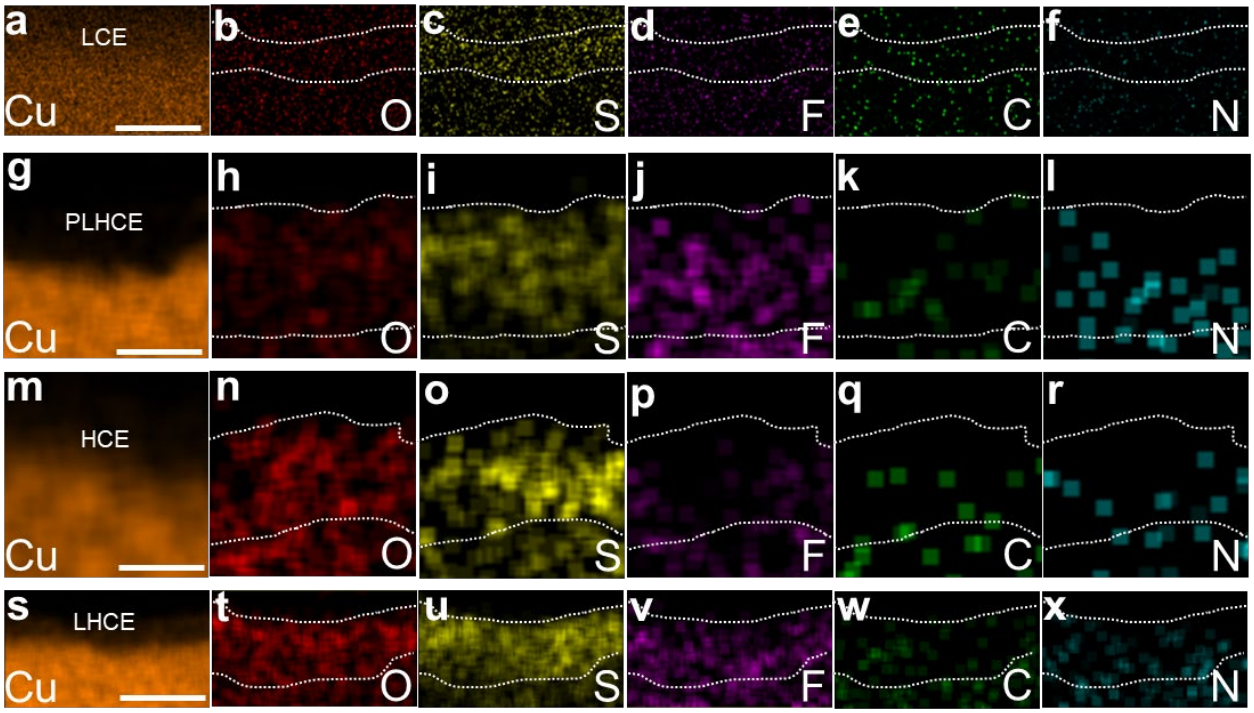

Supplementary Fig. 20 | Composition information acquired from the SEI layers on the Cu foil formed in the different electrolytes. Scale bars, 50 nm in **a-f** and 10 nm in **g-x**.

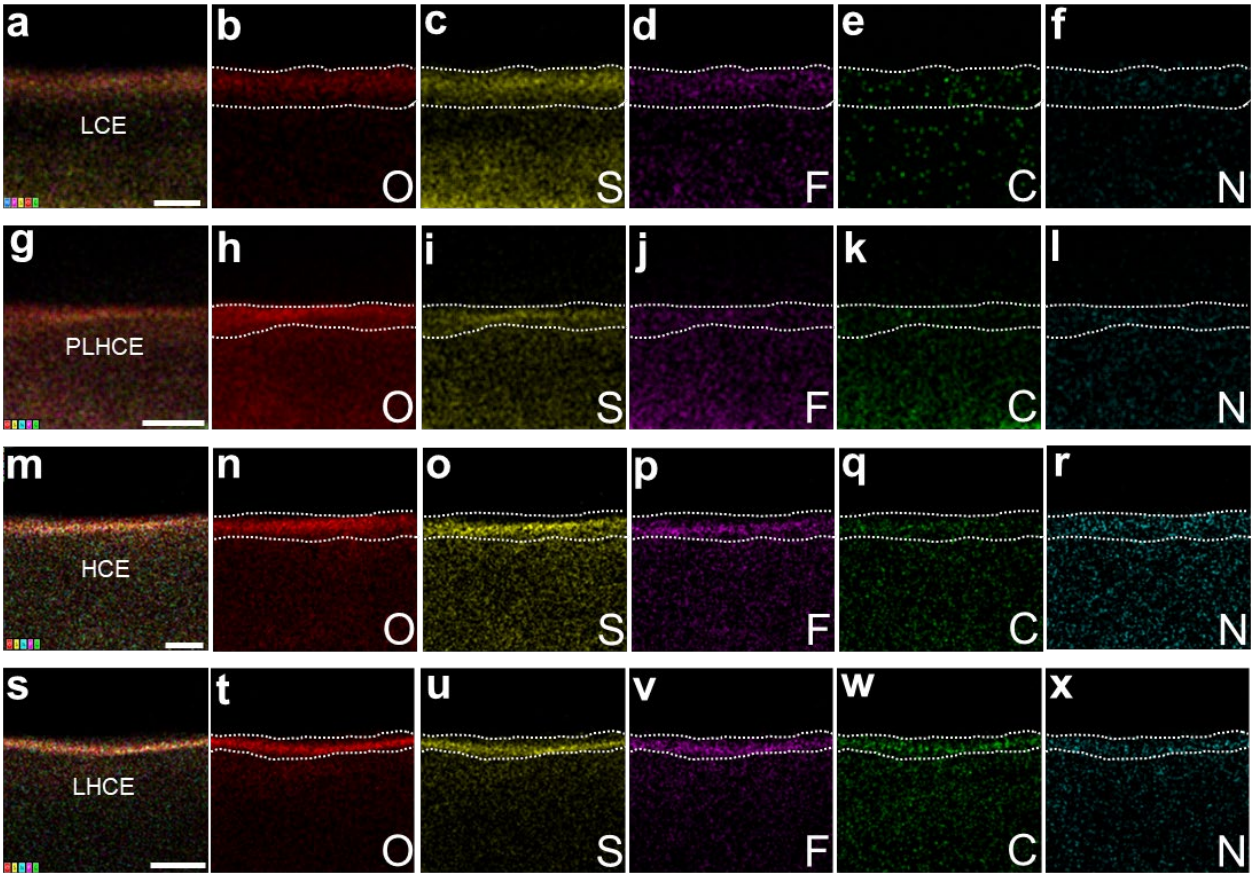

Supplementary Fig. 21 | Composition information acquired from the SEI layers on the Li deposits formed in the different electrolytes. Scale bars, 50 nm in **a-l** and 20 nm in **m-x**.

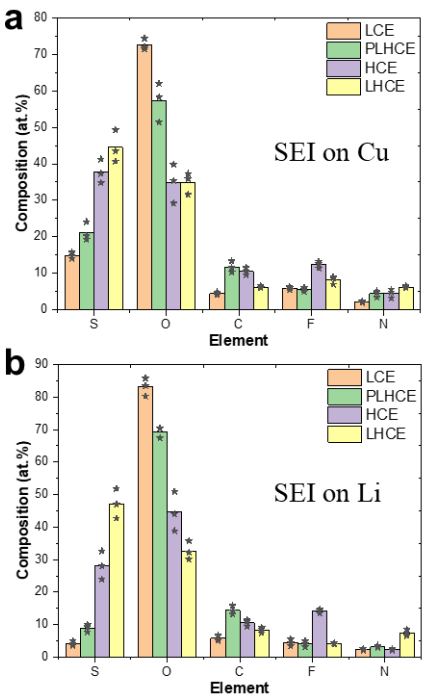

Composition / Electrolyte	S (at.%)	O (at.%)	C (at.%)	F (at.%)	N (at.%)
LCE	14.8	72.6	4.5	5.9	2.2
PLHCE	21.2	57.2	11.7	5.5	4.4
HCE	37.8	34.8	10.5	12.4	4.5
LHCE	44.5	34.9	6.2	8.2	6.2

Composition / Electrolyte	S (at.%)	O (at.%)	C (at.%)	F (at.%)	N (at.%)
LCE	4.2	83.2	5.8	4.4	2.4
PLHCE	9.0	69.4	14.4	4.0	3.2
HCE	28.2	44.6	10.6	14.2	2.4
LHCE	47.2	32.7	8.4	4.2	7.5

Supplementary Fig. 22 | Composition information of SEI layer acquired using STEM-EDS. SEI on the (**a**) Cu foil and (**b**) Li deposits formed in the different electrolytes. The black stars represent individual data points, and the bar signifies the mean value derived from three measurements, which are also shown in tables.

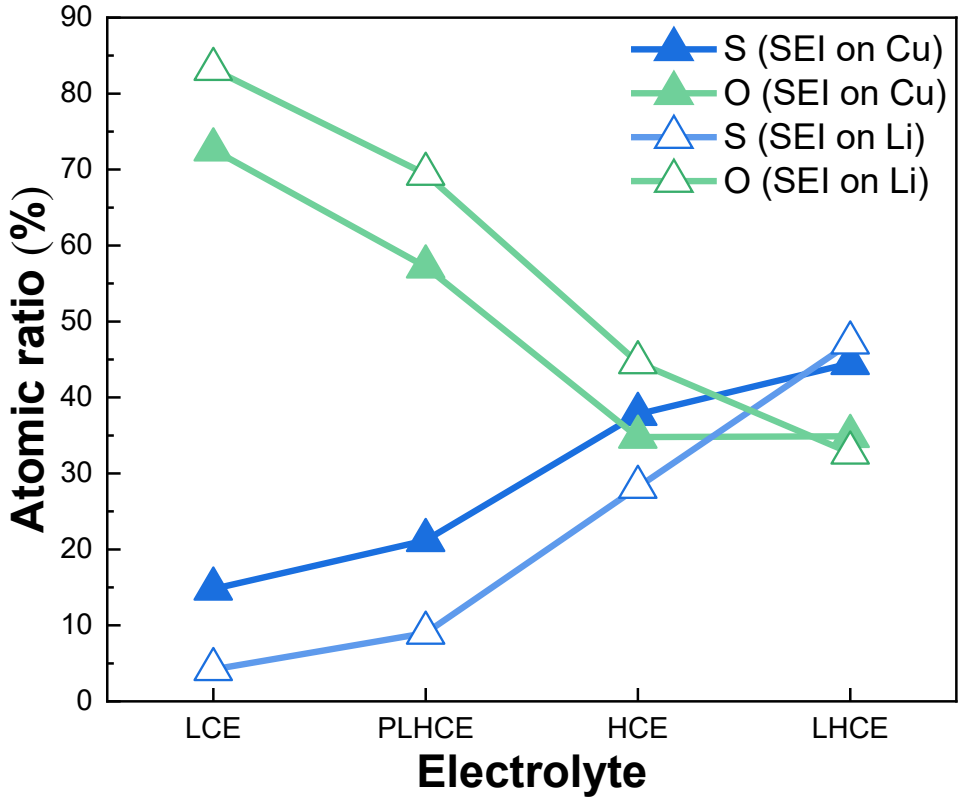

Supplementary Fig. 23 | Atomic fraction of O and S ratio of SEI layers formed in different electrolytes.

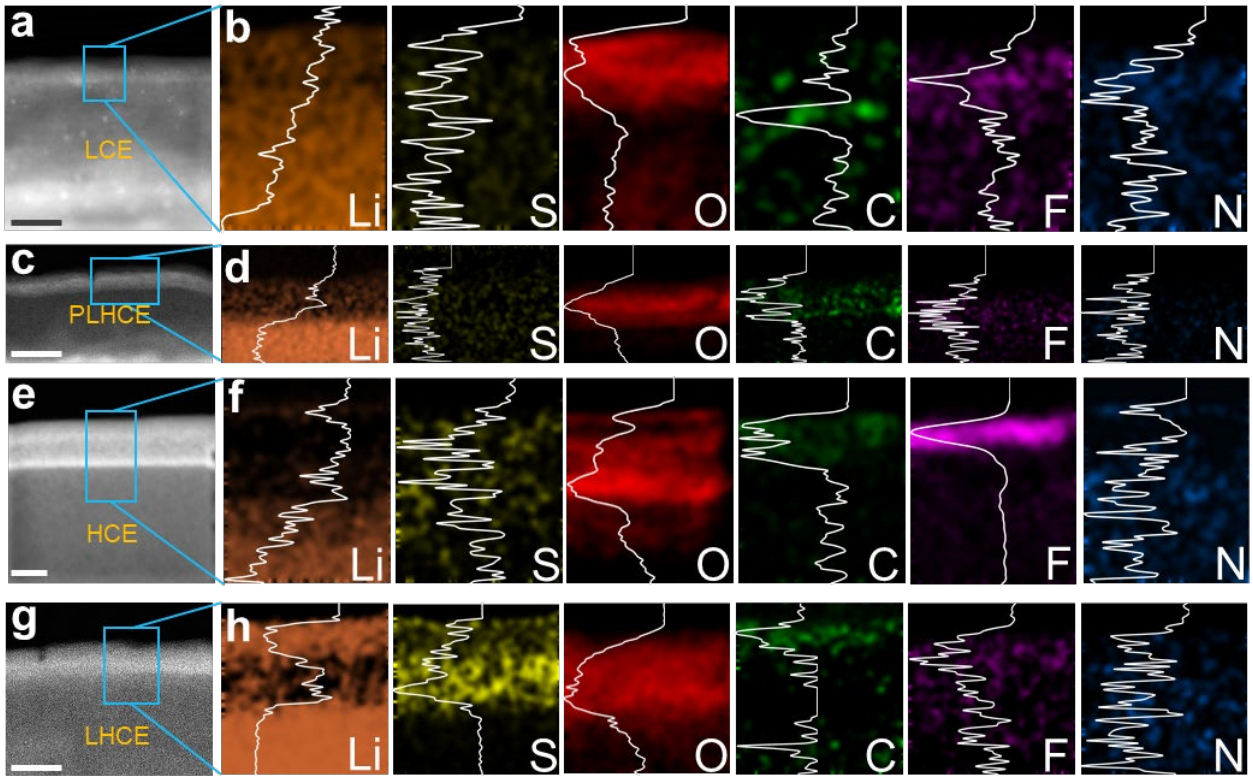

Supplementary Fig. 24 | Structure and elemental composition of Li deposits and their SEIs formed in the different electrolytes. a, Cryo-HAADF-STEM imaging and corresponding (**b**) EELS elemental mapping show the spatial distribution of Li, S, O, C, F, and N in the Li deposit and SEI layer formed in LCE. **c**, Cryo-HAADF-STEM imaging and corresponding (**d**) EELS elemental mapping show the spatial distribution of Li, S, O, C, F, and N in the Li deposit and SEI layer formed in PLHCE. **e**, Cryo-HAADF-STEM imaging and corresponding (**f**) EELS elemental mapping show the spatial distribution of Li, S, O, C, F, and N in the Li deposit and SEI layer formed in HCE. **g**, Cryo-HAADF-STEM imaging and corresponding (**h**) EELS elemental mapping show the spatial distribution of Li, S, O, C, F, and N in the Li deposit and SEI layer formed in LHCE. Insets: line profiles of EELS maps show intensity changes from Li to SEI layer. Scale bars, 50 nm in **a** and **c**, and 10 nm in **e** and **g**.

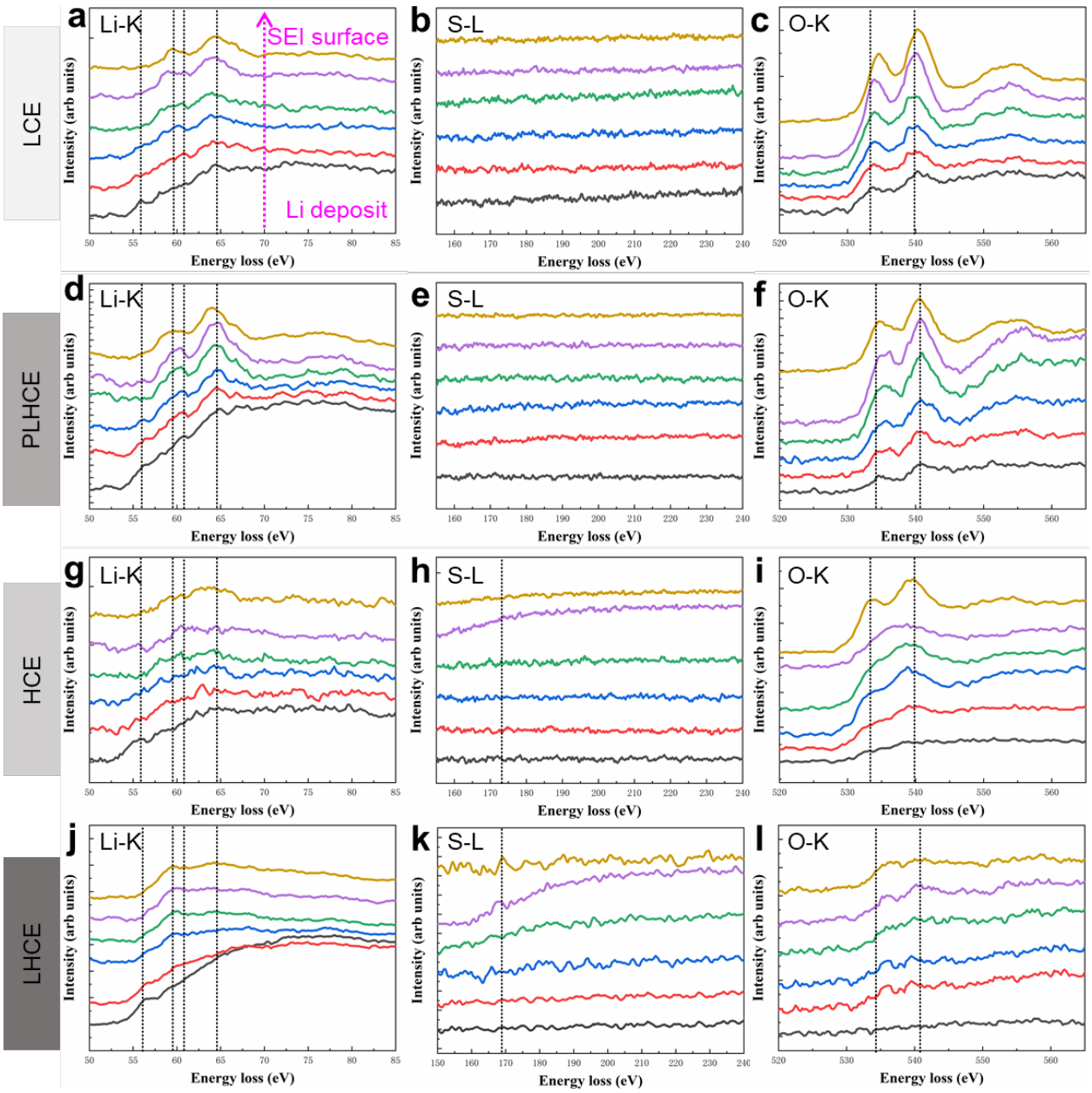

Supplementary Fig. 25 | Analysis of the chemical bonding environment from Li deposits to SEI layers. The EELS of Li K-edge, S L-edge, and O K-edge spectrums acquired from Li deposit to SEI surface in (**a-c**) LCE, (**d-f**) PLHCE, (**g-i**) HCE, and (**j-l**) LHCE.

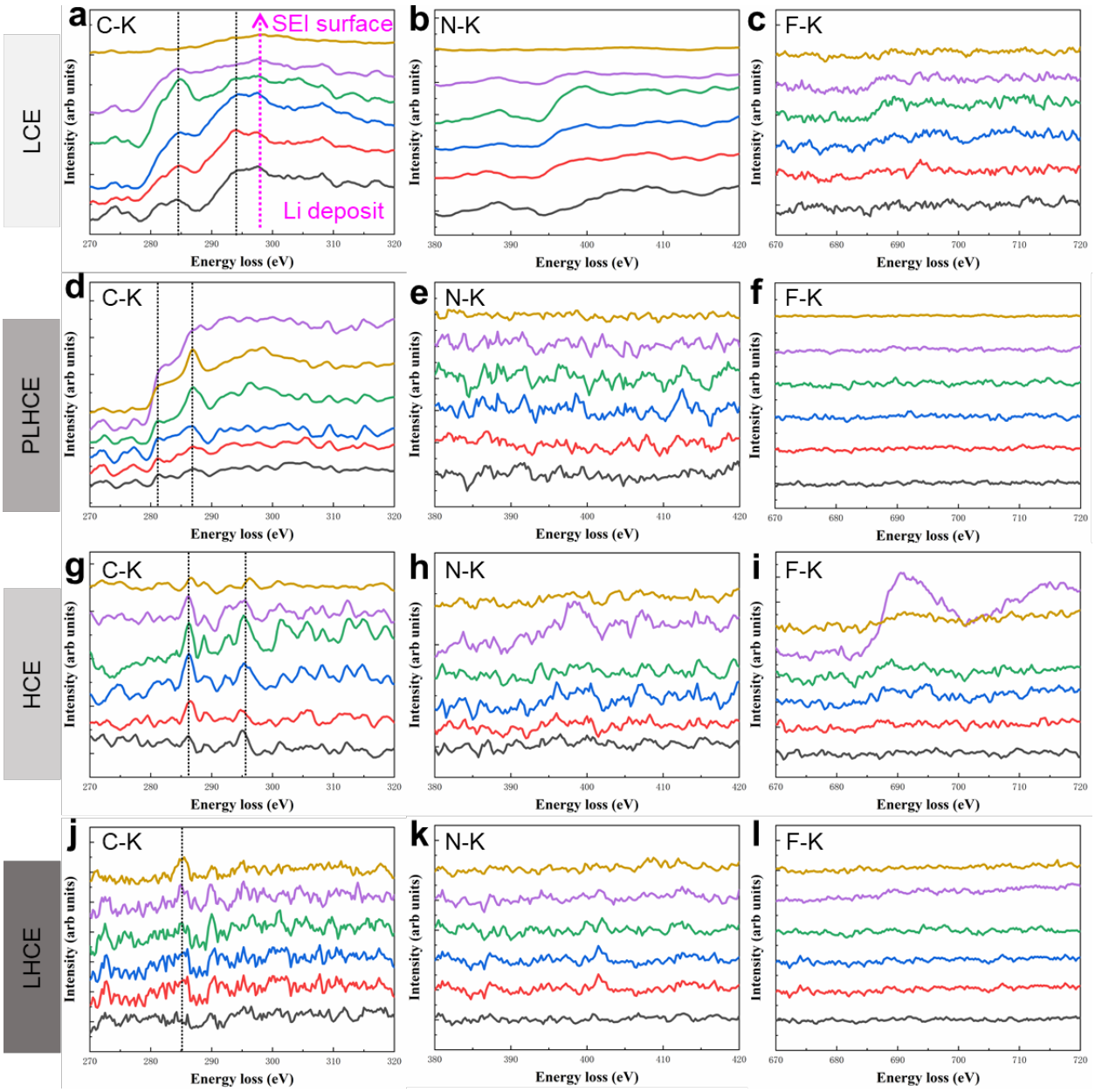

Supplementary Fig. 26 | Analysis of the chemical bonding environment from Li deposits to SEI layers. The EELS of C K-edge, N K-edge, and F K-edge spectrums acquired from Li deposit to SEI surface in (**a-c**) LCE, (**d-f**) LHCE, (**g-i**) HCE, and (**j-l**) LHCE.

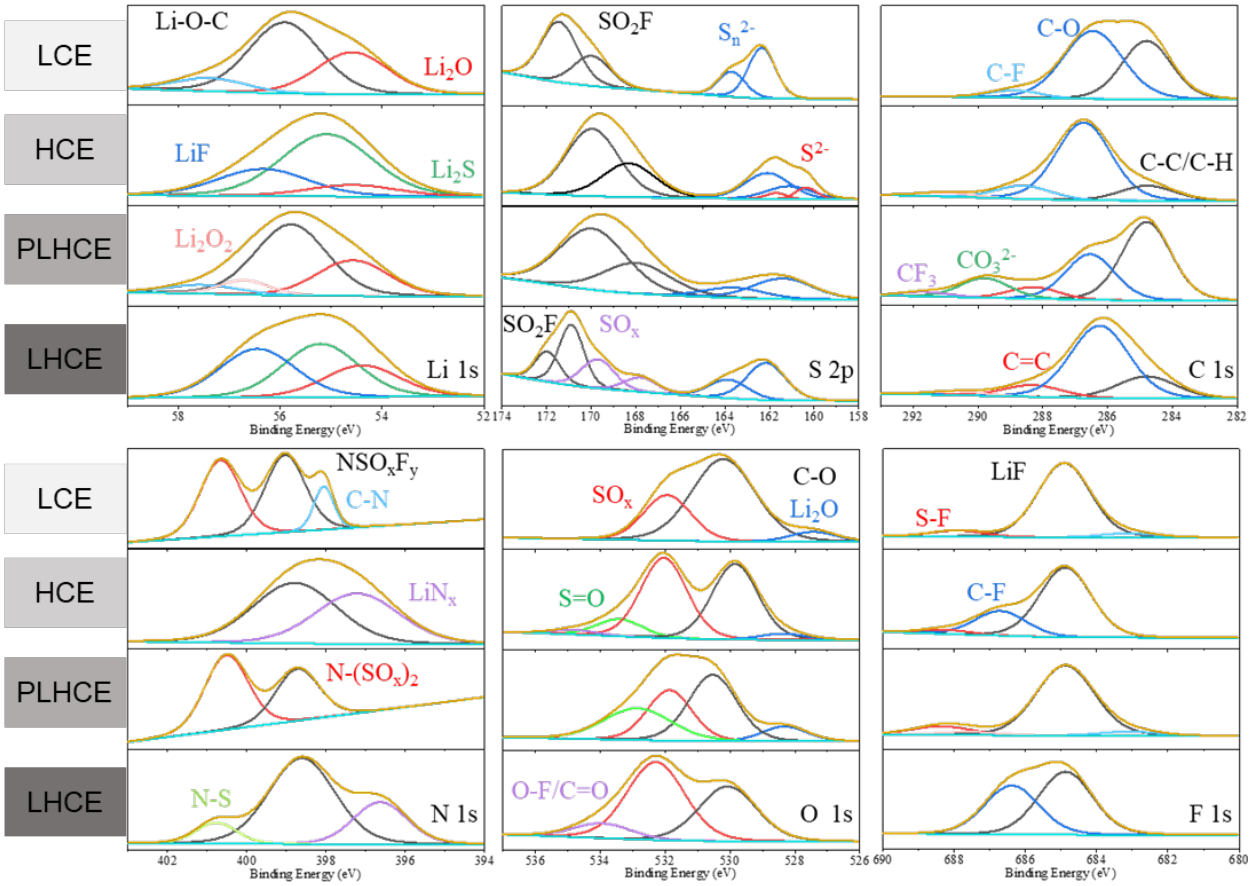

Supplementary Fig. 27 | The XPS spectra for selected elements from the surface of Li deposits.

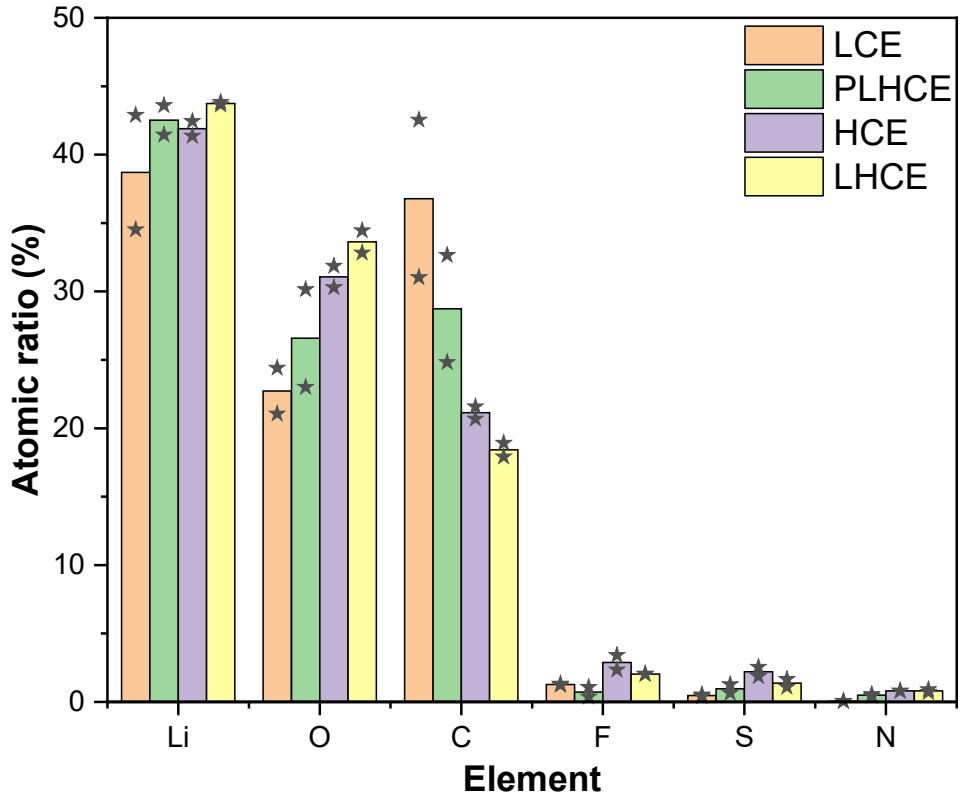

Supplementary Fig. 28 | The XPS atomic ratios of different elements on Li deposits formed in the different electrolytes. The grey stars represent individual data points, and the bar signifies the mean.

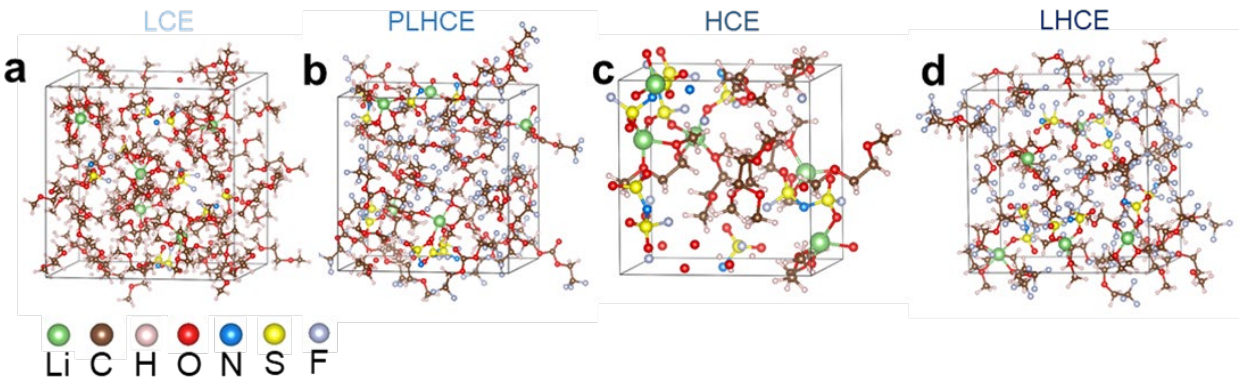

Supplementary Fig. 29 | The molecular structures and snapshots of the electrolytes from AIMD simulations. a, LCE, **b,** PLHCE, **c,** HCE[10] and **d,** LHCE[10].

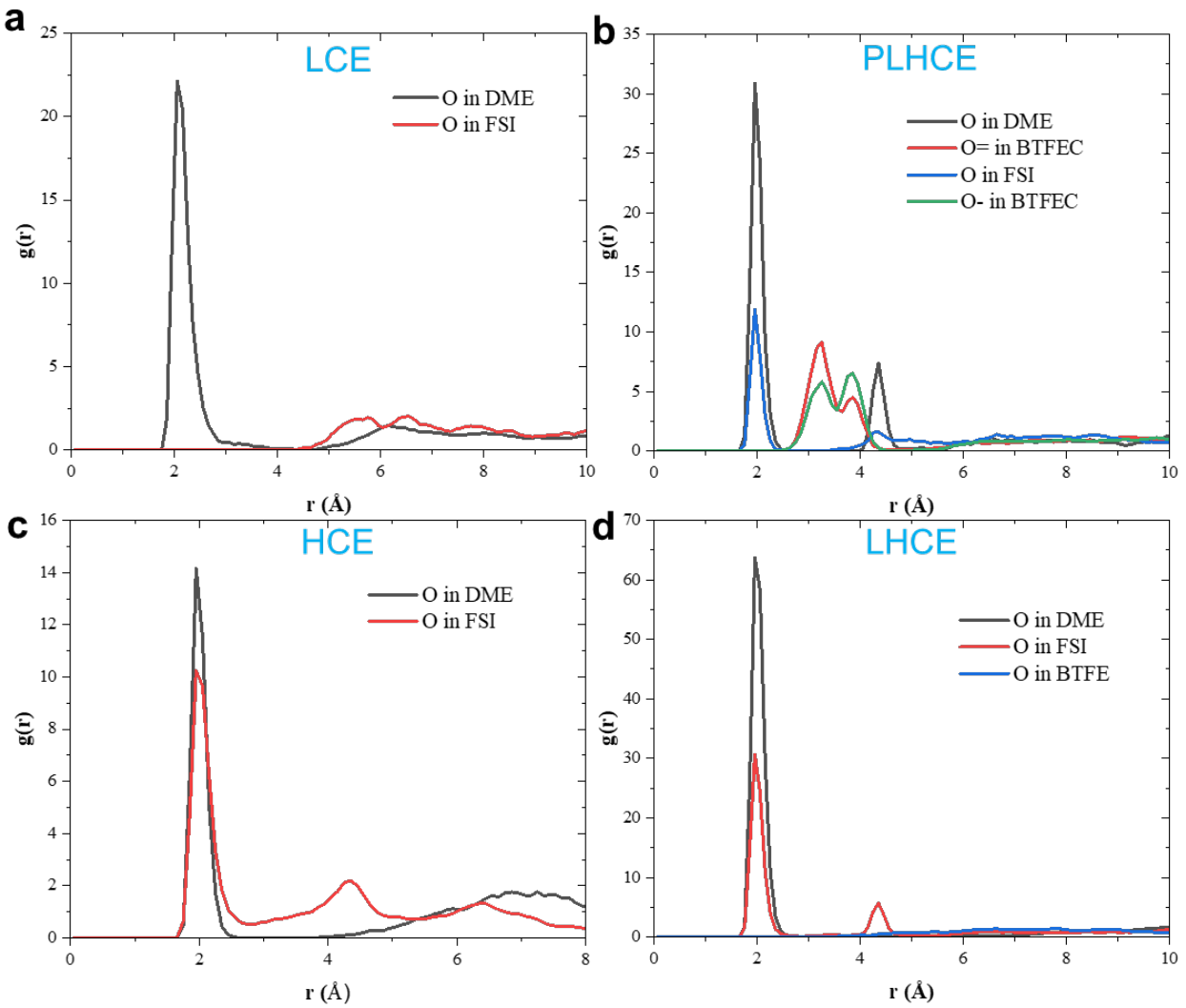

Supplementary Fig. 30 | AIMD simulated radial distribution of electrolytes. **a**, LCE, **b**, PLHCE[10], **c**, HCE, and **d**, LHCE[10].

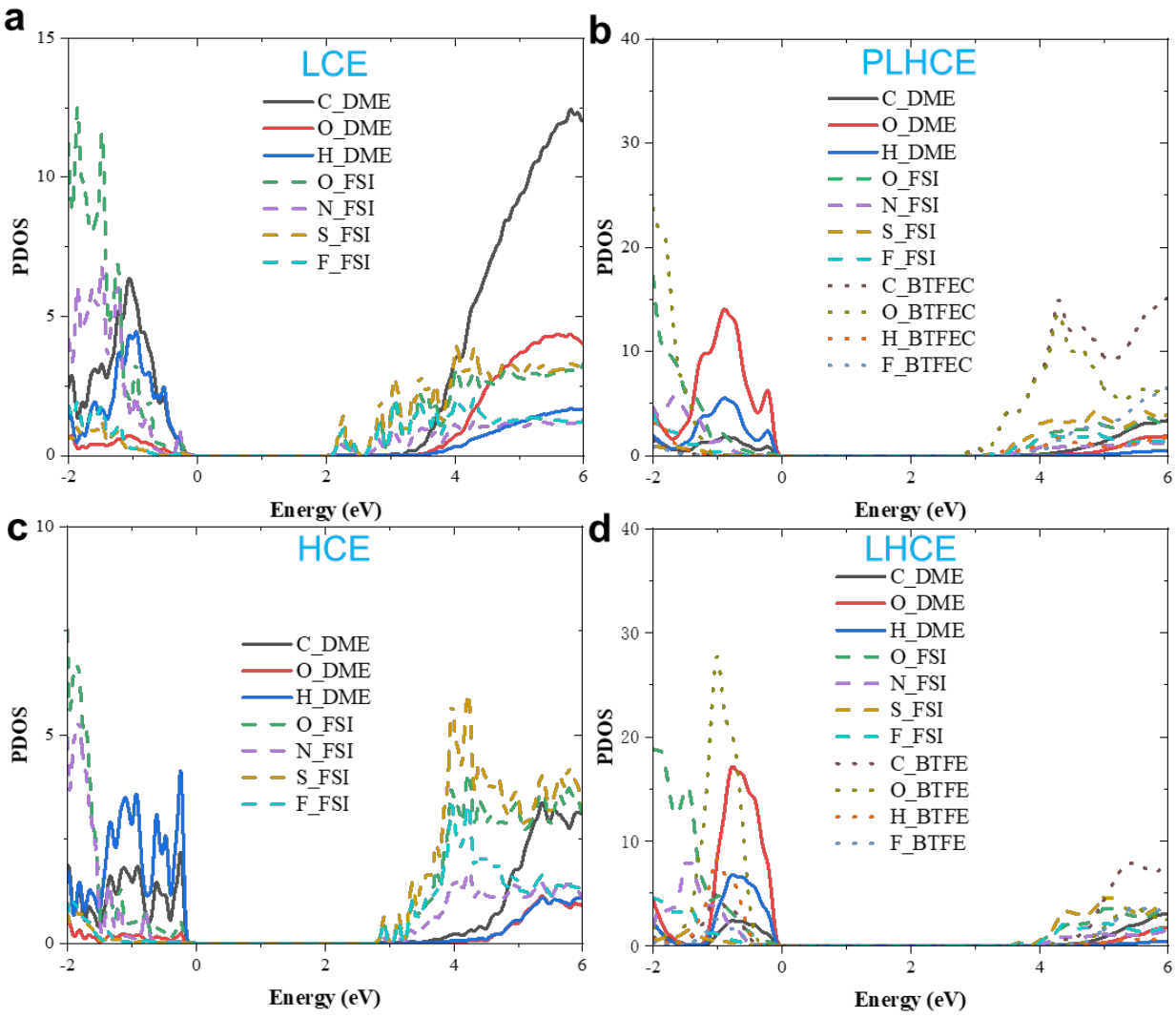

Supplementary Fig. 31 | Projected density of states (PDOS) of electrolytes. a, LCE, **b**, PLHCE[10], **c**, HCE, and **d**, LHCE[10].

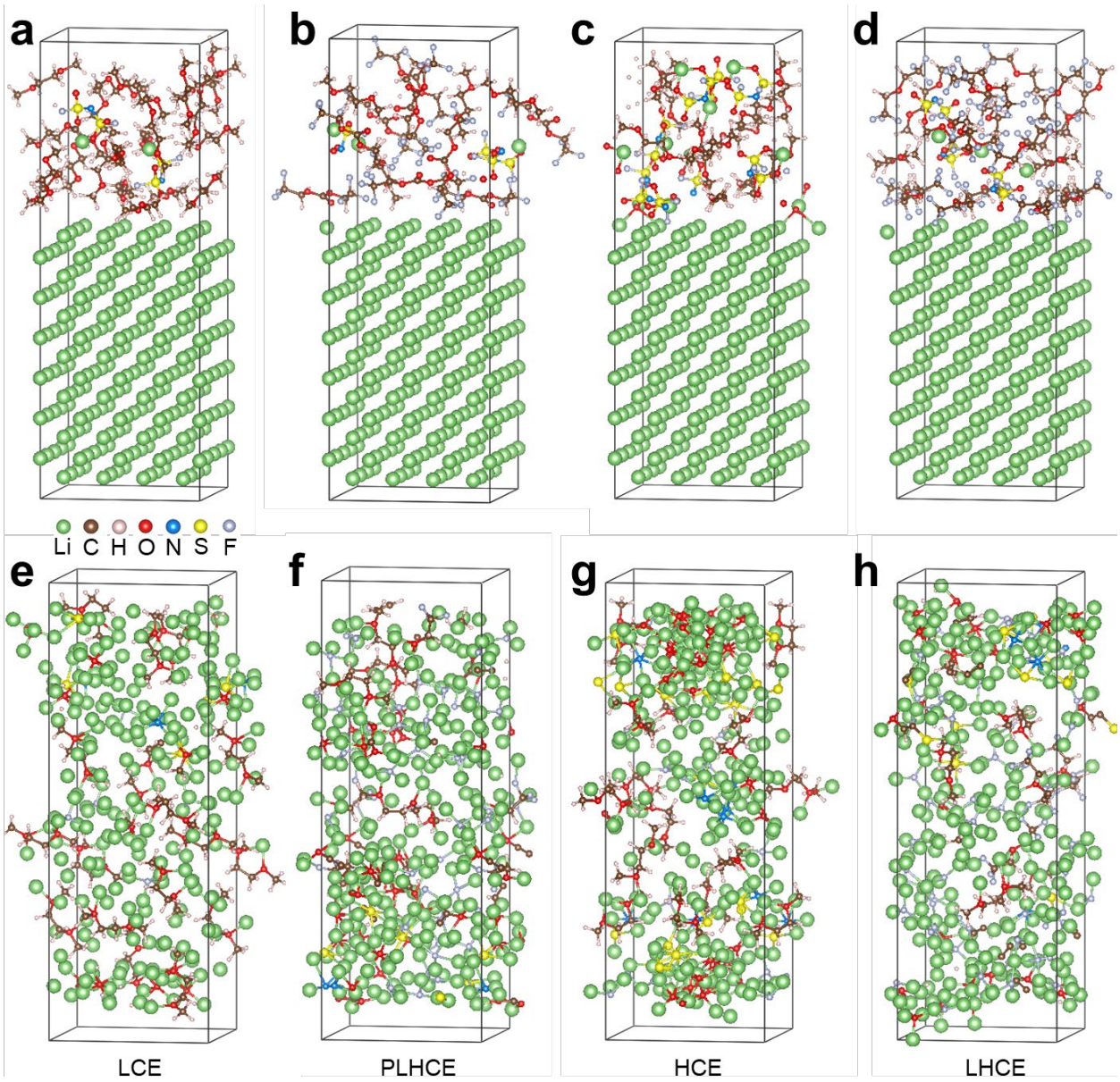

Supplementary Fig. 32 | Simulation snapshots of initial and final states. Snapshots of initial state of (**a**) LCE, (**b**) PLHCE, (**c**) HCE and (**d**) LHCE with Li metal. **e**,**f**, Corresponding final states of SEI formed by reacting between four electrolytes with Li metal. E/A ratio is 0.75.

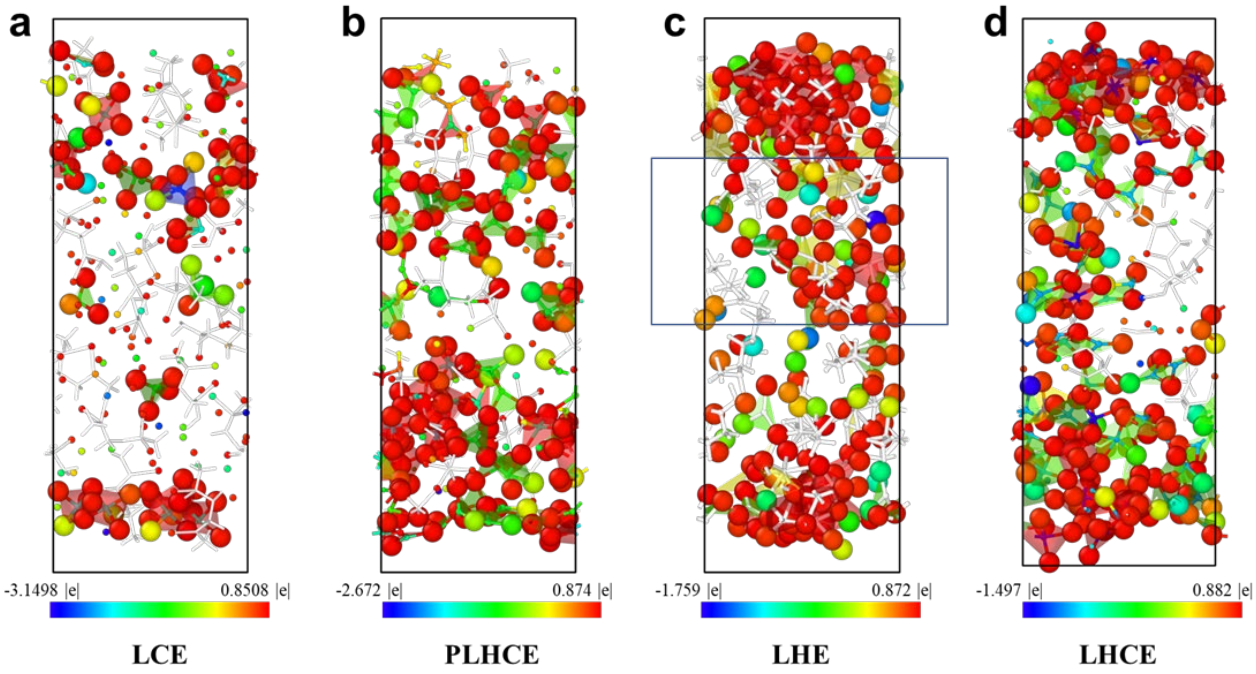

Supplementary Fig. 33 | Bader Charges for Li atoms in SEI formed in four electrolytes. E/A ratio is 0.75. Note: The Li^+ ions with a smaller radius are dissolved Li^+ ions.

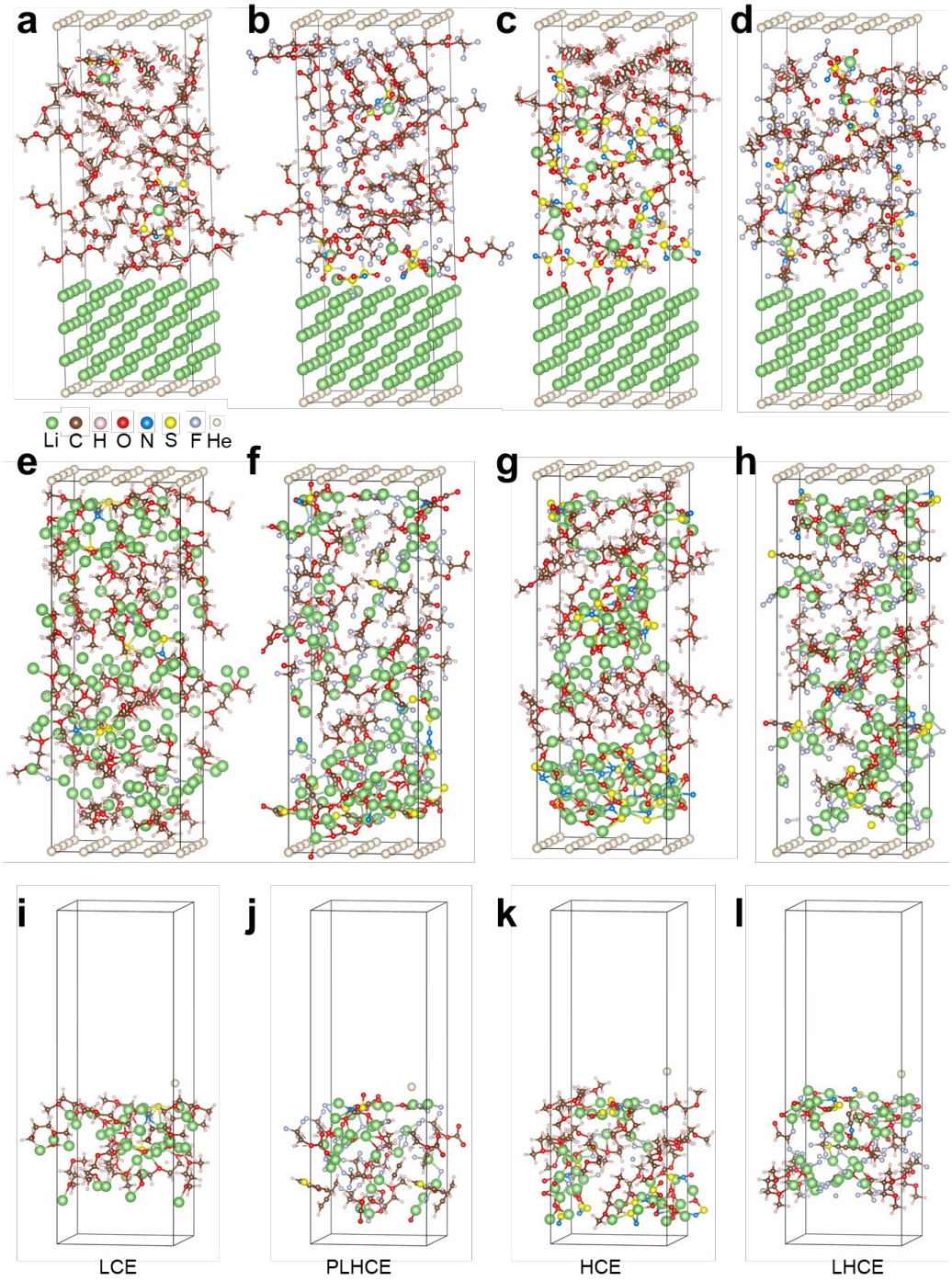

Supplementary Fig. 34 | Simulation snapshots of initial and final states. a-d, Simulation snapshots of initial states of (**a**) LCE, (**b**) PLHCE, (**c**) HCE and (**d**) LHCE with Li metal. **e**,**f**, Simulation snapshots of final states of SEI formed by reacting between (**e**) LCE, (**f**) PLHCE, (**g**) HCE and (**h**) LHCE and Li metal. **i-l**, Sample snapshots of four electrolytes reacting with Li metal. E/A ratio is 2.79. He atom is used as boundary during simulation.

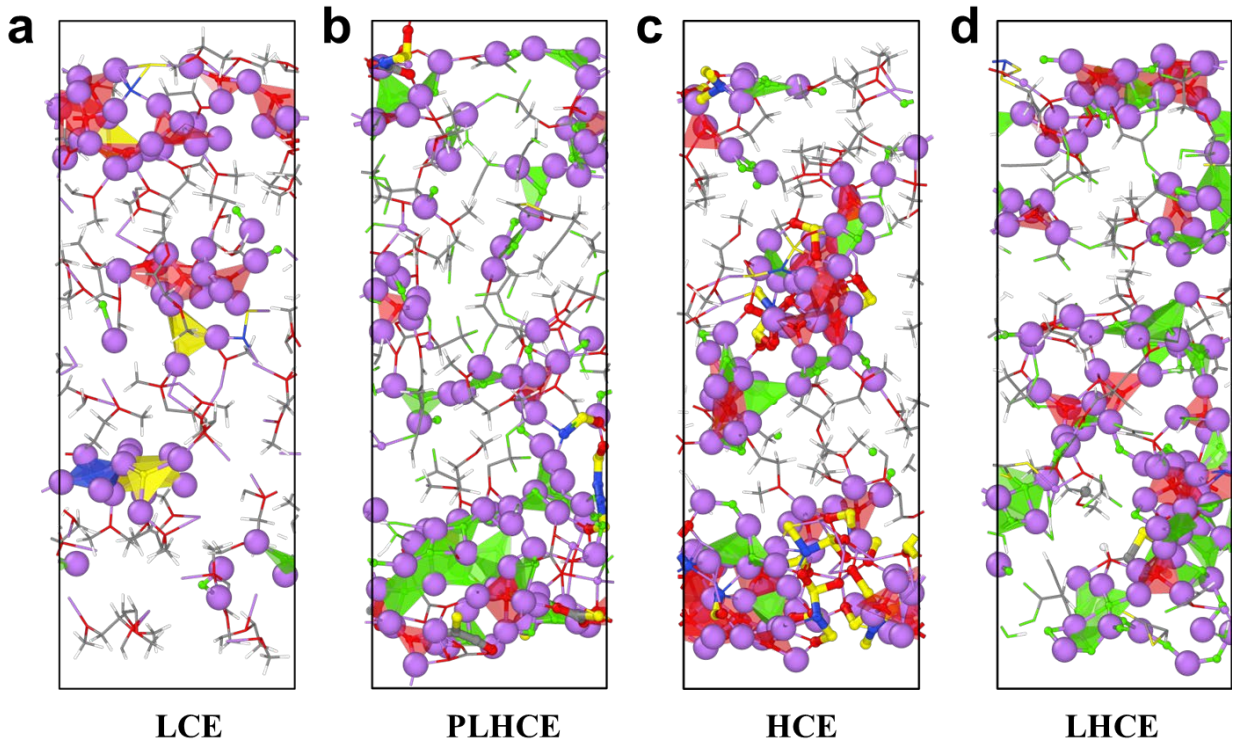

Supplementary Fig. 35 | Bader Charges for Li atoms in SEI formed in four electrolytes. E/A ratio is 2.79. Note: The Li^+ ions with a smaller radius are dissolved Li^+ ions.

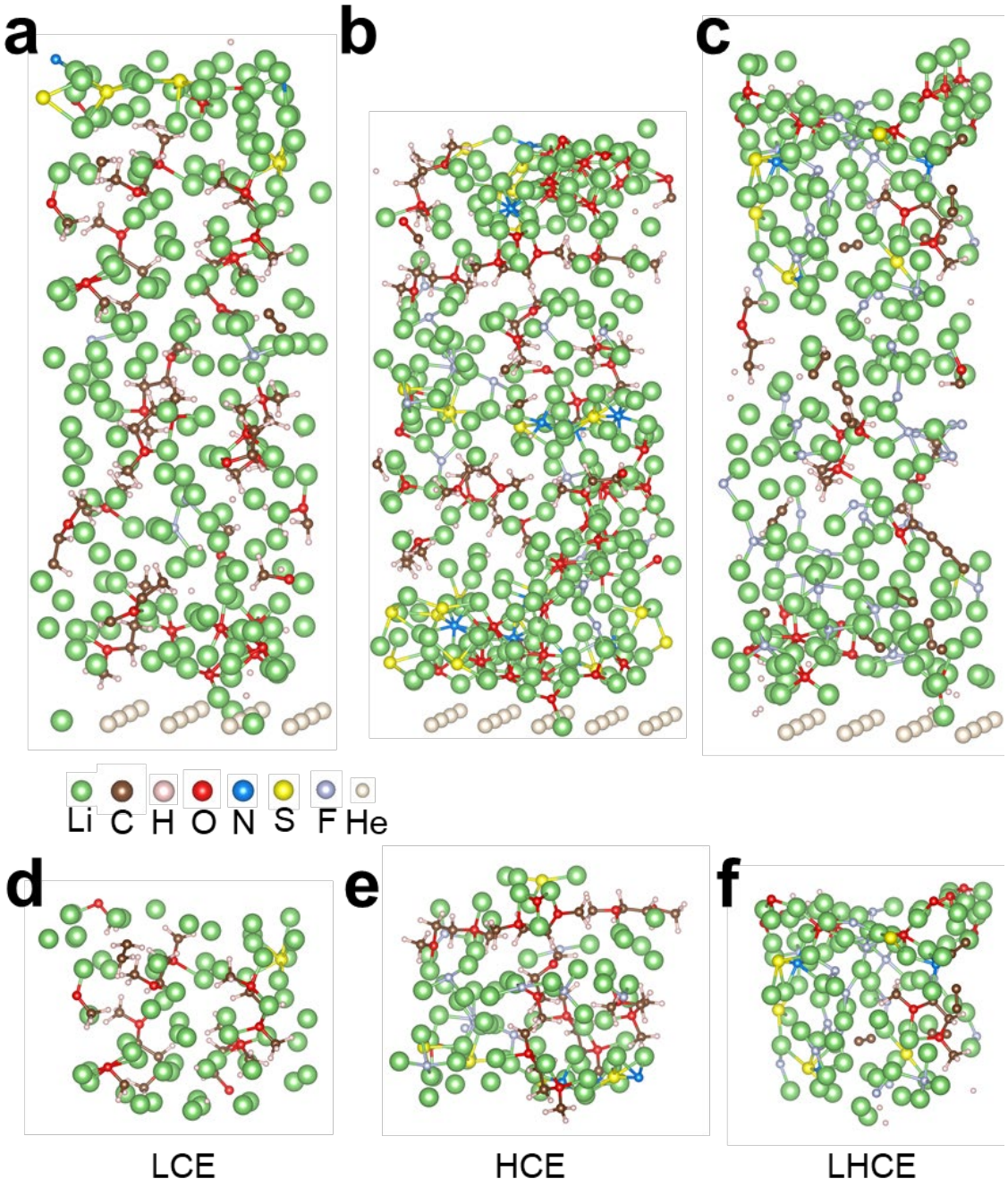

Supplementary Fig. 36 | Simulation snapshots of SEI layer. a-c, Simulation snapshots of initial states of (**a**) LCE (E/A ratio is 0.75 and total simulation time is 1 ns), (**b**) HCE (E/A ratio is 0.75 and total simulation time is 253 ps with larger sample size) and (**c**) LHCE (E/A ratio is 0.75 and total simulation time is 1 ns) with Li metal. **d-f**, Sample snapshots of three electrolytes reacting with Li metal. He atom is used as boundary during simulation.

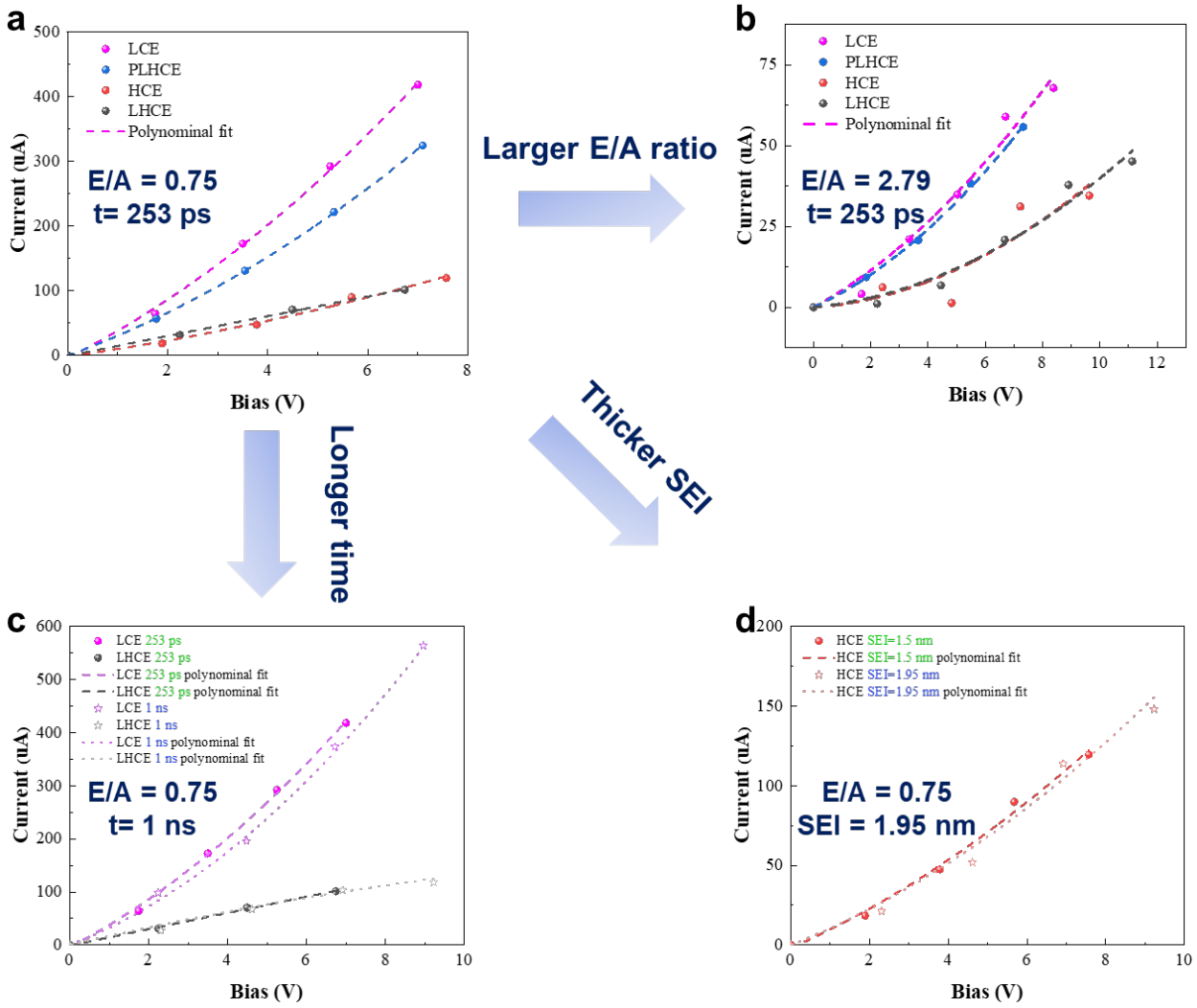

Supplementary Fig. 37 | Calculated I-V curve with different electrolyte/anode (E/A) ratio and simulation time (t). **a**, Calculated I-V curves (E/A ratio is 0.75 and total simulation time is 253 ps). **b**, Calculated I-V curves (E/A ratio is 2.79 and total simulation time is 253 ps). **c**, Calculated I-V curves (E/A ratio is 0.75 and total simulation time is 1 ns). **d**, Calculated I-V curves (E/A ratio is 0.75 and SEI thickness is 1.95 nm).

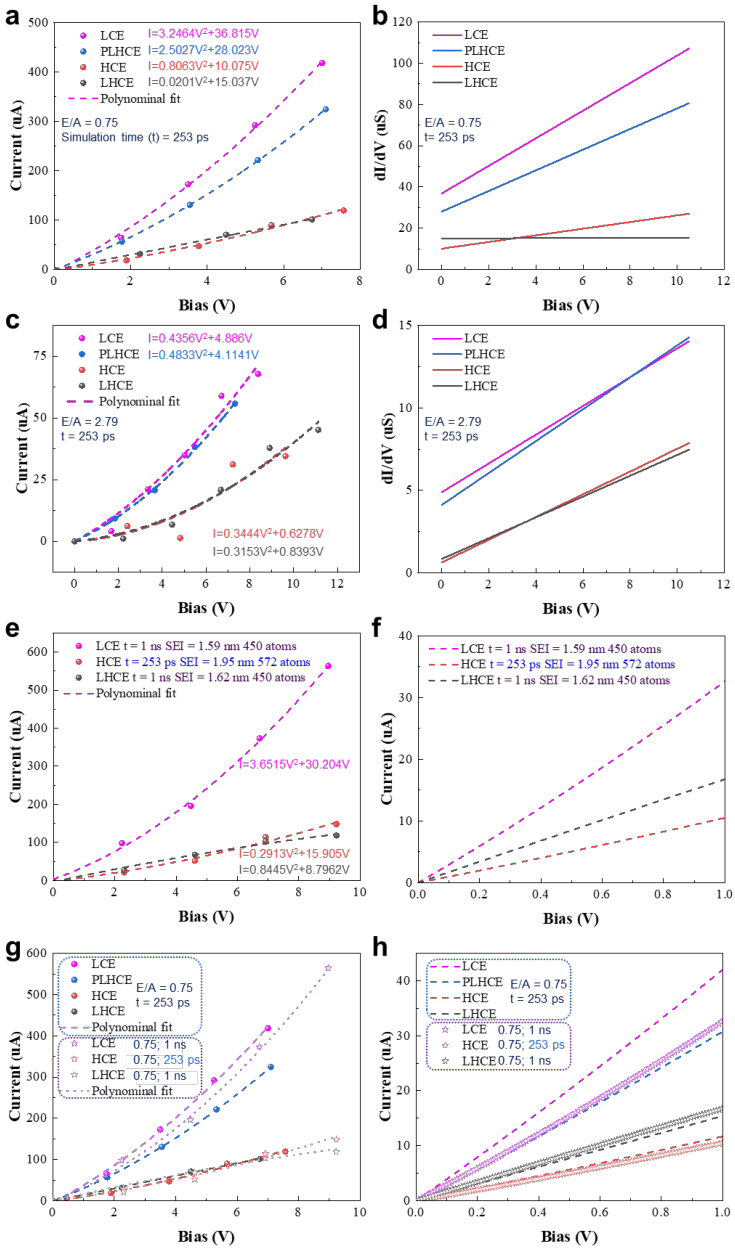

Supplementary Fig. 38 | Calcluated I-V curve and corresponding differential conductance. **a**, Calculated I-V curves (E/A ratio is 0.75 and total simulation time is 253 ps). **b**, Corresponding differential conductance, dI/dV as function of V, derived from the I-V curves. **c**, Calculated I-V curves (E/A ratio is 2.79 and total simulation time is 253 ps). **d**, Corresponding differential conductance. **e**, Calculated I-V curves with different simulation time and sample size. **f**, Corresponding low voltage range (0-1 V) I-V curve. **g**, Comparison of I-V curves with different simulation time and sample size. **h**, Low voltage range (0-1 V) I-V curve.

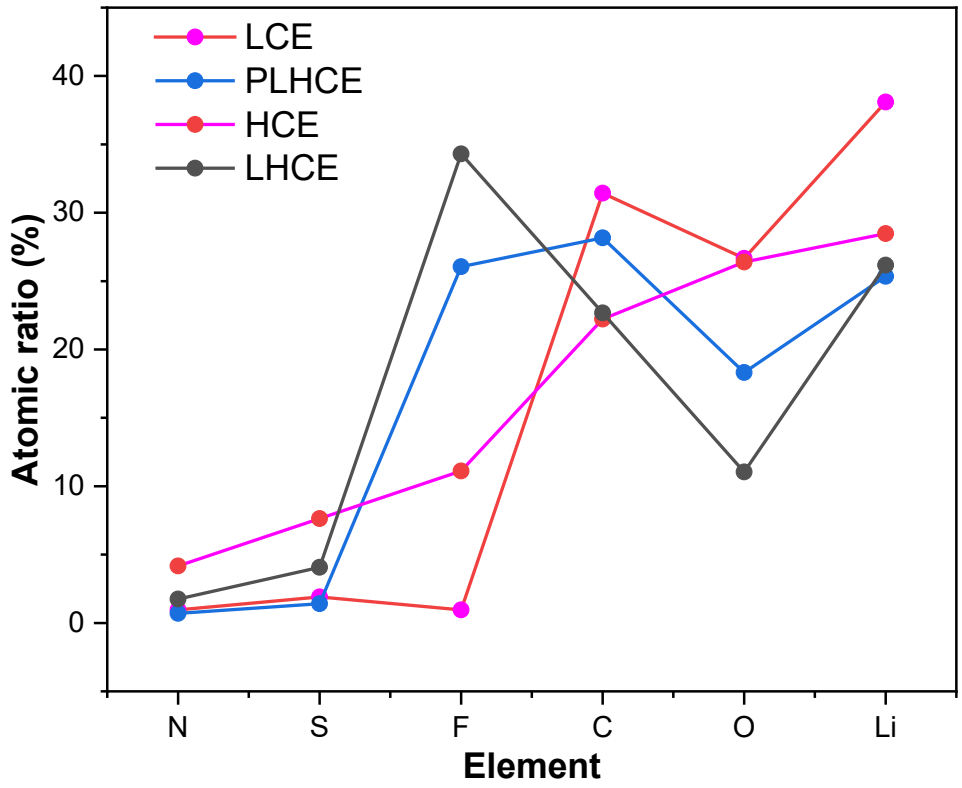

Supplementary Fig. 39 | Atomic ratios of different elements of SEI layer on Li deposits formed in the different electrolytes based on calculated sample cell.

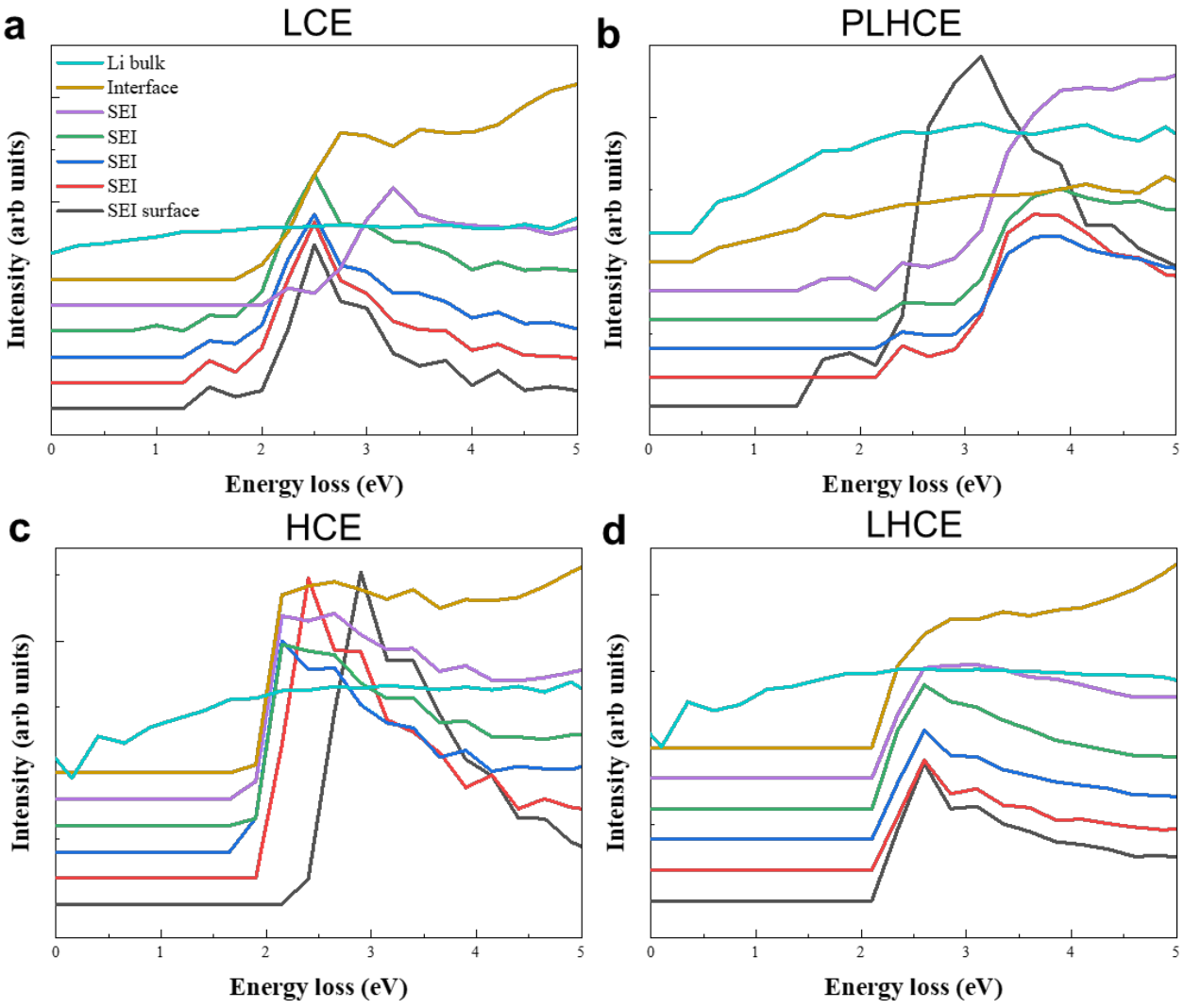

Supplementary Fig. 40 | The bandgap measurements of SEI on Li formed in the different electrolytes using STEM-EELS after background subtraction. Bandgap measurements from Li to SEI surface formed in **(a)** LCE, **(b)** PLHCE, **(c)** HCE, and **(d)** LHCE.

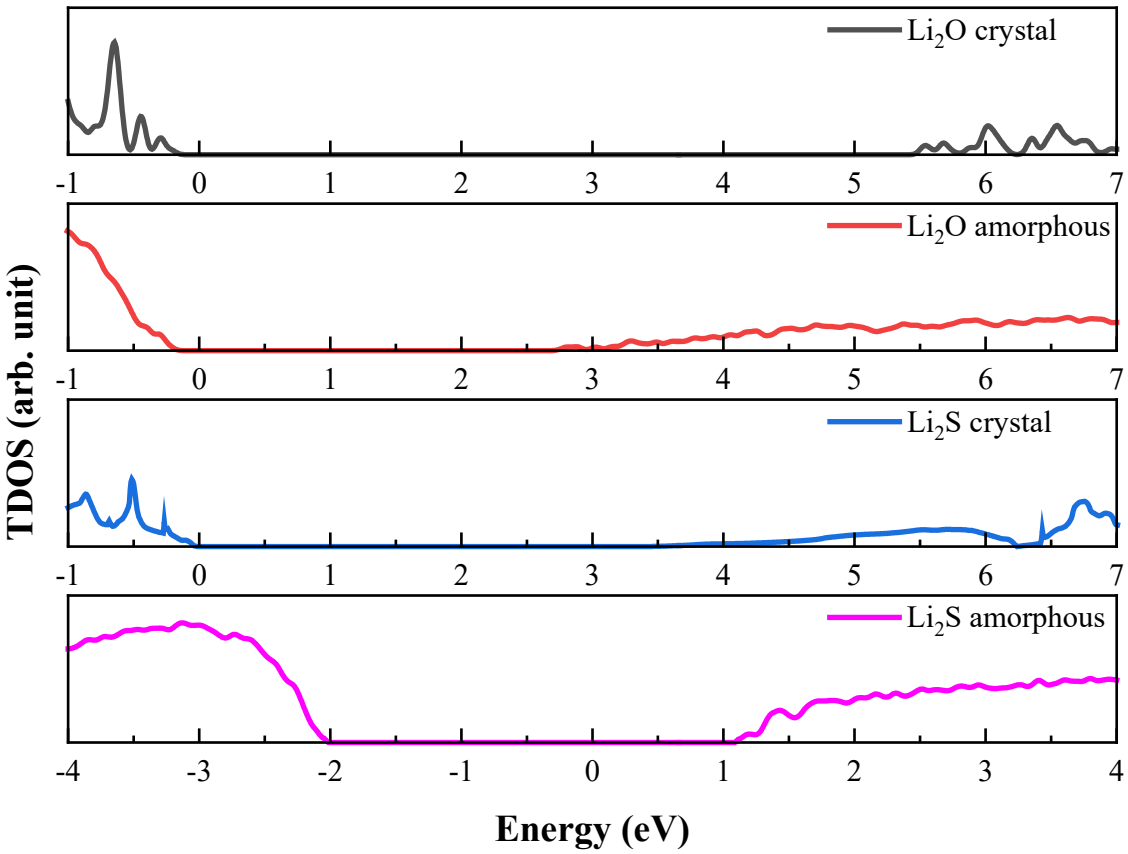

Supplementary Fig. 41 | Total density of states (TDOS) of Li_2O and Li_2S crystal, amorphous Li_2O and Li_2S.

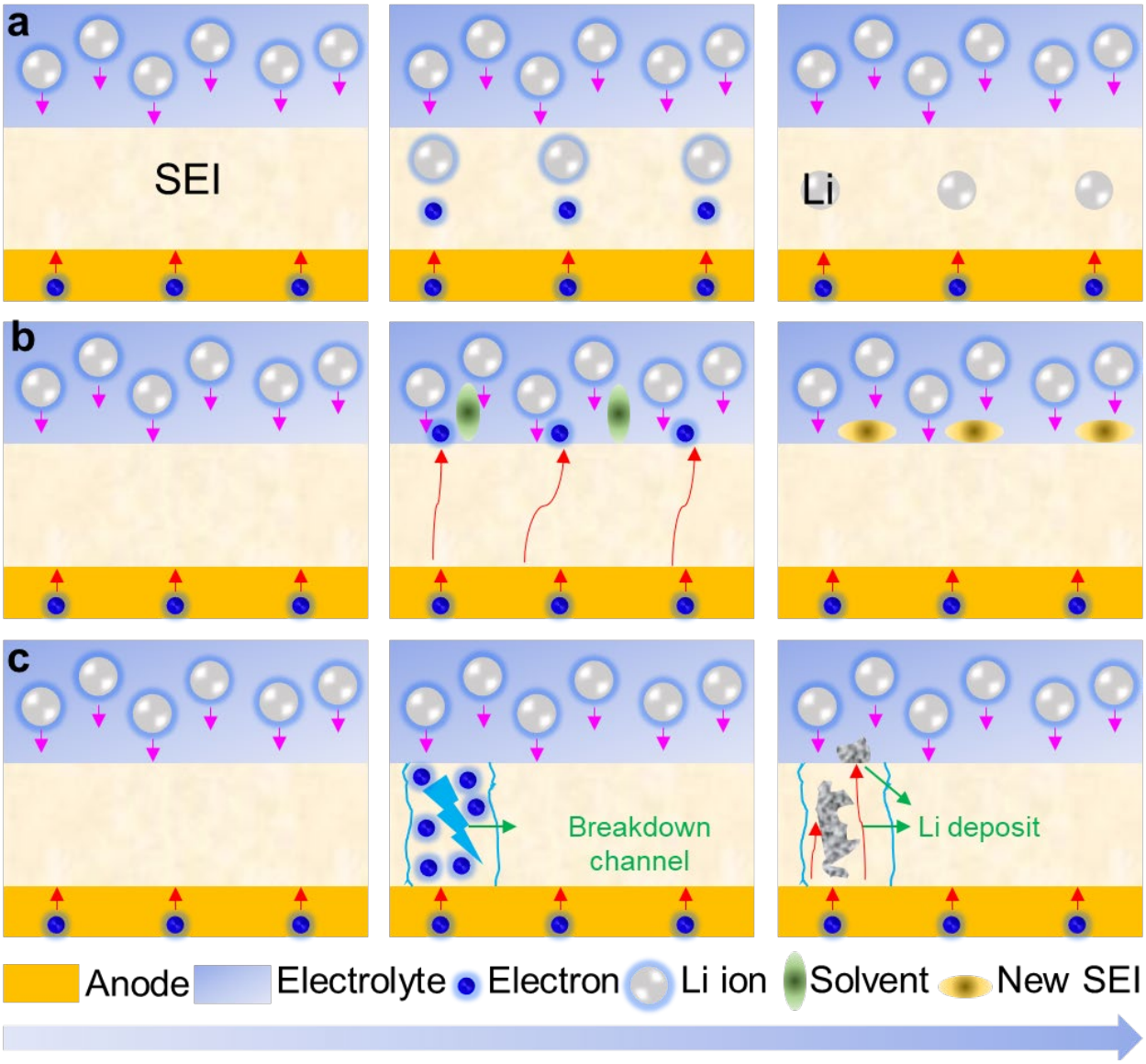

Supplementary Fig. 42 | Mechanisms of Li propagation inside SEI. a, High electronic conductivity of SEI induces the formation of dispersed metallic Li inside SEI. **b**, High electronic conductivity of SEI induces the reduction of solvent to form new SEI on the surface of original SEI. **c**, Unexpected high electric field inside cell induces channel in SEI which will facilitate formation of metallic Li both inside and at the surface of SEI.

Supplementary Methods

Preparation of copper (Cu) and tungsten (W) wires for in situ biasing transmission electron microscopy (TEM)

Cu wire for in situ biasing TEM experiment was directly cut by pincer plier from commercial Cu wire (diameter: 0.25 mm) and TEM half grid for cryogenic TEM (cryo-TEM) was directly cut by razor blade from Cu TEM grid in an argon (Ar)-filled glove box to minimize the oxidation and contamination of Cu. W wire was prepared by electrochemical etching. As shown in Supplementary Fig. 3, the surface of Cu and W is very clean.

TEM Cu foil preparation

Cu foil for TEM observation was directly prepared from commercial Cu foil which was used as the current collector in coin cells. The Cu foil is thinned by Ar ion milling using a Gatan precision ion polishing system (PIPS, Gatan, USA) to make an electron transparent area. After the preparation, the Cu TEM foil was transferred into an Ar-filled glovebox to avoid oxidation[1].

Cryo-transfer procedure

After deposition, the TEM Cu foil with SEI and the TEM grid with Li deposits were taken out from the coin cell and slightly rinsed with DME to remove trace electrolyte and Li salt in the glovebox. Then, the TEM Cu foil with SEI or TEM grid with Li deposits was placed in a sealed bag filled with Ar. The sealed bag was plunged directly into a bath of liquid nitrogen after taken from the Ar-filled glove box until the TEM Cu foil or TEM grid reached the very low temperature (around 100 K). Then the TEM Cu foil or TEM grid was quickly taken out from the sealed bag and loaded onto a pre-cooling Gatan cryo-holder (Elsa, Gatan, USA) using a cryo-transfer station to ensure the entire process occurred under cryogenic environment.

Cryo-TEM characterization of SEIs formed on Cu and Li

Cryo-TEM observations were performed on a 300 kV FEI Titan monochromated (scanning) transmission electron microscope ((S)TEM) equipped with a probe forming lens aberration corrector. The samples were viewed at low temperature (100 K) under low dose condition (~100 $e \cdot Å^{-2} \cdot s^{-1}$ for high-resolution TEM imaging). Energy dispersive X-ray spectroscopy (EDS) elemental mapping was collected by scanning the same region multiple times at a dwell time of 0.01 ms and electron probe current ~40 pA. Electron energy loss spectroscopy (EELS) was collected on a Gatan GIF-Quantum spectrometer. The EELS collection semi-angle during the spectroscopy experiments was ~45 mrad. EELS spectra dispersion was 0.05 eV per channel with vertical binning of 130. The probe beam current was around 25 pA, pixel dwell time as 0.01s. The

electron dose applied during the acquisition of the EELS spectra shown in the main text was 100 $e \cdot Å^{-2}$. All those electron dose rates do not introduce obvious damages after the acquisition of images, EDS and EELS spectra[2-4].

Electrochemical testing

The Li||Cu cells were assembled for the Li Coulombic efficiency (CE) determination using the CE testing protocol optimized in our previous work[5]. 5 mAh cm^{-2} Li was first deposited on Cu electrode and full stripped till 1 V to determine the initial Li CE. Another 5 mAh cm^{-2} Li was deposited on the Cu electrode followed by 10 times repeated stripping and depositing of 1 mAh cm^{-2} Li on Cu electrode and fully stripped the Li till 1 V at the end to get the average Li CE.

The Li||$LiNi_{0.8}Mn_{0.1}Co_{0.1}O_2$ (NMC811) cells were assembled and an Al-clad cathode case was used to avoid stainless steel corrosion at high voltages. Another Al foil with a diameter of 1.9 cm was placed between the cathode disk and the Al-clad case for further protection. The cells were charged/discharged in a voltage window of 2.8 to 4.4 V on Land battery testers (Wuhan Land) at 25 °C and at C/3 rate (a constant-voltage charge at 4.4 V was applied after the cell was charged to 4.4 V until the current reached C/20 or the time reached 1 h) after two formation cycles at C/10.

The performances of four electrolytes in LMBs are summarized in Supplementary Table 3.

X-ray photoelectron spectroscopy (XPS) analysis procedure

Physical Electronics Quantera Scanning X-ray Microprobe with a focused monochromatic Al Kα X-ray (1486.7 eV) source was employed for the XPS characterizations. The X-ray beam was incident normal to the sample, and the photoelectron detector was at 45° off normal. High energy resolution spectra were collected using a pass-energy of 69.0 eV with a step size of 0.125 eV. The X-ray beam diameter was ~100 μm and was scanned over a 1200 μm × 200 μm area of the sample.

Electrolyte solvation structure simulation

Ab initio molecular dynamics (AIMD) simulations were performed by Vienna Ab initio Simulation Package (VASP). Electron-ion interactions were described by the projector-augmented wave (PAW) pseudopotentials with the cutoff energy of 400 eV[6]. The exchange-correlation functional was represented using the Perdew-Burke-Ernzerhof generalized gradient approximation (GGA-PBE). The exchange-correlation functional with a Gaussian smearing width term of 0.05 eV was used. The convergence criterion for electronic self-consistent iteration was set to 1×10^{-5} eV. The simulations were performed in the canonical ensemble. The initial densities of these system (LCE, PLHCE, HCE, and LHCE) and molar ratios are obtained from experiment. The constant temperature of the AIMD simulation systems was controlled using the Nosé thermostat

method with a Nosé-mass parameter of 0.1 at 298 K. The initial structure of each system was set up by randomly placing the numbers of LiFSI, DME and/or diluent molecules based on experimental densities and molar ratios. These initial geometry structures were firstly optimized with classical molecular dynamics method using OPLS-AA force field[7]. Then the systems were preequilibrated for 5 ps by AIMD. Finally, product simulations of 10 ps were carried out with a time step of 1 fs. The projected density of states (PDOS) was calculated and averaged over 10 different configurations (extracted from MD simulation snapshots) to represent ensemble average of the PDOS. A Monkhorst-Pack k-point mesh grid scheme was used as 2 × 2 × 2.

TDOS calculation of amorphous and crystalline Li_2O and Li_2S

AIMD simulations were performed by VASP. Electron-ion interactions were described by the PAW pseudopotentials with the cutoff energy of 650 eV[6]. The exchange-correlation functional was represented using the GGA-PBE. The convergence criteria for the electronic and ionic steps were set to be the energy of 10^{-6} eV and the force of 0.01 eV $Å^{-1}$, respectively. The initial structure parameters of crystals were obtained from the work of Xu et al. [8]. The amorphous structures were obtained by quenching the systems after MD simulations at 1800 K. For the calculation of the total density of states (TDOS), the Monkhorst-Pack grids of 4 × 4 × 4 and 2 × 2 × 2 were used for crystal structures and amorphous structures, respectively.

Supplementary Note 1.

Calibration measurement

Electrode setup

In the experimental setup, the W is negative electrode, and Cu with SEI is positive electrode (Supplementary Fig. 4b). Initially, we connected Cu wire with SEI/Li deposit as negative and W electrode as positive (Supplementary Fig. 4a), and the measured I-V curve is shown as Supplementary Fig. 4c. There is no obvious difference when we exchange the position of W and Cu (Supplementary Fig. 4d). The small difference between Supplementary Figs. 4c-d is associated with the measurement error, which is partially associated with the small difference of work function between Cu (4.76 eV, average of different plane) and W (4.61 eV, average of different plane) [9], therefore generating an electrostatic potential difference, and consequently affecting the measured current value. The I-V curves we measured as shown in Figs. 3a-c and Supplementary Figs. 5-7 and 9-15 are all acquired based on experimental setup as shown in Supplementary Fig. 4b. As such, the effect of electrostatic potential difference between Cu and W will not affect the comparison of electrical properties of SEI formed in the different electrolyte.

Bias calibration

The I-V curve measurements are conducted by sweeping the voltage from 0 V to high voltage at a constant rate 0.125 V/0.25 ms. The reason why we only bias from zero volt toward positive direction is because we found that there is a critical voltage. When the bias is above the critical voltage, the SEI layer will break down, as represented by the fact that the current will reach to maximum of instrument limitation. For an unknown SEI layer, as we do not know the breakdown voltage, if we sweep from negative to positive voltage, we may unintentionally break down the SEI layer upon initial application of the large voltage that is above the breakdown voltage. Therefore, we always sweep the voltage from zero towards positive direction for each measurement.

Further, we indeed carried out sweep the potential from negative to positive voltage as shown in Supplementary Fig. 5. If the voltage is below the critical voltage, the I-V curve is symmetric between negative and positive voltage range. We even can run two cycles as shown in Supplementary Fig. 5b.

In order to accurately measure electrical transport in SEI on Cu and Li by this method, we measured the current (I)-voltage (V) curves under different conditions to prove it works. As shown in Supplementary Fig. 6a, we firstly acquired the I-V curve with W tip and Cu TEM wire uncontacted with each other, which could get background noise from the experiment setup, and the background current is nearly irrelevant to the applied bias.

The applied bias range and electron beam effect on measured electrical conductance were also explored as shown in Supplementary Figs. 6b-d and summarized in Supplementary Fig. 6e. When Cu TEM wire was prepared in the air with a surface layer (Supplementary Fig. 6f), the I-V curve shows a linear relationship, suggesting that the transport and this contact are Ohmic due to the surface contamination layer (Supplementary Fig. 6g). While when W tip and Cu TEM wire without SEI formed on contact with each other, it will make the current reach the maximum value no matter how large bias was applied (Supplementary Fig. 6j). This short circuit phenomenon also proved that the W tip and Cu TEM wire that we prepared in the glove box have clean surface.

In addition, the constant voltage was also applied to get I-t (time) curve, when the constant voltage is above critical voltage (Supplementary Fig. 7a), the current value is maximum value of instrument, indicating this irreversible transition from semiconductor to conductor. While the constant voltage is below critical voltage (Supplementary Fig. 7b), the current value is constant and similar with applied voltage range (Supplementary Fig. 8a), which also confirms that the measured current value is from electron other than Li ion transport.

Supplementary Note 2.

Calibration of sample size, bias range and electron beam effect during the in situ measurement

The sample size, bias range, and electron beam effect were explored in reference samples and SEI layers. Supplementary Fig. 8 shows the in situ probing electrical response measurements of different sample sizes of SiO_2 and TiO_2. The I-V curves, corresponding dI/dV-V curves and calculated electrical conductance of SiO_2 (Supplementary Fig. 9) show that the bias range, sample size and electron beam do not affect electrical properties. The bias range, the sample size and electron beam will affect the current value and dI/dV of TiO_2 as shown in Supplementary Fig. 10, smaller sample size has lower current value, larger bias range will increase current value and dI/dV, and electron beam will also largely increase the current value and dI/dV, which is similar with SEI on Cu and Li (Supplementary Figs. 11-12).

We measured the I-V curves at low voltage range (0-1.0 V) and amplified the voltage range of 0-0.5 V as shown in Supplementary Fig. 13. We used Boltzmann nonlinear fitting method to fit the low voltage range I-V curves. It should be noticed that the exact voltage applied on SEI should be smaller than I-V curve, as there are some contact voltage drops from experimental setup. The I-V curves on Li in low voltage range is similar to that in high voltage range.

Supplementary Note 3.

Statistics analysis of measured I-V curve

As the I-V curve is acquired following on the real battery cell cycling, therefore, to make sure the data repeatability, we measured I-V curve 10 times at different regions of each SEI layer formed in one Cu wire, which shows the similar results as shown in Supplementary Fig. 14. Even from same region, when apply bias below critical voltage, the I-V curves acquired from two times have very good consistent as shown in Supplementary Fig. 5b.

Supplementary Note 4.

Consideration of SEI thickness effect on the measured I-V curve

Based on our experimental setup, two ion-blocking Cu/W electrodes were used. We have drawn the I-V curve and the electrical differential conductance, dI/dV, against the applied voltage, V, where I is the current as shown in Supplementary Fig. 15(a) and (b). However, the thickness of SEI layer, L, for different electrolyte is different. The thickness of SEI, L, could be directly obtained by cryogenic TEM (Fig. 5a). To account for the SEI layer thickness effect, we draw the electrical differential conductance, dI/dV, as a function of the electrical field strength, E, as E = V/L, by which the SEI layer thickness effect is normalized. As shown in Supplementary Fig. 15 (c), the electrical differential conductance, dI/dV, against the electrical field strength, E, shows similar trend of variation for the case of dI/dV as a function of V (Supplementary Fig. 15b).

Supplementary Note 5.

Fine structure and chemical composition of SEI layers on Cu and Li

The fine structure and composition of SEI layers formed on the Cu and Li were characterized by cryo-TEM, EDS, EELS and XPS.

Cryo-TEM

The SEIs formed in different electrolytes show different fine structural features (Supplementary Figs. 16-19). The SEI on Li deposit formed in LCE has a bilayer structure with rough surface, featuring an amorphous outer layer of ~ 15 nm and a mosaic inner layer of ~ 20 nm with crystalline Li_2O particles dispersed in an amorphous matrix (Supplementary Fig. 19). In addition, a few Li_2O particles are observed to be trapped in Li deposit. The SEI formed in PLHCE exhibits a mosaic structure with a thickness of ~ 25 nm (Fig. 5a). The interface between the Li deposit and the SEI is not sharp, and there are few Li_2O nanoparticles embedded in the Li deposit. The SEI formed in HCE exhibits a thickness of ~15 nm and with the sparse dispersion of Li_2O particles in the amorphous matrix. The SEI formed in LHCE is remarkably different from those formed in the

other three electrolytes. First, the thickness of the SEI layer on Li is very thin, only ~ 7.5 nm, which is identical to that of the SEI on Cu (Supplementary Fig. 18h). Second, the SEI on the Li deposit is continuous and uniform. Third, the SEI exhibits a fully amorphous structure.

STEM-EDS

The SEIs formed in different electrolytes also show different elemental distribution (Supplementary Figs. 20-23). As shown in Supplementary Fig. 2a, the SEI layer on Cu formed in LCE is mainly comprised of O (72.6 at.%), and very few S, C, N and F, and changes a little on Li (Supplementary Fig. 22b). The extremely low concentration of C in LCE implies that this SEI layer is not rich in organic species. This is also validated by the projected density of state analysis (PDOS) analysis in AIMD simulation as the lowest unoccupied molecular orbital (LUMO) energy is not located on solvent.

When the BFTEC diluent was added to HCE, the chemical composition of the SEI layer changed a lot (Supplementary Fig. 22a). The SEI layer on Cu is mainly composed of O (57.2 at.%) and S (21.2 at.%), and few C (11.7 at.%), and that on Li is majorly composed of O (69.4 at.%) and S (9 at.%), and few C (14.4 at.%), indicating more organic solvent involved SEI formation. In other words, there is the most severe solvent/diluent decomposition in this electrolyte, which could be strongly related to the pseudo-LHCE nature (PLHCE). Thus, the favorable features of HCE are lost in PLHCE. This is also consistent with previous simulation results: BTFEC prefers to coordinate with Li^+ in a second solvation shell beyond the first solvation with DME and FSI^-, which partially damages the high-concentration coordinated clusters in the HCE by forming a PLHCE[10].

While in the HCE, the SEI layer on Cu is rich in S (37.8 at.%) and O (34.8 at.%), few F, C, and very few N, and the SEI on Li is rich in O (44.6 at.%) and S (28.3 at.%), which indicate high levels of O-, S-, and F-containing species derived from LiFSI salt, and few from C-containing organic solvent. This is also supported by the PDOS analysis in the AIMD simulation since the LUMO energy is located on FSI- anion. The decomposition of FSI- anion will generate the high contents of S and O.

In comparison to other three electrolytes, adding BTFE diluent induces more S-containing species formed in the SEI layer as shown in Supplementary Fig. 22, implying that the FSI^- anions are predominantly reduced. Especially, the higher S/O ratio indicates S=O bond of FSI^- is difficult to break as shown in Supplementary Fig. 23. The high S/O ratio also indicates the FSI is deeply reduced in LHCE. The distinct morphologies of Li deposits and distinct chemical information of SEI layers formed in the four electrolytes indicate the strong correlation between solvation structure and SEI layer.

STEM-EELS

EELS can yield elemental distribution with high spatial resolution and be sensitive to Li. Supplementary Fig. 24 illustrates the EELS elemental maps, showing the spatial distribution of elements in SEI layers formed in the different electrolytes. As shown in Supplementary Fig. 24b, O and Li are distributed uniformly across the SEI layer formed in LCE, while C within the SEI layer shows the non-uniform distribution. In HCE, O and Li distributions are not uniform across the SEI layer and O has a higher concentration in the inner layer of the SEI, while Li has a high concentration in the outer layer of the SEI, and C and F only distribute in the outer layer of the SEI.

For PLHCE, Li, O and C are distributed uniformly across the SEI layer. This is because besides organic fragments, the decomposition of BTFEC could generate CO_3^{2-}, which will form Li_2CO_3 with Li. On the contrary, for the LHCE, Li and S within the SEI show distinguished bilayer, featuring that the inner layer has lower Li intensity and higher S intensity, while O distributes near the Li deposit, and very few C distributes on the surface of SEI layer. The difference in the spatial distribution of different elements across the SEI layer indicates the difference in the SEI formation process in the different electrolytes, thus affects the electrical properties of SEI layers on the Cu and Li, and then regulate the Li morphology and finally affect the electrochemical performance of cells.

In addition, Li-K, S-L, O-K, C-K, N-K, and F-K spectra in the SEI layers were extracted from corresponding EELS elemental maps across Li metal to the surface of the SEI layer (Supplementary Figs. 25-26). For example, the S L-edge spectra only show high intensity near the surface of the SEI layer formed in the HCE and LHCE, which indicates the possible presence of Li_2S, SO_2F, and SO_x. The O K-edge spectra of SEI layers in LCE and PLHCE show high intensity around 535 eV, 540 eV, and 555 eV as shown in Supplementary Figs. 25c and 25f, indicating a high content of Li_2O as well[3,4,11]. The low intensity of C K-edge of SEI layers formed in the HCE and LHCE is consistent with the EDS results, which confirms the main components of SEI are from the FSI^- anions rather than solvent in those two electrolytes. In addition, high intensity of F K-edge only appears near the surface of the SEI layer formed on the HCE, which is consistent with EDS results (Supplementary Fig. 21) as well.

XPS

XPS spectra of selected elements of the SEIs formed in the studied electrolytes are illustrated in Supplementary Figs. 27-28. All the XPS spectra were calibrated by shifting the C-C peak in the C 1s spectra to the binding energy of 284.8 eV. It should be noted that the XPS spectra results are consistent with EDS and EELS results except C 1s spectra, indicating few C-containing species might form as indirect SEI layer on Li, rather than compact SEI layer on Li surface[12].

Supplementary Note 6.

Discussion of solvation structure of electrolyte

As FSI^- anion is the only source of S in electrolytes we studied here, the experimentally observed systematic change of O:S ratio in the SEI layer indicates variation of solvent and salt anion FSI^- on the formation of SEI layer in different electrolytes. The AIMD simulations were performed to investigate the solvation structures at molecular level of the four electrolytes. The molecular structures and snapshots of the electrolytes from AIMD simulations are shown in Supplementary Fig. 29. In LCE, all the Li ions are solvated by DME solvent molecules. While in other three electrolytes, the contact ion pairs are observed due to the scarcity of solvating solvent (i.e. DME). In the radial distribution function plots obtained by AIMD simulations, the peaks for the correlations between Li ions and the O atoms in FSI^- anions are distinctive for HCE, PLHCE, and LHCE (Supplementary Fig. 30). The projected density of state (PDOS) analysis was employed to investigate the decomposition of solvent/diluent. As shown in Supplementary Fig. 31, the solvation structure of Li ion in PLHCE is changed because the BTFEC can insert into the solvation sheath of Li ion (Supplementary Fig. 31b). The lowest unoccupied molecular orbital (LUMO) energy is located on the BTFEC molecules, indicating the BTFEC molecules are preferentially reduced, which is consistent with the EDS and EELS results of the SEI from PLHCE showing the low S ratio in SEI (Supplementary Figs. 21-22 and 24). While for other electrolytes, the LUMO energies are all located on FSI^- anions. The PDOS analysis results are consistent with the experimentally observed tendency of O:S ratios in SEIs for different electrolytes. The spatial distributions of O and S are overlapped (Supplementary Fig. 24), indicating O=S is likely the dominant configuration as it is hard to break down the O=S in FSI^-.

Supplementary Note 7.

Methodology on SEI layer simulation and subsequently I-V curve calculation

SEI layer simulation

The lithium metal is a thirteen-layer slab cut along the Li (001) plane[13,14]. The cell dimensions are 13.78 Å x 13.78 Å x 39.21 Å. Periodic boundary conditions apply along the x- and y-coordinates while a fixed He-atom layer breaks periodicity along the z-coordinate. The lithium slab is 22.4 Å in thickness, and the electrolyte fills the vacuum space, such as the electrolyte-to-anode (E/A) ratio along the z-coordinate is 0.75 (Fig. 2a).

The SEI structures reported in this work were obtained using a hybrid AIMD/classical molecular dynamics (CMD) procedure as described in the Simulation part in main text of Methods section (Fig. 2b). A finite cluster sample of the box of dimensions 13.78 × 13.78 × 16.5 Å was used to generate the wavefunctions for the SEI for the GENIP procedure. This finite sample was taken from an AIMD/CMD simulation that generated a SEI periodic simulation box of dimensions 13.78 × 13.78 × 39.21 Å. To account for the effects external metallic contacts embracing the SEI finite

layer, partial densities of states of gold electron reservoirs were provided to the GENIP program to use them for all analyzed SEIs, thus fair comparisons can be made among the four studied SEIs.

We could change the E/A ratio to alter modeling structure size. Hence, we performed three rounds of simulation with different length and time scale. The sample cells in I-V curve calculations are based on the hybrid AIMD combined with reactive force field simulations (Fig. 2c). The first-round we built electrolyte (E) /Li metal (A) with E/A ratio as 0.75, and total simulation time was 253 ps (Supplementary Figs. 32a-d). In this case, the SEI samples used for the I-V curve calculations are around ~15 Å in thickness, depending on the electrolyte: LCE = 15.0 Å, PLHCE = 16.0 Å, HCE = 15.0 Å and LHCE = 15.8 Å (Supplementary Figs. 32e-h). In the second-round simulation, we increased E/A ratio to 2.79, and kept the same simulation time (Supplementary Figs. 34a-d). The thicknesses of the SEI samples used in the I-V curve calculations are LCE = 14.2 Å, PLHCE = 16.5 Å, HCE = 16.8 Å and LHCE = 15.5 Å (Supplementary Figs. 34e-h). In the third-round simulation, we chose three electrolytes: LCE and LHCE with longer simulation time (total time is 1 ns), and HCE with larger sample surface size (Supplementary Figs. 36 a-c). In this case, the thicknesses of SEI samples used in the I-V curve calculations are LCE = 15.9 Å, HCE = 19.5 Å and LHCE = 16.2 Å (Supplementary Figs. 36 d-f). The simulation parameters are summarized in Supplementary Table 4, calculated I-V curves and corresponding differential conductance are summarized in Supplementary Figs. 37-38. The number of molecules approximates the molar ratios in Supplementary Table 2 within the limitations due to the cell sizes.

I-V curve calculation

A combined density functional theory and Green's function approach (DFT-GF) is used to study the electron transport through molecular-solid systems consisting of a non-stoichiometric SEI finite cluster sample, bounded by two bulk electrodes represented by two metallic nanocontacts, following the experiments carried out in this work to obtain the I-V characteristics (Fig. 2c). We use our program GENIP[15-17] (Generalized Electron Nano-Interface Program) developed by our nanoelectronics group. An external voltage is applied to the two metal nanocontacts, thus recreating not only the usual current through a molecular system but also the quantum mechanical effects such as the tunneling current that would occur during I-V experimental measurements. These leakage currents are those producing the reduction of the electrolyte components, even of the counter-ions at electrolyte-electrode interfaces, and thus formation of the SEI. The GENIP procedure has been largely validated and described in several previous studies to obtain I-V characteristics[18-24]. It uses as inputs the wavefunctions from two DFT calculations, one for the bulk electrode using periodic boundary conditions with the program Crystal-06[25] and the other for the SEI finite cluster sample obtained using the program Gaussian 16[26].

We performed single point self-consistent field (SCF) calculations to the SEI cluster (known as the molecule), which was extended with one metallic atom at each end, where the external voltage is applied, using the B3PW91[27,28] hybrid functional with the 6-31G(d) basis set[29] for C, H, O, F,

S, N, and Li, and the basis set LANL2DZ[30] for the metal as they are implemented in the Gaussian-16 program. Hamiltonian and overlap matrices are obtained self-consistently for every external field applied to the extended cluster sample. Thus, every point of the I-V curve corresponds to a separated DFT calculation under the corresponding electric fields. The metal bulk electrodes partial DOS was calculated using the Crystal-06 program. Specifically, the GENIP[25] program takes as input, for each bias voltage of the Hamiltonian, the density and the overlap matrices and the calculated bulk DOS to obtain electron transport characteristics considering the local nature of the SEI cluster sample as well as the nonlocal features of the bulk electrodes. In this procedure, the self-consistent treatment performed when the external electric field is applied to the extended SEI finite cluster sample ensures that the chemistry of the SEI is not lost throughout the calculations of geometry optimizations as it corresponds to a strong nonequilibrium system.

The calculated I-V curves with different E/A ratio and simulation time are shown in Supplementary Fig. 37, and corresponding differential conductance curves are summarized in Supplementary Fig. 38. There are not too many differences between results from shorter time and longer time simulations (Supplementary Fig. 37c), smaller E/A ratio and larger E/A ratio simulations (Supplementary Figs. 37a-b), and thinner SEI and thicker SEI simulations (Supplementary Fig. 37d), indicating a well equilibrated, representative system.

Supplementary Tables

Supplementary Table 1 | Physical properties of the investigated solvents.

Solvent	DME	BTFEC	BTFE
Molecular weight/g mol^{-1}	90.12	226.07	182.06
HOMO/eV	-7.19[10]	-9.28[10]	-8.76[10]
LUMO/eV	-0.18[10]	-0.6[10]	-0.5[10]
Viscosity at 25 °C/cP	0.122	1.69[10]	0.7[10]
Density/g mL^{-1}	0.868[31]	1.51[10]	1.4[10]
Boiling point/°C	85	117-118	62-63
Flash point/°C	-41	N/A	1
Fluorine:hydrogen ratio	N/A	1.5	1.5

Supplementary Table 2 | Physical properties of the investigated electrolytes.

Electrolyte	LCE	PLHCE	HCE	LHCE
Density/g mL^{-1}	0.966[31]	1.45[10]	1.41[32]	1.39[10]
Conductivity at 25 °C/mS cm^{-1}	16.9[33]/21.9[31]	2.64[10]	4.18[34]	4.88[10]
Viscosity at 25 °C/cP	0.58[31]/1.61[32]	4.06[10]	77.71[32]	2.86[10]
Salt concentration/M	1	1.49	4.4	1.65

Note:
LCE: LiFSI-9DME (by mol.)
HCE: LiFSI-1.2DME (by mol.)
PLHCE: LiFSI-1.2DME-3BTFEC (by mol.)
LHCE: LiFSI-1.2DME-3BTFE (by mol.)

Supplementary Table 3 | Summary of the performances of four electrolytes in LMBs.

Electrolyte	Anode	Initial CE (Li||Cu)	Average CE (Li||Cu)	Initial CE (Li||NMC811)	Average CE (Li||NMC811)	Cycling performance
LCE	Li	90.3%	98.1%	83.34%	96.68%	After 10 cycles dropped to 80% initial capacity
PLHCE	Li	98.3%	96.8%	85.96%	96.81%	After 41 cycles dropped to 80% initial capacity retention
HCE	Li	98.6%	98.6%	87.99%	99.15%	80% initial capacity retention after 57 cycles
LHCE	Li	99.2%	99.2%	87.88%	99.36%	80% initial capacity retention after 110 cycles

Supplementary Table 4 | SEI simulation and I-V curve calculation parameters.

Electrolyte	Label	Molarity	# Molecules	Density [g/cm^3]	Li thickness (Å)	Electrolyte thickness (Å)	E/A ratio	SEI sample thickness (Å)	Total simulation time
LiFSI:DME	LCE	1	2:14	0.966	22.4	16.8	0.75	15.0	253 ps
					10.33	28.9	2.79	14.2	253 ps
					22.4	16.8	0.75	15.9	1 ns
LiFSI:DME/BTFEC	PLHCE	1.49	2:3:7	1.45	22.4	16.8	0.75	16.0	253 ps
					10.33	28.9	2.79	16.5	253 ps
LiFSI:DME	HCE	4.4	8:9	1.41	22.4	16.8	0.75	15.0	253 ps
					10.33	28.9	2.79	16.8	253 ps
					22.4	16.8	0.75	19.5*	253 ps
LiFSI:DME/BTFE	LHCE	1.65	3:3:8	1.39	22.4	16.8	0.75	15.8	253 ps
					10.33	28.9	2.79	15.5	253 ps
					22.4	16.8	0.75	16.2	1 ns

* This is the biggest cell, contains 552 atoms. All other cells contain ~450 atoms.

Supplementary Table 5 | Simulated SEI composition from full cell. The E/A ratio is 0.75.

(at.%)	LCE	PLHCE	HCE	LHCE
Li-O-C	24.91	20.6	12.28	8.13
Li_2O	15.97	11.48	5.63	2.27
SO_xLi	4.72	2.44		
SO_2F	0.27	0.34	1.4	0.68
LiF	0.44	1.01	12.52	17.18
SO_x		5.96	13.63	18.47
NSO_xF_y	0.08	0.06	0.46	0.52
S=O	6.14	4.8	2.92	2.69
S-F	0.06	0.19	1.33	0.8
N-$(SO_x)_2$	0.08	0.05	0.38	
Inorganic	**54.46**	**59.77**	**67.21**	**72.78**
C-C/C-H	12.92	20.78	4.67	2.53
C-O	32.62	20.45	28.12	24.72
Organic	**45.54**	**40.23**	**32.79**	**23.61**

Supplementary Table 6 | Simulated SEI composition from sample cell. The E/A ratio is 0.75.

(at.%)	LCE	PLHCE	HCE	LHCE
Li-O-C	7.79	8.11	5.94	5.67
Li_2O	7.79	10.81	25.74	8.51
Li_2S	6.49		11.88	3.55
LiF	5.19	40.54	12.87	39.72
N-S	1.3		0.99	
C=C	3.9	5.41	1.98	6.38
LiN_x	12.99		12.87	4.96
CF_3		0.68		1.42
CO_3^{2-}		0.68		
Inorganic	**45.46**	**66.22**	**72.28**	**70.21**
C-C/C-H	38.96	24.32	19.8	21.99
C-O	15.58	9.46	7.92	7.8
Organic	**54.54**	**33.78**	**27.72**	**29.79**

Supplementary Table 7 | Simulated SEI composition from full cell. The E/A ratio is 2.79.

(at.%)	LCE	PLHCE	HCE	LHCE
Li-O-C	12.23	8.89	9.22	3.75
Li_2O	17.47	9.7	16.5	13.75
Li_2S	3.06	1.62	0.49	0.31
LiF	3.93	34.5	15.53	43.44
N-S	0.44			
SO_xLi		0.54	3.88	
SO_x		1.35	8.25	
NSO_xF_y			1.46	
S=O		0.27	1.21	
$N-(SO_x)_2$		0.27	0.97	
C=C	6.11	1.89		5
LiN_x	2.18	1.08	3.88	5
CF_3		1.08		2.81
O-F			1.21	
O-F/C=O		7.28		0.31
CO_3^{2-}		0.54		
Inorganic	**45.42**	**69.01**	**62.6**	**74.37**
C-C/C-H	11.79	10.24	20.87	12.19
C-O	42.79	20.75	16.5	13.44
Organic	**54.58**	**30.99**	**37.37**	**25.63**

Supplementary Table 8 | Simulated SEI composition from sample cell. The E/A ratio is 2.79.

(at.%)	LCE	PLHCE	HCE	LHCE
Li-O-C	11.43	4.96	5.15	4.73
Li_2O	22.86	12.4	25	18.34
Li_2S	4.76	0.83	2.74	2.96
LiF	0.95	47.11	10.02	33.14
N-S	0.95			
SO_xLi		0.83	2.94	
SO_x		0.83	14.71	
NSO_xF_y			1.47	
S=O		0.83	1.47	
$N-(SO_x)_2$				
C=C	2.86	2.48	1.47	2.37
LiN_x	0.96	0.83	5.15	4.73
CF_3		0.83		2.37
O-F				
O-F/C=O			1.47	
CO_3^{2-}		0.8		
Inorganic	**44.77**	**72.73**	**71.59**	**68.64**
C-C/C-H	13.33	15.7	5.88	19.53
C-O	41.9	11.57	22.53	11.83
Organic	**55.23**	**27.27**	**28.41**	**31.36**

Supplementary Table 9 | XPS quantification of SEI components on Li.

(at.%)	LCE	PLHCE	HCE	LHCE
Li-O-C	24.91	20.6	12.28	8.13
Li_2O	15.97	14.23	5.63	2.27
Li_2S			12.76	17.62
SO_xLi	4.72	2.44		
SO_2F	0.27	0.34	2.18	1.28
LiF	0.44	1.01	12.52	17.18
SO_x		5.96	13.63	18.47
NSO_xF_y	0.08	0.06	3.03	0.6
S=O	6.14	5.48	3.48	3.34
S-F	0.06	0.19	1.32	1.01
$N-(SO_x)_2$	0.08	0.05	0.38	
C=C		3.07		2.85
Inorganic	**52.67**	**53.43**	**67.21**	**72.75**
C-C/C-H	14.71	20.96	4.67	2.53
C-O	32.62	20.45	28.12	24.72
Organic	**47.33**	**46.57**	**32.79**	**27.25**

Supplementary References

1 Xu, Y. B. *et al.* Sweeping potential regulated structural and chemical eCtion of solid-electrolyte interphase on Cu and Li as revealed by cryo-TEM. *Nano Energy* **76**, 105040 (2020).

2 Li, Y. Z. *et al.* Atomic structure of sensitive battery materials and Interfaces revealed by cryo-electron microscopy. *Science* **358**, 506-510 (2017).

3 Zachman, M. J., Tu, Z., Choudhury, S., Archer, L. A. & Kourkoutis, L. F. Cryo-STEM mapping of solid-liquid interfaces and dendrites in lithium-metal batteries. *Nature* **560**, 345-349 (2018).

4 Xu, Y. *et al.* Atomic to nanoscale origin of vinylene carbonate enhanced cycling stability of lithium metal anode revealed by cryo-transmission electron microscopy. *Nano Lett.* **20**, 418-425, (2020).

5 Adams, B. D., Zheng, J. M., Ren, X. D., Xu, W. & Zhang, J. G. Accurate determination of coulombic efficiency for lithium metal anodes and lithium metal batteries. *Adv. Energy Mater.* **8**, 1702097 (2018).

6 Kresse, G. & Joubert, D. From ultrasoft pseudopotentials to the projector augmented-wave method. *Phys. Rev. B* **59**, 1758-1775 (1999).

7 Jorgensen, W. L., Maxwell, D. S. & TiradoRives, J. Development and testing of the OPLS all-atom force field on conformational energetics and properties of organic liquids. *J. Am. Chem. Soc.* **118**, 11225-11236 (1996).

8 Xu, J. G. *et al.* Mechanical and electronic stabilization of solid electrolyte interphase with sulfite additive for lithium metal batteries. *J. Electrochem. Soc.* **166**, A3201-A3206 (2019).

9 Haynes, W. M. *CRC Handbook of Chemistry and Physics*. (CRC Press, Taylor & Francis Group, 2014).

10 Cao, X. *et al.* Effects of fluorinated solvents on electrolyte solvation structures and electrode/electrolyte interphases for lithium metal batteries. *Proc. Natl. Acad. Sci. U.S.A.* **118** e2020357118 (2021).

11 Xu, Y. *et al.* Current density regulated atomic to nanoscale process on Li deposition and solid electrolyte interphase revealed by cryogenic transmission electron microscopy. *ACS Nano* **14**, 8766-8775 (2020).

12 Huang, W., Wang, H., Boyle, D. T., Li, Y. & Cui, Y. Resolving nanoscopic and mesoscopic heterogeneity of fluorinated species in battery solid-electrolyte interphases by cryogenic electron microscopy. *ACS Energy Lett.* **5**, 1128-1135 (2020).

13 Doll, K., Harrison, N. M. & Saunders, V. R. A density functional study of lithium bulk and surfaces. *J. Phys.:Condens. Matter* **11**, 5007-5019 (1999).

14 Camacho-Forero, L. E., Smith, T. W., Bertolini, S. & Balbuena, P. B. Reactivity at the lithium-metal anode surface of lithium-sulfur batteries. *J. Phys. Chem. C* **119**, 26828-26839 (2015).

15 Derosa, P. A. & Seminario, J. M. Electron transport through single molecules: scattering treatment using density functional and green function theories. *J. Phys. Chem. B* **105**, 471-481 (2001).

16 Yan, L. M. & Seminario, J. M. Electronic structure and electron transport characteristics of a cobalt complex. *J. Phys. Chem. A* **109**, 6628-6633 (2005).

17 Sotelo, J. C., Yan, L. M., Wang, M. & Seminario, J. M. Field-induced conformational changes in bimetallic oligoaniline junctions. *Phys. Rev. A* **75**, 022511 (2007).

18 Seminario, J. M. & Yan, L. M. Ab initio analysis of electron currents in thioalkanes. *Int. J. Quantum Chem.* **102**, 711-723 (2005).
19 Bautista, E. J., Yan, L. M. & Seminario, J. M. Ab initio analysis of electron transport in oligoglycines. *J. Phys. Chem. C* **111**, 14552-14559 (2007).
20 Yan, L. M., Bautista, E. J. & Seminario, J. M. Ab initio analysis of electron currents through benzene, naphthalene, and anthracene nanojunctions. *Nanotechnology* **18**, 485701 (2007).
21 Hong, S. M. *et al.* Impedance measurements on a DNA junction. *J. Chem. Phys.* **128**, 201103 (2008).
22 Salazar, P. F. & Seminario, J. M. Identifying receptor-ligand interactions through an ab initio approach. *J. Phys. Chem. B* **112**, 1290-1292 (2008).
23 Wang, K. *et al.* Switchable molecular conductivity. *J. Am. Chem. Soc.* **131**, 10447-10451 (2009).
24 Benitez, L. & Seminario, J. M. Electron transport and electrolyte reduction in the solid-electrolyte interphase of rechargeable lithium ion batteries with silicon anodes. *J. Phys. Chem. C* **120**, 17978-17988 (2016).
25 Roetti, C. *Quantum-Mechanical Ab-initio Calculation of the Properties of Crystalline Materials* 125-137 (Springer Berlin Heidelberg, 1996).
26 Gaussian 16 Rev. C.01 (Wallingford, CT, 2016).
27 Perdew, J. P. & Wang, Y. Accurate and simple analytic representation of the electron-gas correlation-energy. *Phys. Rev. B* **45**, 13244-13249 (1992).
28 Becke, A. D. Density-functional thermochemistry. III. The role of exact exchange. *J. Chem. Phys.* **98**, 5648-5652 (1993).
29 Hehre, W. J., Ditchfield, R. & Pople, J. A. Self-consistent molecular orbital methods. XII. further extensions of gaussian-type basis sets for use in molecular orbital studies of organic molecules. *J. Chem. Phys.* **56**, 2257-2261 (1972).
30 Hay, P. J. & Wadt, W. R. Ab initio effective core potentials for molecular calculations. potentials for the transition metal atoms Sc to Hg. *J. Chem. Phys.* **82**, 270-283 (1985).
31 Yu, Z. *et al.* Molecular design for electrolyte solvents enabling energy-dense and long-cycling lithium metal batteries. *Nat. Energy* **5**, 526-533 (2020).
32 Jiang, Z. *et al.* Fluorobenzene, a low-density, economical, and bifunctional hydrocarbon cosolvent for practical lithium metal batteries. *Adv. Funct. Mater.* **31**, 2005991 (2020).
33 Qian, J. F. *et al.* High rate and stable cycling of lithium metal anode. *Nat. Commun.* **6**, 6362 (2015).
34 Ren, X. *et al.* Enabling high-voltage lithium-metal batteries under practical conditions. *Joule* **3**, 1662-1676 (2019).